An Unsteady, Accelerated, High Order Panel Method with Vortex Particle Wakes

by

David Joe Willis

Submitted to the Department of Aeronautics and Astronautics
in partial fulfillment of the requirements for the degree of

Doctor of Philosophy, Department of Aeronautics and Astronautics

at the

MASSACHUSETTS INSTITUTE OF TECHNOLOGY

June 2006

Author .....
Department of Aeronautics and Astronautics
May 22, 2006

Certified by .....
Jaime Peraire
Professor, Department of Aeronautics and Astronautics
Thesis Supervisor

Certified by .....
Jacob K. White
Professor, Department of Electrical Engineering and Computer Science
Thesis Supervisor

Certified by .....
Mark Drela
Professor, Department of Aeronautics and Astronautics
Committee Member

Accepted by .....
Jaime Peraire
Chairman, Department Committee on Graduate Students

An Unsteady, Accelerated, High Order Panel Method with Vortex Particle Wakes

by

David Joe Willis

Submitted to the Department of Aeronautics and Astronautics
on May 30, 2006, in partial fulfillment of the
requirements for the degree of
Doctor of Philosophy, Department of Aeronautics and Astronautics

Abstract

Potential flow solvers for three dimensional aerodynamic analysis are commonly used in industrial applications. The limitation on the number of discretization elements and the user expertise and effort required to specify the wake location are two significant drawbacks preventing the even more widespread use of these codes. These drawbacks are addressed by the hands off, accelerated, unsteady, panel method with vortex particle wakes which is described.

In the thesis, an unsteady vortex particle representation of the domain vorticity is coupled to several boundary element method potential flow formulations. Source-doublet, doublet-Neumann membrane (doublet lattice), and source-Neumann boundary integral equation formulations are implemented. A precorrected-FFT accelerated Krylov subspace iterative solution technique is implemented to efficiently solve the boundary element method linear system of equations. Similarly, a Fast Multipole Tree algorithm is used to accelerate the vortex particle interactions. Additional simplification of the panel method setup is achieved through the introduction of a body piercing wake discretization for lifting bodies with thickness.

Linear basis functions on flat panel surface triangulations are implemented in the accelerated potential flow framework. The advantages of linear order basis functions outweigh the increased complexity of the implementation when compared with traditional constant collocation approaches. Panel integration approaches for the curved panel, double layer self term are presented. A quadratic curved panel, quadratic basis function, Green's theorem direct potential flow solver is presented.

Thesis Supervisor: Jaime Peraire
Title: Professor, Department of Aeronautics and Astronautics

Thesis Supervisor: Jacob K. White
Title: Professor, Department of Electrical Engineering and Computer Science

Acknowledgments

I would like to express my sincere gratitude to my thesis supervisors Professor Jaime Peraire and Professor Jacob White. Their suggestions, guidance, feedback, discussions and support throughout my time at MIT is deeply appreciated. I would like to thank Professor Mark Drela, who provided significant insight and technical support. I would like to thank the readers of the thesis, Professor David Darmofal, and Professor Kenneth Breuer for their abundance of useful suggestions and comments. In addition, I would like to thank Jean Sofronas and Chadwick Collins without whom nothing would be organized. I would like to thank the National Sciences Foundation, The Singapore-MIT Alliance, and the Natural Sciences and Engineering Research Council of Canada for their support of this work.

My time at MIT has been influenced and enhanced by the many friends I have met. I would like to thank them for the friendships we have formed. Ivan Skopovi for his encouragement and positive outlook. Jay Bardhan for the long hours spent discussing BEM in the bowling alley office. Carlos Freire da Silva Pinto Coelho for his magic with C++ and claims of bovine world dominance. Junghoon Lee for his matlab skills and for the valuable technical discussions. Sudeep K. Lahiri for keeping my one foot planted in the FDRL/ACDL lab and for the many discussions both technical and otherwise. Christopher Sequiera for his hard work in coupling his 6 D.O.F. dynamics engine to the flow solver. Zhenhai Zhu and Ben Song for the first pFFT++ implementation which was used in early versions of the flow solver. Xin Wang for helping me settle into the corner office. To Luke Theogarajan for his discussions of Feynman and science in general. A sincere thank you to (Professor) Luca Daniel, Nader Farzaneh, Xin Hu, Tom Klemas, Shihhsien Kuo, Dimitry Vasilyev, Michal Riewenski, Homer Reid, Bradley Bond, Bo Kim, Per Olof Persson, Krzysztof Fidkowski, Garrett Barter, Brian Taff, Anne Vithayathil, John Rockway, Lily Kim, Kin Sou, Du Ke, Lei Zhang, Tarek Moselhy, Laura Proctor, Joe Kanapka, the triathlon club, and all the other members of the MIT community I have interacted with.

Finally, I would like to thank those closest to me, without whom this thesis would not be possible. To my wife, Kayla, I thank you for your patience, encouragement, love, and support through all the ups and downs of the research. Your ability to make the hard

times bearable and the happy times even happier will be forever cherished. To my parents, Owen and Tina and my two sisters, Natasha and Suzie(QT), who have taught me more than education can teach me. For their love, and support throughout my life and academic pursuits. Finally to the Riccio family, John, Maria and Gina who have become my second family. Thank you all.

Contents

List of Figures

List of Tables

Chapter 1

Introduction

The solution of unsteady fluid dynamic flow around morphing bodies remains a challenge for computational scientists. Several algorithms for handling this class of flows have been proposed [1, 2, 3, 4, 5, 6, 7]; however, excessive computation time and power required for moderate to high Reynolds Number flows as well as long setup times for complex geometries limits the widespread use of the methods for practical design and analysis. In this thesis a potential flow solver for simulating unsteady potential flows is presented. Although unsteady potential flow approaches have been proposed in the past [35, 19, 21, 13, 14], the current method has a collection of distinct advantages for the solution of unsteady flow around morphing bodies:

- *Wake Body Intersections*: A formulation which allows for body-piercing wakes is presented, thereby relaxing the strict requirements of body conforming wakes.

- *Particle Wake Representation*: The approach makes use of a time dependent Vortex Particle Method (VPM)[54, 57, 88] to represent domain vorticity rather than a dipole wake sheet [21].

- *Hands-off simulation of complex geometries*: Due to the combined use of a vortex particle wake representation and the implementation of body piercing wakes, hands off simulation of potential flow around complex geometries is possible.

- *Fast Acceleration Approaches*: The precorrected-FFT algorithm (p-FFT)[84], and the Fast Multipole Tree Method (FMT) [110, 70] are used to reduce the solution computational complexity to $O(N\,log(N))$ (where N represents the number of unknowns in the system).

• *Steady State Wake Location*: The method has advantages for steady applications. In particular, it does not require a wake geometry to be prescribed by the user.

• *High order basis functions*: New integration methods for the curved panel dipole are presented. In addition, a method for computing the single layer self term integral over curved surfaces similar to previous work in the field is implemented.

1.1 Panel Methods: A Brief History

Aerodynamics Panel Methods were first investigated in the late 1950s. Since their initial development, they have been instrumental in the design, optimization and analysis of aircraft and aerodynamic bodies [15, 16, 107, 18, 22, 23]. A brief outline of some salient history of panel methods is presented:

1.1.1 BIEs in the Pre-1960s

Prior to the use of digital computers, basic analytical solutions to the potential flow Boundary Integral Equations were employed [24, 25, 26]. The principle of linear superposition of fundamental solutions such as point sources, and point doublets was used regularly to solve potential problems[10]. The field of panel methods was born in 1958, when Smith and Pierce from Douglas Aircraft Company used a discrete form of the boundary integral equations to solve for the potential flow around bodies of revolution [29].

1.1.2 1960s - 1980s

With the success of the initial panel methods, the Smith group received support to continue development of panel methods for both two and three dimensional flow [78]. They pioneered the panel method solution to the lifting body problem in 2-Dimensions [13] and in 3-Dimensions [12]. The development continued to include higher order discretizations of the BEM approach in 2-Dimensions[11]. The Douglas group panel methods were almost exclusively of Neumann type, using either source or vorticity distributions over the surface [10]. In the 1970s, the Green's Theorem perturbation potential based Dirichlet

problem was introduced by Morino [31]. There were also several variations of different complexity of the surface singularity boundary element method/membrane lattice approach [30, 121, 123].

The early panel methods were limited by computer memory and processing power. Some alleviation of computational complexity was achieved by using multipole expansions in place of analytical expressions for panel integral expressions for farfield evaluations; however, the methods still required the solution of a dense linear system.

1.1.3 1980s - 1990s

During the 1980s, several low order three dimensional panel methods were developed [34, 35, 107]. In addition to the low order methods (low order here referring to the constant basis function approximation of the solution), several high order implementations were also developed. These high order methods were developed for the benefits of increased solution accuracy as well as for satisfying the solution continuity requirements imposed by supersonic flow applications. A combined Boeing and NASA effort resulted in PANAIR/A502, a quadratic basis, flat-sub-element high order panel method [116, 36]. Additionally, HISSS [37] a panel method based on PANAIR was developed. In the late 1980s PMARC [106] was developed at NASA-Ames Research Center and was later released as a controlled access computer program. Although the 1980s brought with them great advances in computational power, limitations on computational time and memory still prevented large-scale panel method solutions. Solutions with several thousand panels were routinely performed on large computers; however, due to the coarseness of surface discretizations, limitations on the practical use of panel methods existed. In addition to developments in three dimensional solvers, two dimensional panel methods were being developed and used heavily for inverse airfoil design [38, 27, 39, 28]. Furthermore, the use of boundary layer coupling was investigated for incorporating viscous effects[38, 39].

In the 1980s several algorithmic developments were also made which have had a significant impact on the development of panel methods. These developments included iterative solution methods, most notably for this thesis the development of Krylov subspace iterative

solvers [100, 42, 43]. In addition to iterative solvers, several sparsification and acceleration routines were also developed in order to facilitate the rapid computation of matrix vector products of the dense BEM linear systems. The first category of fast methods involved multipole expansion approximations of the farfield influences [110, 70, 86]. The second category of methods relied on rapidly approximating farfield interactions using a Cartesian background mesh[102, 50, 68].

1.1.4 1990s - present

By the 1990s panel methods had largely given way to higher fidelity Navier-Stokes and Euler solvers [105, 51]. Although Eulerian reference frame domain solvers were being heavily investigated, several Lagrangian based approaches were developed. The Vortex Particle Method was refined and further investigated for the simulation of largely vortical flow [54, 59, 56, 57, 60, 67]. The section which follows describes some of the history and development of vortex particle methods. Despite the promise of Navier-Stokes solvers, accurate viscous drag prediction remained an elusive task. In the 1990s several researchers started to consider the problem of 3-Dimensional Integral Boundary Layer Methods[40, 41] with some success.

The Fast Multipole Method [110] was used and further developed in practical boundary element method solvers for many diverse disciplines [44, 49, 46]. In the early 1990s, the precorrected-FFT algorithm [84] was developed. The precorrected-FFT approach provided a kernel independent framework for the acceleration of BEM and N-body problems[45, 83]. In the 1990s and 2000s several panel method codes continued the advancement of higher order approximations to the boundary integral equations[115, 117, 118, 119, 120, 123, 124, 125, 111], however, due to the complexity involved with higher order methods and the lack of robust and efficient integration techniques for higher order approaches, their adoption in the BEM community is limited in comparison with the popular constant collocation type approaches.

1.2 Vortex Particle Methods: Background and Previous Work

Like the panel method, the vortex particle method (VPM) has a rich and long history which is presented in several references [54, 57, 88]. Only some of the brief points of interest are outlined in this section. The framework for Vortex Particle Methods originated well before the digital computer age. In 1930, Rosenhead performed a dynamical vortex calculation using singular point vortices [53]. The vortex particle method in 3-Dimensions was largely derived from the 2-Dimensional method. Initial investigations in 3-Dimensions used vortex filament approximations to account for the domain vorticity [58, 55]. The difficulty with the vortex filament and sheet methods was the need to store the connectivity information. Beale and Majda [57] proposed the first vortex blob method in which the vortex blob positions and strengths were updated in a Lagrangian manner with no connectivity between the blobs. Several advancements have been made to the vortex particle method since its inception which can be found in the following works [54, 57, 59].

The use of vortex particles, vortex filaments as well as vortex sheets has been explored for representation of domain vorticity in many diverse applications [60, 54, 59, 65, 67, 68]. Many current vortex particle methods are used for the simulation of turbulent flows. The method has been found to be quite useful for the prediction of jet flows [66], turbulent bluff-body wake flows [59], internal flows [67], etc.

Much like panel methods, the vortex particle approaches require the evaluation of an N-body interaction problem at each step of the simulation. Since the particles advect in a Lagrangian manner, their positions change at each timestep, requiring the re-computation of inter-particle influences. With the development of $O(Nlog(N))$ algorithms such as the Fast Multipole Tree [110], and particle in cell [102] methods, the particle based approaches became viable for the large number of particles required to adequately resolve the flow physics.

1.2.1 Combined Panel Method - Vortex Method Approaches

Vorticity representation in panel method aerodynamics has been traditionally limited to vorticity sheet and vortex filament approaches [113, 107, 10]. Although vortex particles are used commonly for representing vorticity in unsteady 2-Dimensional aerodynamics computations [61, 113, 65], the use of vortex particle methods to model lifting body vortex wake sheets in 3-Dimensional aerodynamic panel methods has been limited to a small number of researchers [62, 63, 64]. The previous use of the combined 3-Dimensional panel method and vortex particle approach has been limited to applications in which a lifting surface or series of lifting surfaces is considered isolated from the body (sails [64] and wind turbines [62]). Combined panel method and vortex particle approaches require a sufficiently high density of vortex particles to practically and accurately model the vortex sheet; therefore, when acceleration methods are not considered, these approaches suffer from large computational times and low accuracy. The vortex particle approach has also been coupled to several boundary element potential flow methods in disciplines other than aerodynamics; however, this coupling often involves approaches for modeling the near wall viscous effects which are beyond the scope of this thesis [67, 69, 59].

1.3 Challenges with Panel Methods

Despite the comprehensive development of panel methods over the past several decades, there are several drawbacks to existing methods which hinder their more common use, namely:

- *Stringent requirements for wake discretizations*: There are two primary drawbacks with current wake discretizations.

1. Due to the necessity to impose a potential jump in the wake region, there is a need to have a body conforming wake surface mesh. This poses significant challenges in the problem setup and meshing.

2. For unsteady problems, the development and accurate advection of the wake is often compromised when wing-body simulations are considered. Common problems

include: intersection of the wake with downstream surfaces, the difficulty in wake-body intersection meshing, and the time and effort required to compute full unsteady flows.

By providing a panel method framework which incorporates an automatic wake generation and advection approach, the difficulties associated with user expertise and user interference will be reduced.

• *Memory and Processor Imposed Limitations*: Physical computer memory constraints as well as unrealistic solution times hinder the applicability of panel methods to practical problems. This limit on the number of elements prevents the interfacing of panel methods to traditional CAD and CFD grid generation tools. In addition to the panel count limitations, specific surface panel types (such as quadrilateral) often prevent the use of CAD and CFD compatible discretizations. By ensuring a panel method can use the same surface grid as a CFD tool will reduce the significant preprocessing workload for aircraft designers. Often, preprocessing such as surface grid generation and geometry description is more time consuming than solutions.

• *Discrete Approximation to the Continuous Problem* : Most panel methods in use consider low order approximations for both the geometric discretization as well as the solution basis representation. In particular, a common approach is the constant collocation approximation on flat polygonal elements. Although the approach works well for many simulations, it is shown in Chapter 3 that the method has several drawbacks. Increased accuracy and faster convergence rates are a direct consequence of appropriately designed higher order methods.

1.4 Thesis Outline

In the following chapters of this thesis, solutions to each of the drawbacks of the traditional panel method are presented. The resulting solution framework which is implemented provides rapid simulations of potential flow simulations which are accurate, and easy to compute. Chapter 2 outlines the applicable theory and Boundary Integral Equation formulations considered. In chapter 3, a novel integration approach for high order curved panel

integrals is presented for the double layer potential (the single layer potential approach is also demonstrated and closely resembles traditional approaches). In chapter 4 approaches for handling the wake vorticity are presented. In chapter 5, the details of the implementation of the panel method is presented. Finally in chapter 6 and chapter 7 validation, results and conclusions are presented.

Chapter 2

The Governing Equations

In this chapter the governing fluid dynamics equations are presented.

2.0.1 The Domain

Consider the domain illustrated in Fig. 2-1. A point position, $\vec{R}(X, Y, Z, t)$, in space at a given time, defined in the fixed-in-space global reference frame is:

$$\vec{R}_p = \vec{R}_G + \vec{r}_{Gp}, \tag{2.1}$$

where $\vec{R}_G$ is the position of the body frame origin, and $\vec{r}_{Gp}$ is the position of point p relative to the local body frame. A given point on the body will have a velocity with respect to the global reference frame given by:

$$\vec{V}_p = \vec{V}_G + \vec{V}_{Gp} + (\vec{\Omega} \times \vec{r}_{Gp}), \tag{2.2}$$

where $\vec{V}_G$ represents the velocity of the body frame origin in global coordinates, $\vec{\Omega}$ is the angular velocity, and $\vec{V}_{Gp}$ represents the relative motion of the surface due to deformation of the body (eg. deflection of a control surface). For clarity, body velocities are denoted by $\vec{V}$ and fluid velocities by $\vec{U}$.

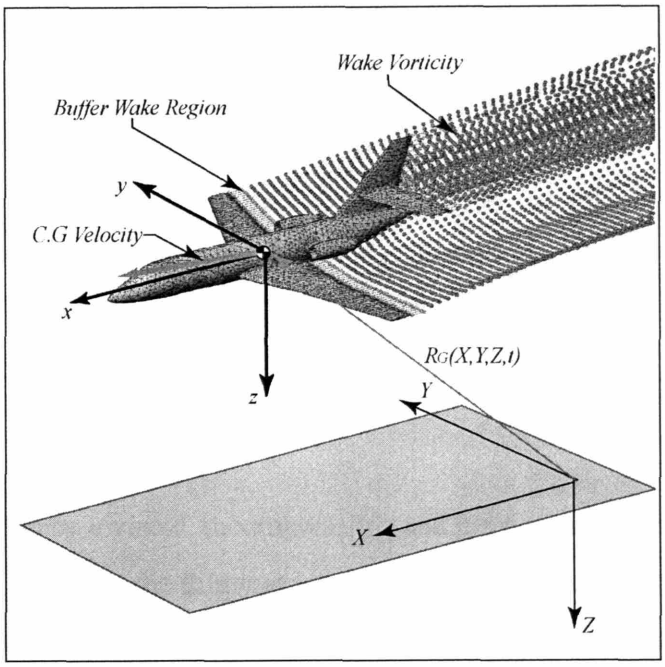

Figure 2-1: The domain of interest includes all fluid external to the aircraft surface. The particles trailing the wing section, the vertical tail and horizontal stabilizer represent regions in which vorticity exists due to the lifting surface trailing shear layer.

2.1 The Governing Flow Equations

In the paragraphs which follow, the governing equations and assumptions are presented.

2.1.1 The Boundary Conditions

At any point on a solid surface in the domain, a no penetrating flux boundary condition (flow tangency condition) is given by:

$$\hat{n} \cdot \vec{U}(\vec{R}, t) = \hat{n} \cdot (\vec{V}_G + \vec{V}_{Gp} + \vec{\Omega} \times \vec{r}_{Gp}), \tag{2.3}$$

where, $\hat{n}$ is the outward unit normal vector on the body at a given point $\vec{R}$ on the body surface. The rate at which the perturbations in velocity decay with distance from a non-lifting body is:

$$\lim_{\vec{R} \to \infty} \vec{U}(\vec{R}, t) \leq O\left(\frac{1}{\|\vec{R}\|^3}\right). \tag{2.4}$$

Similarly, for a lifting body, the velocity radiation condition is:

$$\lim_{\vec{R}\to\infty} \vec{U}(\vec{R},t) \leq O\left(\frac{1}{\|\vec{R}\|^2}\right). \tag{2.5}$$

The slower decay of the velocity in a lifting body simulation is due to the presence of the trailing vorticity in the wakes.

2.1.2 Velocity Definition

The flow is assumed to be inviscid, incompressible and have constant density. Any vorticity in the domain is localized on the thin wake regions trailing the lifting surfaces. Otherwise, the flow is assumed to be irrotational. These assumptions greatly simplify the form of the governing equations. The fluid velocity, $\vec{U}(\vec{R},t)$ satisfies the following two farfield conditions:

$$\nabla \cdot \vec{U}(\infty,t) = 0, \tag{2.6}$$

by the continuity requirement, and:

$$\nabla \times \vec{U}(\infty,t) = 0, \tag{2.7}$$

by the farfield velocity decay boundary condition. As a consequence of the above fluid velocity field properties, the fluid velocity, $\vec{U}(\vec{R},t)$ at a given point in the domain can be expressed as the superposition of a scalar potential component, $\vec{U}_\phi(\vec{R},t)$, and a solenoidal vector potential component, $\vec{U}_\Psi(\vec{R},t)$, using a Helmholtz decomposition [77]:

$$\vec{U}(\vec{R},t) = \vec{U}_\phi(\vec{R},t) + \vec{U}_\Psi(\vec{R},t) = \nabla\phi + \nabla \times \vec{\Psi}. \tag{2.8}$$

The scalar potential component of the velocity is irrotational and any rotational effects are captured in the vector potential component. The decomposition of the velocity field into a scalar potential and a vector potential component is not commonly considered in most panel method implementations. By performing the decomposition, the traditional scalar potential boundary element method formulations can still be used; however, with

the addition of the vector potential, wake vorticity can be modeled directly using vortex distributions (volumes, sheets or points) rather than indirectly through the use of dipole sheets.

In terms of the vector and scalar potentials, the boundary condition of equation 2.3 is:

$$\hat{n} \cdot (\nabla\phi + \nabla \times \vec{\Psi}) = \hat{n} \cdot (\vec{V}_G + \vec{V}_{Gp} + \vec{\Omega} \times \vec{r}_{Gp}). \tag{2.9}$$

Note that due to the inviscid flow assumption, only the normal velocity boundary condition is applied at the body surface.

2.1.3 The Scalar Potential Relationships

The governing continuity equation for a constant density fluid is expressed in differential form as:

$$\nabla \cdot \vec{U} = 0,$$

Substituting the velocity as defined in equation 2.8 into the continuity equation the resulting mass conservation equation is:

$$\nabla \cdot (\nabla\phi + \nabla \times \vec{\Psi}) = \nabla \cdot (\nabla\phi) = \nabla^2\phi = 0. \tag{2.10}$$

Which is the Laplace's equation for the scalar potential.

2.1.4 The Vector Potential Relationships

The Vector Potential - Vorticity Relationship

The vorticity in the domain, $\vec{\omega}(\vec{R}, t)$, is defined as the curl of the velocity [8]:

$$\nabla \times \vec{U} = \vec{\omega} \tag{2.11}$$

The velocity component due to the *Vector Potential*, $\vec{\Psi}$, is:

$$\nabla \times \vec{\Psi} = \vec{U}_\Psi \tag{2.12}$$

Substituting the vector potential relationship (equation 2.12) into the definition of vorticity (equation 2.11), and choosing the vector potential to be a solenoidal vector field ($\nabla \cdot \vec{\Psi} = 0$), results in:

$$\nabla^2 \vec{\Psi} = -\vec{\omega}, \tag{2.13}$$

which is a vector Poisson equation relating the vector potential to the vorticity.

The Vorticity Evolution Equation

The vorticity evolution equation is derived from the incompressible Euler equations [8],

$$\frac{\partial \vec{U}}{\partial t} + \vec{U} \cdot \nabla \vec{U} = -\frac{\nabla p}{\rho}, \tag{2.14}$$

where, ρ, is the fluid density, and p is the pressure. Taking the curl of eqn. 2.14, the resulting equation for the vorticity evolution in the domain is [8],

$$\frac{D\vec{\omega}}{Dt} = \frac{\partial \vec{\omega}}{\partial t} + \vec{U} \cdot \nabla \vec{\omega} = \vec{\omega} \cdot \nabla \vec{U} \tag{2.15}$$

where the term $\vec{\omega} \cdot \nabla \vec{U}$ on the right hand side represents the vorticity stretching (or how the magnitude and direction of the vorticity changes as it is exposed to velocity gradients in the flow field). The left hand side of the equation is simply the total derivative of the vorticity with respect to time.

2.1.5 The Integral Equation Relationships for the Vorticity in the Domain

The vector Poisson equation governs the velocity vector potential (see equation 2.13). In integral form, the vector potential due to the vorticity in the domain is:

$$\vec{\Psi}(\vec{r}, t) = \frac{1}{4\pi} \int_V \frac{\vec{\omega}}{\|\vec{r} - \vec{r}'\|} dV', \tag{2.16}$$

where, V is the volume of the domain in which the vorticity, $\vec{\omega}$, exists. The vorticity induced velocity is determined by taking the curl of equation 2.16:

$$\vec{U}_{\Psi} = \nabla \times \vec{\Psi}(\vec{r}, t) = \nabla \times \frac{1}{4\pi} \int_V \frac{\vec{\omega}}{\|\vec{r} - \vec{r}'\|} dV'. \tag{2.17}$$

The resulting expression in equation 2.17 for vortex filaments is the familiar Biot-Savart law [113, 8]. Similarly, the associated component of the gradient of the velocity term used for the vorticity stretching in the vorticity evolution equation is determined by taking the gradient of equation 2.17.

2.2 Boundary Integral Equations for the Potential Flow Equation

The derivation of the potential flow boundary integral equations is briefly presented in this section. First, a general derivation is presented, following which is a closer examination of the integral equation formulations.

2.2.1 Derivation of the Green's theorem BIE

The following derivation is similar to that presented in [94, 127, 95, 96, 113]. Consider the potential governed by Laplace's equation:

$$\nabla^2 \phi(\vec{r}) = 0. \tag{2.18}$$

A particular fundamental solution (Green's function) to Laplace's equation is:

$$G(\vec{r}, \vec{r}') = \frac{1}{\|\vec{r} - \vec{r}'\|}. \tag{2.19}$$

The following statements are a result of integrating by parts (for $\vec{r} \neq \vec{r}'$) [25]:

$$\int_V \left[\frac{1}{\|\vec{r}-\vec{r}'\|}\right] \nabla^2\phi \, dV' = -\int_V \left(\nabla\left[\frac{1}{\|\vec{r}-\vec{r}'\|}\right] \cdot \nabla\phi\right) dV' + \int_S \left[\frac{1}{\|\vec{r}-\vec{r}'\|}\right] \hat{n}_{\vec{r}'} \cdot \nabla\phi \, dS', \tag{2.20}$$

and, similarly:

$$\int_V \phi\nabla^2 \left[\frac{1}{\|\vec{r}-\vec{r}'\|}\right] dV' = -\int_V \left(\nabla\left[\frac{1}{\|\vec{r}-\vec{r}'\|}\right] \cdot \nabla\phi\right) dV' + \int_S \phi \, \hat{n}_{\vec{r}'} \cdot \nabla \left[\frac{1}{\|\vec{r}-\vec{r}'\|}\right] dS', \tag{2.21}$$

where, $\vec{r}'$ is the integration variable position on the boundary surface, S represents the domain boundary surfaces under consideration, and $n_{\vec{r}'}$ represents the boundary surface normal (directed into the fluid domain) at the integration variable position. Combining equations 2.20 and 2.21, results in:

$$\int_V \left[\left(\frac{1}{\|\vec{r}-\vec{r}'\|}\right) \nabla^2\phi\right] dV' = \int_V \phi\nabla^2 \left[\frac{1}{\|\vec{r}-\vec{r}'\|}\right] dV' + \int_{S_W+S_B+S_\infty+S_{Sphere}} \left[\left(\frac{1}{\|\vec{r}-\vec{r}'\|}\right) \nabla\phi - \phi\nabla\left(\frac{1}{\|\vec{r}-\vec{r}'\|}\right)\right] \cdot \hat{n}_{\vec{r}'} \, dS'. \tag{2.22}$$

Figure 2-2 illustrates the boundaries of the fluid domain as well as the spherical exclusion surrounding the point $\vec{r} = \vec{r}'$. The volume integrals in equation 2.22 are identically zero. Hence the integral equation reduces to a boundary integral equation:

$$\int_{S_W+S_B+S_\infty+S_{Sphere}} \left[\phi\nabla\left(\frac{1}{\|\vec{r}-\vec{r}'\|}\right) - \left(\frac{1}{\|\vec{r}-\vec{r}'\|}\right) \nabla\phi\right] \cdot \hat{n}_{\vec{r}'} \, dS' = 0. \tag{2.23}$$

Integration over the farfield boundary reduces to zero due to the radiation boundary condition. The integration over the surface of the spherical exclusion region simplifies to [113, 95]:

$$\int_{S_{Sphere}} \left[\phi\nabla\left(\frac{1}{\|\vec{r}-\vec{r}'\|}\right) - \left(\frac{1}{\|\vec{r}-\vec{r}'\|}\right) \nabla\phi\right] \cdot \hat{n}_{\vec{r}'} \, dS' = -4\pi\phi(\vec{r}). \tag{2.24}$$

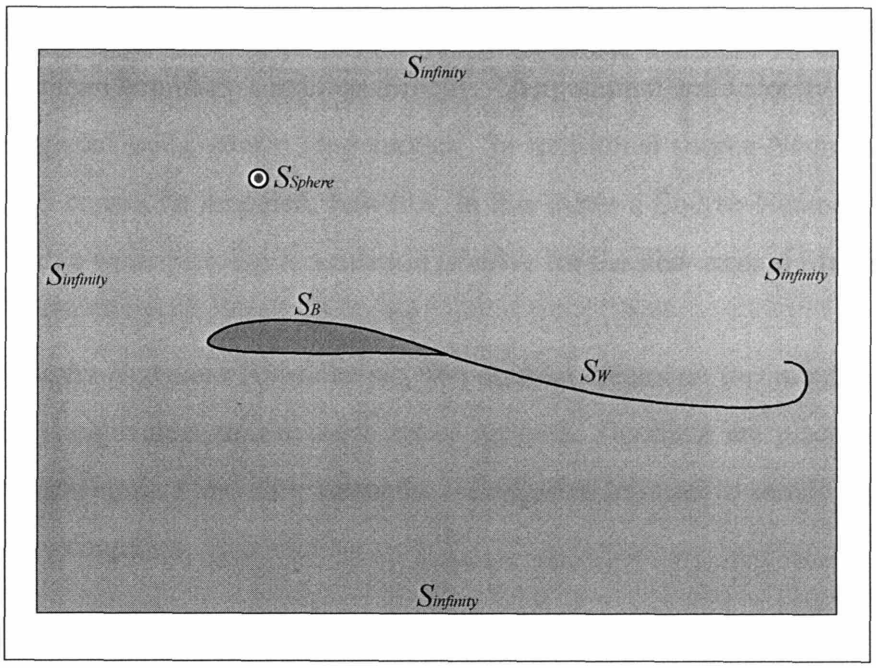

Figure 2-2: The fluid domain considered in the derivation of the Green's Theorem BIE

The result is the Greens Theorem boundary integral equation for describing the potential at an evaluation point $\vec{r}$ inside of the fluid domain:

$$\phi(\vec{r}) = \frac{1}{4\pi}\int_{S_B} \frac{\partial\phi}{\partial n_{\vec{r}'}}\left[\frac{1}{\|\vec{r}-\vec{r}'\|}\right] dS'_B - \frac{1}{4\pi}\int_{S_B+S_W} \phi\frac{\partial}{\partial n_{\vec{r}'}}\left[\frac{1}{\|\vec{r}-\vec{r}'\|}\right] dS'_{B+W}, \quad (2.25)$$

2.2.2 BIE Formulations

In this work, the following Boundary Integral Equation formulations are considered:

1. *The Greens Theorem Formulation*: The traditional Greens theorem formulation [113, 95, 127] involves solving for the surface potential on the body boundary by specifying the normal derivative according to the boundary conditions.

2. *The Source-Doublet Formulation*: The source doublet formulation [31, 113] is a common panel method formulation consisting of an interior and an exterior domain over which potentials are defined. The jump in the potential is prescribed using doublets and the jump in the normal derivative of the potential is prescribed using surface sources.

3. *The Source-Neumann Formulation*: The source-Neumann formulation [13] satisfies the Neumann boundary condition directly. The potential and velocity in the domain are computed using source singularities. In traditional source-Neumann formulations, lift cannot be modeled; however, in this thesis a Source-Neumann method is used with a wake piercing formulation to solve for the flow around lifting bodies.

4. *The Doublet-Neumann Formulation*: The doublet-Neumann formulation [113] considered is equivalent to a doublet lattice method. Doublets are placed onto an infinitely thin surface and their strengths are adjusted in order to satisfy the Neumann boundary condition.

In the following paragraphs the above methods are presented.

The Direct Green's Theorem BIE

The Green's Theorem boundary integral equation for computing the potential at a point, $(\vec{r})$, in the fluid domain due to a non-lifting body is [95, 127, 113]:

$$\phi(\vec{r}) = \frac{1}{4\pi}\int_{S_B} \frac{\partial \phi}{\partial n_{\vec{r}'}}(\vec{r}')\frac{1}{\|\vec{r}-\vec{r}'\|}dS'_B - \frac{1}{4\pi}\int_{S_B}\phi(\vec{r}')\frac{\partial}{\partial n_{\vec{r}'}}\left[\frac{1}{\|\vec{r}-\vec{r}'\|}\right]dS'_B, \qquad (2.26)$$

The lifting-body potential flow problem requires the addition of a potential jump in the trailing wake region to account for the physical vorticity[113]. In equation 2.25 the following Green's Theorem boundary integral equation expression resulted when a wake was included in the domain:

$$\phi(\vec{r}) = \frac{1}{4\pi}\int_{S_B} \frac{\partial \phi}{\partial n_{\vec{r}'}}\left[\frac{1}{\|\vec{r}-\vec{r}'\|}\right]dS'_B - \frac{1}{4\pi}\int_{S_B+S_W}\phi\frac{\partial}{\partial n_{\vec{r}'}}\left[\frac{1}{\|\vec{r}-\vec{r}'\|}\right]dS'_{B+W}. \qquad (2.27)$$

In this case the potential, ϕ, includes a component due to the body, ϕ_B, and a component due to the wake, ϕ_W.

A slightly different expression for the lifting body potential arises from a superposition principle, in which the potential due to a dipole sheet trailing all lifting surfaces is added to

the Green's Theorem representation of the non-lifting potential flow (equation 2.26):

$$\phi(\vec{r}) = \frac{1}{4\pi}\int_{S_B} \frac{\partial \phi_B}{\partial n_{\vec{r}'}}(\vec{r}')\frac{1}{\|\vec{r}-\vec{r}'\|}dS'_B - \frac{1}{4\pi}\int_{S_B} \phi_B(\vec{r}')\frac{\partial}{\partial n_{\vec{r}'}}\left[\frac{1}{\|\vec{r}-\vec{r}'\|}\right]dS'_B + \Phi_W, \tag{2.28}$$

Where Φ_W represents the added domain potential jump influence due to the wake. The potential $\phi(\vec{r})$ represents a contribution from both the body and the wake:

$$\phi(\vec{r}) = \phi_B(\vec{r}) + \Phi_W(\vec{r}). \tag{2.29}$$

Notice, in equation 2.28, that the unknown is the body surface potential (ϕ_B). The wake potential, Φ_W can be expressed as a function of the prescribed wake potential jump, μ_W as:

$$\Phi_W = \frac{1}{4\pi}\int_{S_W} \mu_W(\vec{r}')\frac{\partial}{\partial n_{\vec{r}'}}\left[\frac{1}{\|\vec{r}-\vec{r}'\|}\right]dS'_W \tag{2.30}$$

In order to uniquely solve equation 2.28 for the potential, $\phi(\vec{r}')$, the following steps are taken:

1. Prescribe a wing trailing edge Kutta condition which relates the unknown wake strength(s) μ_W to the surface potential or its derivatives.

2. Specify the normal derivative of the potential at the boundary. Equation 2.3 is used:

$$\hat{n}\cdot\nabla\phi_B(\vec{R},t) = \hat{n}\cdot\left(\vec{V}_G + \vec{V}_{Gp} + \vec{\Omega}\times\vec{r}_{Gp} - \nabla\times\vec{\Psi}(\vec{R},t) - \nabla\Phi_W(\vec{r})\right), \tag{2.31}$$

In order to solve for the body potential $\phi_B(\vec{r})$, the problem must be reduced to one in which the influence of all of the other potentials comprising the solution become boundary conditions.

Depending on the wake representation, either of the expressions (equation 2.25 or equation 2.28) for a lifting body problem may be used. In this work, the wake is often considered as a potential influence close to the body (in order to satisfy the Kutta condition) and as a velocity influence further away from the body (using a vorticity representation).

The Indirect Source-Doublet BIE

The source-doublet formulation is commonly presented in place of the Green's theorem formulation in many aerodynamics texts [113, 20]. The source-doublet approach considers the two domains which are separated by the surface of the body. The first region is the domain interior to the aerodynamic body under consideration. The second region which is considered is the domain exterior to the body boundary surface (which includes the fluid of interest). Inside of each of these domains a potential can be defined.

Setting up a potential flow inside of the body yields the following interior potential $\phi_i(\vec{r})$ expression for an evaluation point inside of the body:

$$\begin{aligned}\phi_i(\vec{r}) =& \frac{1}{4\pi}\int_{S_B}\frac{\partial\phi_i}{\partial n_{\vec{r}'}}(\vec{r}')\frac{1}{\|\vec{r}-\vec{r}'\|}dS'_B - \\ & \frac{1}{4\pi}\int_{S_B}\phi_i(\vec{r}')\frac{\partial}{\partial n_{\vec{r}'}}\left[\frac{1}{\|\vec{r}-\vec{r}'\|}\right]dS'_B,\end{aligned} \tag{2.32}$$

Similarly, for an evaluation point in the region exterior to the body (inside the fluid of interest), the influence of the internal potential is:

$$\begin{aligned}0 =& \frac{1}{4\pi}\int_{S_B}\frac{\partial\phi_i}{\partial n_{\vec{r}'}}(\vec{r}')\frac{1}{\|\vec{r}-\vec{r}'\|}dS'_B - \\ & \frac{1}{4\pi}\int_{S_B}\phi_i(\vec{r}')\frac{\partial}{\partial n_{\vec{r}'}}\left[\frac{1}{\|\vec{r}-\vec{r}'\|}\right]dS'_B,\end{aligned} \tag{2.33}$$

For a point exterior to the body, the potential $\phi(\vec{r})$ is described by:

$$\begin{aligned}\phi(\vec{r}) =& \frac{1}{4\pi}\int_{S_B}\frac{\partial\phi}{\partial n_{\vec{r}'}}(\vec{r}')\frac{1}{\|\vec{r}-\vec{r}'\|}dS'_B - \\ & \frac{1}{4\pi}\int_{S_B}\phi(\vec{r}')\frac{\partial}{\partial n_{\vec{r}'}}\left[\frac{1}{\|\vec{r}-\vec{r}'\|}\right]dS'_B + \Phi_W,\end{aligned} \tag{2.34}$$

Adding the interior potential expression (equation 2.33) to the expression in equation 2.34 (while appropriately adjusting the surface normal definition to point into the fluid domain

(exterior to the body)), the following integral equation results:

$$\phi(\vec{r}) = \frac{1}{4\pi}\int_{S_B} \frac{\partial(\phi-\phi_i)}{\partial n_{\vec{r}'}}(\vec{r}')\frac{1}{\|\vec{r}-\vec{r}'\|}dS'_B - \frac{1}{4\pi}\int_{S_B}(\phi(\vec{r}')-\phi_i(\vec{r}'))\frac{\partial}{\partial n_{\vec{r}'}}\left[\frac{1}{\|\vec{r}-\vec{r}'\|}\right]dS'_B + \Phi_W, \tag{2.35}$$

By compactly representing the surface singularity distributions, the following equation results:

$$\phi(\vec{r}) = \frac{1}{4\pi}\int_{S_B}\mu(\vec{r}')\frac{\partial}{\partial n_{\vec{r}'}}\left[\frac{1}{\|\vec{r}-\vec{r}'\|}\right]dS'_B - \frac{1}{4\pi}\int_{S_B}\sigma(\vec{r}')\frac{1}{\|\vec{r}-\vec{r}'\|}dS'_B + \Phi_W. \tag{2.36}$$

The doublet, μ represents the interface potential jump:

$$\mu(\vec{r}) = \phi_e(\vec{r}) - \phi_i(\vec{r}), \tag{2.37}$$

where the superscripts e and i represent the limit as the point $\vec{r}$ is approached from the exterior domain, and the interior domain respectively. The source, σ represents the magnitude of the interface discontinuity in the normal derivative:

$$\sigma(\vec{r}) = \left(\frac{\partial\phi_e}{\partial n}\right) - \left(\frac{\partial\phi_i}{\partial n}\right) \tag{2.38}$$

The application of boundary conditions to the source-doublet formulation is similar to that in the Green's Theorem formulation; however, care must be taken to ensure that the interior and exterior problems are appropriately considered. A benefit of the source-doublet method is that the interior potential can be carefully chosen in order to simplify the particular problem being solved. In the following paragraphs a brief discussion of two of the many possible interior potential choices is presented. The two formulations represent a subtle difference between the traditional source-doublet method and a useful variation of the source-doublet method which is investigated in this thesis:

Internal Potential Case 1: In the first example of the source-doublet approach, a zero

internal potential is examined:

$$\phi(\vec{r}) = \frac{1}{4\pi}\int_{S_B} \mu(\vec{r}')\frac{\partial}{\partial n_{\vec{r}'}}\frac{1}{\|\vec{r}-\vec{r}'\|}dS'_B - \frac{1}{4\pi}\int_{S_B} \sigma(\vec{r}')\frac{1}{\|\vec{r}-\vec{r}'\|}dS'_B + \Phi_W. \tag{2.39}$$

In this case the source strength has a value:

$$\sigma(\vec{r}) = \left(\frac{\partial \phi_e}{\partial n_{\vec{r}}}\right) = \hat{n}_{\vec{r}} \cdot \left(\vec{V}_G + \vec{V}_{Gp} + \vec{\Omega} \times \vec{r}_{Gp} - \nabla \times \vec{\Psi}(\vec{R}, t)\right), \tag{2.40}$$

and, similarly, the doublet strength can be written as:

$$\mu(\vec{r}) = \phi_e(\vec{r}) - \phi_i(\vec{r}) = \phi(\vec{r}), \tag{2.41}$$

By inserting these values into the source-doublet BIE, the result is:

$$\begin{aligned}\phi(\vec{r}) =& \frac{1}{4\pi}\int_{S_B} \phi(\vec{r}')\frac{\partial}{\partial n_{\vec{r}'}}\frac{1}{\|\vec{r}-\vec{r}'\|}dS'_B - \\ & \frac{1}{4\pi}\int_{S_B} \hat{n}_{\vec{r}'} \cdot \left(\vec{V}_G + \vec{V}_{Gp} + \vec{\Omega} \times \vec{r}_{Gp} - \nabla \times \vec{\Psi}(\vec{R}, t)\right)\frac{1}{\|\vec{r}-\vec{r}'\|}dS'_B + \\ & \Phi_W.\end{aligned} \tag{2.42}$$

hence,

$$\begin{aligned}\phi_B(\vec{r}) =& \frac{1}{4\pi}\int_{S_B} \phi(\vec{r})\frac{\partial}{\partial n_{\vec{r}'}}\frac{1}{\|\vec{r}-\vec{r}'\|}dS'_B - \\ & \frac{1}{4\pi}\int_{S_B} \hat{n}_{\vec{r}'} \cdot \left(\vec{V}_G + \vec{V}_{Gp} + \vec{\Omega} \times \vec{r}_{Gp} - \nabla \times \vec{\Psi}(\vec{R}, t)\right)\frac{1}{\|\vec{r}-\vec{r}'\|}dS'_B.\end{aligned} \tag{2.43}$$

Solving equation 2.43 gives the potential $\phi(\vec{r})$ (which is also the doublet strength) at the surface of the body. This expression is similar to equation 2.25. The potential and velocity at points in the domain is a simple evaluation of the BIE in equation 2.39.

Internal Potential Case 2: In the second example of the source-doublet approach, an interior potential corresponding to the wake induced potential is examined:

$$\phi(\vec{r}) = \frac{1}{4\pi}\int_{S_B} \mu(\vec{r}')\frac{\partial}{\partial n_{\vec{r}'}}\frac{1}{\|\vec{r}-\vec{r}'\|}dS'_B - \frac{1}{4\pi}\int_{S_B} \sigma(\vec{r}')\frac{1}{\|\vec{r}-\vec{r}'\|}dS'_B + \Phi_W. \tag{2.44}$$

where, the source strength has a value:

$$\begin{aligned}\sigma(\vec{r}) &= \left(\frac{\partial \phi_e}{\partial n_{\vec{r}}}\right) - \left(\frac{\partial \phi_i}{\partial n_{\vec{r}}}\right) \\ &= \hat{n}_{\vec{r}'} \cdot \left(\vec{V}_G + \vec{V}_{Gp} + \vec{\Omega} \times \vec{r}_{Gp} - \nabla \times \vec{\Psi}(\vec{R}, t) - \nabla \Phi_W(\vec{r})\right), \end{aligned} \tag{2.45}$$

and, similarly, the doublet strength can be written as:

$$\mu(\vec{r}) = \phi_e(\vec{r}) - \phi_i(\vec{r}) = \phi_e(\vec{r}) - \Phi_W(\vec{r}) = \phi_B(\vec{r}), \tag{2.46}$$

By inserting these source and doublet values into the source-doublet BIE, the result is:

$$\begin{aligned}\phi(\vec{r}) =& \frac{1}{4\pi} \int_{S_B} \phi_B(\vec{r}) \frac{\partial}{\partial n_{\vec{r}'}} \frac{1}{\|\vec{r} - \vec{r}'\|} dS'_B + \Phi_W - \\ & \frac{1}{4\pi} \int_{S_B} \hat{n}_{\vec{r}'} \cdot \left(\vec{V}_G + \vec{V}_{Gp} + \vec{\Omega} \times \vec{r}_{Gp} - \nabla \times \vec{\Psi}(\vec{R}, t) - \nabla \Phi_W(\vec{r})\right) \frac{1}{\|\vec{r} - \vec{r}'\|} dS'_B \end{aligned} \tag{2.47}$$

hence,

$$\begin{aligned}\phi_B(\vec{r}) =& \frac{1}{4\pi} \int_{S_B} \phi_B(\vec{r}) \frac{\partial}{\partial n_{\vec{r}'}} \frac{1}{\|\vec{r} - \vec{r}'\|} dS'_B - \\ & \frac{1}{4\pi} \int_{S_B} \hat{n}_{\vec{r}'} \cdot \left(\vec{V}_G + \vec{V}_{Gp} + \vec{\Omega} \times \vec{r}_{Gp} - \nabla \times \vec{\Psi}(\vec{R}, t) - \nabla \Phi_W(\vec{r})\right) \frac{1}{\|\vec{r} - \vec{r}'\|} dS'_B. \end{aligned} \tag{2.48}$$

Which is similar to the expression presented in equation 2.28.

In the first internal potential case the boundary integral equation absorbed the wake potential into the surface singularity strength representations; however, in the second example, the wake was treated as a superimposed potential field and as such the potential on the body. In the second case, one effectively sets up an internal potential which corresponds to the wake potential. The difference between the two formulations is subtle. For the work presented in this thesis, the ability to treat the wake using a velocity and/or potential representation is useful.

The Indirect Neumann Source BIE

The remaining two BIE formulations which are considered impose Neumann boundary conditions. The Neumann-Source formulation potential is [113]:

$$\phi(\vec{r}) = \frac{1}{4\pi}\int_{S_B} \sigma(\vec{r}')\frac{1}{\|\vec{r}-\vec{r}'\|}dS'_B, \tag{2.49}$$

where, $\sigma(\vec{r}')$ is the boundary surface distribution of fluid source strength. To add generality, an arbitrarily defined potential Φ_W can be added:

$$\phi(\vec{r}) = \phi_B(\vec{r}) + \Phi_W = \frac{1}{4\pi}\int_{S_B} \sigma(\vec{r}')\frac{1}{\|\vec{r}-\vec{r}'\|}dS'_B + \Phi_W. \tag{2.50}$$

The gradient of the equation is taken to yield a boundary integral equation for the velocity in the domain:

$$\nabla\phi(\vec{r}) = \nabla\left(\frac{1}{4\pi}\int_{S_B} \sigma(\vec{r}')\frac{1}{\|\vec{r}-\vec{r}'\|}dS'_B + \Phi_W\right). \tag{2.51}$$

When the boundary conditions are applied to the resulting equation is:

$$\hat{n}_{\vec{r}}\cdot(\vec{V}_G + \vec{V}_{Gp} + \vec{\Omega}\times\vec{r}_{Gp} - \nabla\times\vec{\Psi}) = \hat{n}_{\vec{r}}\cdot\nabla\left(\frac{1}{4\pi}\int_{S_B} \sigma(\vec{r}')\frac{1}{\|\vec{r}-\vec{r}'\|}dS'_B + \Phi_W\right). \tag{2.52}$$

Solving for the strength of the source distribution $\sigma(x')$, one can back substitute into equation 2.49 or 2.50 to obtain a relationship for the potential in the domain.

The Indirect Neumann-Doublet Membrane BIE

The Indirect Neumann-Doublet BIE is an identical formulation to that used in a doublet lattice type code[113]. The potential is defined as:

$$\phi(\vec{r}) = \frac{1}{4\pi}\int_{S_B} \mu(\vec{r}')\frac{\partial\phi}{\partial n}\left[\frac{1}{\|\vec{r}-\vec{r}'\|}\right]dS'_B, \tag{2.53}$$

where, $\mu(\vec{r}')$ is the boundary surface distribution of dipole or doublet strength. In order to once again add generality, one can explicitly incorporate the superposition of any other

solutions of Laplace's equation:

$$\phi(\vec{r}) = \phi_B(\vec{r}) + \Phi_W = \frac{1}{4\pi}\int_{S_B} \mu(\vec{r}')\frac{\partial \phi}{\partial n}\left(\frac{1}{\|\vec{r}-\vec{r}'\|}\right) dS'_B + \Phi_W. \tag{2.54}$$

The boundary conditions given in equation 2.3 are applied to give:

$$\hat{n}_{\vec{r}} \cdot (\vec{V}_G + \vec{V}_{Gp} + \vec{\Omega} \times \vec{r}_{Gp} - \nabla \times \vec{\Psi}) = \hat{n}_{\vec{r}} \cdot \nabla \left(\frac{1}{4\pi}\int_{S_B} \mu(\vec{r}')\frac{\partial \phi}{\partial n}\left(\frac{1}{\|\vec{r}-\vec{r}'\|}\right) dS'_B + \Phi_W\right). \tag{2.55}$$

The indirect Neumann-Doublet approach is particularly useful for lifting membrane applications. For example, thin fabric or membrane structures are difficult to model well with a source-doublet type approach due to the need for panel elements which are of comparable size to the thickness of the membrane. Instead, the Neumann doublet membrane formulation approximates the thin surface using a single sheet of doublet singularities which do not have strict limiting constraints as the Dirichlet approach.

2.3 The Pressure-Velocity Relationship

The Bernoulli Equation is used to determine the forces and pressures on the body. Since a potential-vorticity approach is used, the applicable unsteady Bernoulli equation is derived[113]. The incompressible Euler equations are:

$$\frac{\partial \vec{U}}{\partial t} + \vec{U} \cdot \nabla \vec{U} = -\frac{\nabla p}{\rho}. \tag{2.56}$$

If those regions of the flow which have zero vorticity (all of space excluding the trailing vortex wake region) are considered, the resulting equation is:

$$\frac{\partial \vec{U}}{\partial t} + \frac{1}{2}\nabla|\vec{U}|^2 = -\frac{\nabla p}{\rho}. \tag{2.57}$$

The definition of the velocity, given by equation 2.8, can be substituted into equation 2.57 resulting in:

$$\frac{\partial(\nabla\phi + \nabla \times \vec{\Psi})}{\partial t} + \frac{1}{2}\nabla|\nabla\phi + \nabla \times \vec{\Psi}|^2 = -\frac{\nabla p}{\rho}. \tag{2.58}$$

Collecting like terms, and re-arranging:

$$\frac{\partial(\nabla \times \vec{\Psi})}{\partial t} + \nabla \frac{\partial \phi}{\partial t} + \frac{1}{2}\nabla|\nabla\phi + \nabla \times \vec{\Psi}|^2 + \nabla\left(\frac{p}{\rho}\right) = 0. \tag{2.59}$$

Integrating eqn. 2.59 along the streamline from surface point x_1, to a farfield reference point at ∞ (where at $\vec{R} = \infty$, $\vec{U}_{t=0\to t_\infty} = 0$, and $p = p_\infty$) results in:

$$\int_\infty^{p_{x_1}} \frac{\partial(\nabla \times \vec{\Psi})}{\partial t} \cdot d\vec{C} + \left(\frac{\partial \phi}{\partial t}_{x_1} + \frac{1}{2}|\nabla\phi + \nabla \times \vec{\Psi}|^2_{x_1}\right) = \frac{p_\infty - p_{x_1}}{\rho}. \tag{2.60}$$

Furthermore, note that the term $\frac{\partial \phi}{\partial t}$ in equation 2.60 is defined in an Eulerian reference frame. The change in potential with respect to time for a point on the body surface can be computed by converting to a body Lagrangian reference frame:

$$\frac{\partial \phi}{\partial t}|_{Eulerian} = \frac{\partial \phi}{\partial t}|_{body} - (\vec{V}_G + \vec{V}_{Gp} + (\vec{\Omega} \times \vec{r}_{Gp})) \cdot \nabla\phi \tag{2.61}$$

The overall Unsteady Bernoulli equation is therefore:

$$\begin{aligned}\frac{p_\infty - p_{x_1}}{\rho} = &\int_\infty^{p_{x1}} \frac{\partial(\nabla \times \vec{\Psi})}{\partial t} \cdot d\vec{C} + \frac{\partial \phi}{\partial t}|_{body} - \\ &(\vec{V}_G + \vec{V}_{Gp} + (\vec{\Omega} \times \vec{r}_{Gp})) \cdot \nabla\phi + \frac{1}{2}|\nabla\phi + \nabla \times \vec{\Psi}|^2.\end{aligned} \tag{2.62}$$

The unsteady term due to the domain vorticity:

$$\int_\infty^{p_{x1}} \frac{\partial(\nabla \times \vec{\Psi})}{\partial t} \cdot d\vec{C}, \tag{2.63}$$

is difficult to handle in the form written above. By considering the contribution of the vortex wake as an analogous contribution due to a dipole sheet, one can write:

$$\int_\infty^{p_{x1}} \frac{\partial(\nabla \times \vec{\Psi})}{\partial t} \cdot d\vec{C} = \int_\infty^{p_{x1}} \frac{\partial \varphi}{\partial t}|_{wake} \cdot d\vec{C}. \tag{2.64}$$

Integrating the expression for the wake potential φ is simple:

$$\int_{\infty}^{p_{x1}} \frac{\partial \varphi}{\partial t}|_{wake} \cdot d\vec{C} = \frac{\partial \varphi}{\partial t} = \frac{\partial \varphi}{\partial t}|_{body} - (\vec{V}_G + \vec{V}_{Gp} + (\vec{\Omega} \times \vec{r}_{Gp})) \cdot \nabla \varphi \tag{2.65}$$

where, $\nabla \varphi$ is simply the velocity due to the wake. The overall Unsteady Bernoulli equation is therefore:

$$\frac{\partial \varphi}{\partial t}|_{body} + \frac{\partial \phi}{\partial t}|_{body} - (\vec{V}_G + \vec{V}_{Gp} + (\vec{\Omega} \times \vec{r}_{Gp})) \cdot \nabla(\phi + \varphi) + \frac{1}{2}|\nabla\phi + \nabla \times \vec{\Psi}|^2 = \frac{p_\infty - p_{x_1}}{\rho}. \tag{2.66}$$

The above expression for the change in potential due to the wake can be examined from an order of magnitude argument. For finite wing-only simulations the term is small (see figure 2-3 for a pictorial argument). Although the contribution to the pressure from the vortex

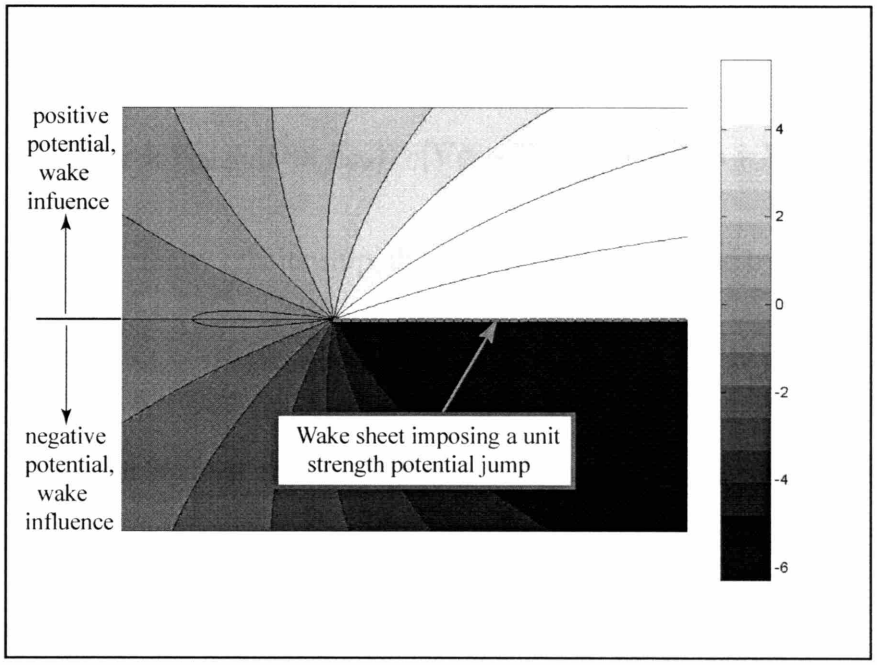

Figure 2-3: A plot of the potential due to a unit strength wake trailing behind an airfoil. The wake extends 50 chord lengths behind the airfoil and is not shown in entirety. Notice that the potential contribution to the airfoil is nearly zero due to the airfoil lying nearly in plane with the wake sheet. For airfoils, the change in potential due to the wake in an unsteady computation is a perturbation of an already small potential influence. In a scaling argument, one can argue that the change in potential due to the wake is negligible for many simulations (especially for thin airfoils).

wakes in many cases is small, for certain cases the order of magnitude of the unsteady

wake potential contribution is similar to the other contributions in the pressure calculation. This tends to occur when the wake passes above or below a downstream surface. In these cases, one can compute the unsteady pressure contribution of the domain vorticity on the body by solving the linear BIE system for the interior to the body wake potential:

$$\varphi(\vec{r}) = \frac{1}{4\pi}\int_{S_b'} \frac{\partial \varphi}{\partial n_{\vec{r}'}}(\vec{r}')\frac{1}{\|\vec{r}-\vec{r}'\|}dS_b' - \frac{1}{4\pi}\int_{S_b'} \varphi(\vec{r}')\frac{\partial}{\partial n_{\vec{r}'}}\frac{1}{\|\vec{r}-\vec{r}'\|}dS_b', \tag{2.67}$$

where, the potential φ represents the potential due to the wakes at the body surface. The normal derivative of the wake potential is known at the surface by the velocity expression for the vorticity in the domain. By solving the boundary integral equation, the potential contribution due to the wakes on the surface of the body is determined. As a result, the unsteady Bernoulli's equation for the pressure at the surface of the body is:

$$\begin{aligned}\frac{p_\infty - p_{x_1}}{\rho} =& \frac{\partial \varphi}{\partial t}|_{body} + \frac{\partial \phi}{\partial t}|_{body} - \\ & (\vec{V}_G + \vec{V}_{Gp} + (\vec{\Omega}\times\vec{r}_{Gp}))\cdot[\nabla\phi + \nabla\times\varphi] + \frac{1}{2}|\nabla\phi + \nabla\times\vec{\Psi}|^2.\end{aligned} \tag{2.68}$$

From this pressure-velocity relationship, the forces can be computed by integration:

$$\vec{F}(t) = \int_{S(t)} (p_\infty - p_{x'}(t))\,\hat{n}\,dS'(t). \tag{2.69}$$

Similarly, the moments about the body reference frame origin can also be computed by integration:

$$\vec{M}(t) = \int_{S(t)} \vec{r}'_{Gp}\times[(p_\infty - p_{x'}(t))\,\hat{n}]\,dS'(t). \tag{2.70}$$

2.4 The Wing Trailing Edge Kutta Condition

Most surfaces with sharp geometric cusps will produce forces when the body moves relative to a fluid. This net force is due to the viscous nature of fluids which prevents flows from traveling around these cusps. Rather, the flow will tend to separate from a sharp corner and shed a trailing shear wake. Since the flow is assumed to be inviscid, the production of forces requires an additional condition on the governing equations. In this thesis a Kutta

condition [9] is applied at all wing trailing edges. The Kutta condition prescribes a finite surface potential jump discontinuity across the geometric cusp, thereby resulting in smooth and finite trailing edge velocities. In order to assure the potential jump at the trailing edge, a fictitious wake surface is introduced into the domain. The wake surface is considered as a cut in the fluid domain capable of sustaining a potential discontinuity. Both a linear and non-linear Kutta condition have been considered in different formulations presented in this thesis.

The non-linear Kutta condition requires that there be no pressure jump across the trailing edge [72, 73, 74]:

$$p_{upper} - p_{lower} = 0, \tag{2.71}$$

Which, for an unsteady flow is:

$$\left[\frac{\partial\varphi}{\partial t}|_{body} + \frac{\partial\phi}{\partial t}|_{body} - (\vec{V}_G + \vec{V}_{Gp} + (\vec{\Omega}\times\vec{r}_{Gp}))\cdot[\nabla\phi + \nabla\times\varphi] + \frac{1}{2}|\nabla\phi + \nabla\times\vec{\Psi}|^2\right]_{upper} -$$
$$\left[\frac{\partial\varphi}{\partial t}|_{body} + \frac{\partial\phi}{\partial t}|_{body} - (\vec{V}_G + \vec{V}_{Gp} + (\vec{\Omega}\times\vec{r}_{Gp}))\cdot[\nabla\phi + \nabla\times\varphi] + \frac{1}{2}|\nabla\phi + \nabla\times\vec{\Psi}|^2\right]_{lower} = 0, \tag{2.72}$$

and for a steady flow, the above expression simplifies to:

$$\frac{1}{2}\rho|\vec{U}|^2_{upper} - \frac{1}{2}\rho|\vec{U}|^2_{lower} = 0, \tag{2.73}$$

where, $\vec{U}$ in equation 2.73 is the total velocity of the fluid relative to the trailing edge. A linearized version of the steady pressure continuity condition at the trailing edge is also considered for use in certain formulations. The linearized, steady, Kutta condition provides a rapid means to compute the potential jump [123],

$$\phi_{upper} - \phi_{lower} = \Delta\phi_{wake}. \tag{2.74}$$

Here, the subscripts $upper$ and $lower$ refer to points on the upper and lower surfaces of the trailing edge of the wing. This linearized Kutta condition assumes the fluid flows in a direction normal to the trailing edge cusp. For most applications this is an adequate assumption,

however, for highly loaded, low aspect ratio, or highly swept wings this linearization will be inaccurate. Furthermore, although this Kutta condition performs well as a first approximation for unsteady lifting flows, it should be cautioned that highly unsteady flows will not be accurately modeled.

For membrane flows, a condition which imposes no trailing edge vorticity has been implemented. The condition requires that the lifting surface potential jump at the trailing edge be equal to the potential jump imposed by the wake at the trailing edge:

$$\Delta\mu_{wing} = \Delta\mu_{wake}. \tag{2.75}$$

Equation 2.75 requires that there be no net vorticity capable of turning the flow around the trailing edge line.

For unsteady flows, any increase in bound vorticity on the wing must be balanced by an equivalent increase in vorticity in the wake. The formal statement for this condition (attributed to Kelvin [9]) is:

$$\left[\frac{d\Gamma_{span}}{dt}\right]_{wing} = -\left[\frac{d\Gamma_{span}}{dt}\right]_{wake}, \tag{2.76}$$

where Γ represents the circulation strength of the wing and body. In this relationship, Γ_{span} on the wing represents the integral of the bound vorticity. Therefore, in order to satisfy the above equation, the rate at which body bound vorticity increases must be equal in magnitude (but opposite in direction) to the rate of of vorticity shed into the wake. Satisfying the trailing edge Kutta condition of choice, and representing the domain vorticity using a vortex or doublet wake representation will result in the bound vorticity increase on the wing being appropriately accounted for in the wake.

2.5 Conclusions

This chapter presents the theoretical background for the potential flow solution framework. Considering the wake as either a potential influence (due to a dipole sheet) or a velocity influence (due to domain vorticity) proves valuable in the implementation of the panel

method. The Helmholtz decomposition of the fluid in the domain provides a means to represent the scalar and vector potential components of the flow independently, thus providing flexibility in the discretization.

Chapter 3

High Order, Curved Panel Integration

The justification for the use of curved panel, high order integration approaches is examined in the first section of the chapter; following that integration techniques for the self term, higher order, single and double layer potentials are presented.

3.1 Boundary Element Discretization

Discretizing the boundary integral equation involves approximations to both the boundary surface and the solution. In most boundary element methods the body is discretized into a series of triangular or rectangular panels. Over each of the panels, a basis function is used to represent the unknown quantity. Due to the discrete approximations, panel integrals such as the ones presented in equations 3.1-3.4 need to be evaluated for the discretization of interest:

$$\Phi_{\sigma}^{Panel} = \int_{S_{Panel}} \sigma(\xi', \eta') \frac{1}{\|x - x'\|} dS'_{Panel} \tag{3.1}$$

$$\Phi_{\mu}^{Panel} = \int_{S_{Panel}} \mu(\xi', \eta') \frac{\partial}{\partial n} \left[\frac{1}{\|x - x'\|} \right] dS'_{Panel} \tag{3.2}$$

$$V_{\sigma}^{Panel} = \nabla \left(\int_{S_{Panel}} \sigma(\xi', \eta') \frac{1}{\|x - x'\|} dS'_{Panel} \right) \tag{3.3}$$

$$V_{\mu}^{Panel} = \nabla \left(\int_{S_{Panel}} \mu(\xi', \eta') \frac{\partial}{\partial n} \left[\frac{1}{\|x - x'\|} \right] dS'_{Panel} \right) \tag{3.4}$$

Due to the singularity of the integral equation kernel under consideration, expressions for computing the above integrals when the evaluation point and the panel are coincident are not simple by nature. This section discusses the limitations of lower order basis functions as well as lower order geometry representations. In the sections which follow, several techniques for improving the discrete approximations using higher order techniques to remedy these drawbacks are presented.

3.1.1 Discussion of Orders of Approximation

In order to justify the investigation of higher order approaches a brief presentation of the limitations of some lower order approaches are presented.

1. *Convergence Rates*: One would expect that more accurate approximations of the boundary integral equation will produce more accurate computations. Care however must be taken to ensure that the surface discretization is consistent with the order of approximation of the solution in order to achieve optimal convergence for a given order of representation. Figure 3-13 illustrates the various convergence properties for a Green's Theorem solution of the potential around a unit sphere with successive grid refinements. A flat panel discretization of curved surfaces has an area which converges to the true area as $O(N^{-1})$, where N is the number of panels in the discrete approximation. As such, flat panel discretizations of curved surfaces at best will converge with an $O(N^{-1})$ rate due to the area's role in the discrete approximation. To achieve higher rates of convergence, a coupled approach in which higher order surface representations must be used in conjunction with higher order solution approximations. Several researchers have investigated higher order BEM approaches[115, 116, 117, 118, 119, 120, 121, 123, 124, 125, 111]; however, difficulties in evaluating the panel integrals prevent the more common use of these methods. In this chapter a set of high order curved panel integration approaches on curved panels will be presented.

2. *Velocity Calculations*: The accurate computation of velocity is important for computing the forces and moments. This is especially true for the potential based Green's

Theorem and Source-Doublet formulations. There are two approaches for computing the velocity:

(a) *Numerical differencing approaches for computing surface derivatives of the potential.* For the potential based computations (Green's Theorem and Source-Doublet formulations), the unknown is a potential. The surface gradient of the potential is the tangential velocity due to that potential. Computing the surface derivatives of the potential requires that either:

   i. The potential is represented using linear or higher order basis functions such that gradients in surface potential amount to differentiating the basis function representation of the solution,

   ii. The discrete elements are ordered in such a manner that finite difference approximations can be made.

(b) *Direct forward evaluation of the integral equations.* The forward evaluation of the boundary integral equation for the velocity is another option for velocity post processing. Figure 3-1 illustrates the evaluation of the velocity integral equation post-solution for a constant collocation solution. The velocity computed using the Green's Theorem BIE is visibly wrong. This arises due to the nature of the dipole representation. The constant dipole is equivalent to a vortex ring. The vortex ring represents the normal velocity accurately; however, close to the surface of the body the computation of the tangential derivative is increasingly different than physical reality. Figure 3-2 demonstrates the inconsistency with the constant basis dipole used for a tangential velocity calculation.

As a result of the desire for more accurate solutions with fewer panels as well as accuracy in the computation of velocities, pressures, forces and moments, higher order BEM approximations to the BIE's were investigated. This chapter presents some methodology which is a result of the investigations.

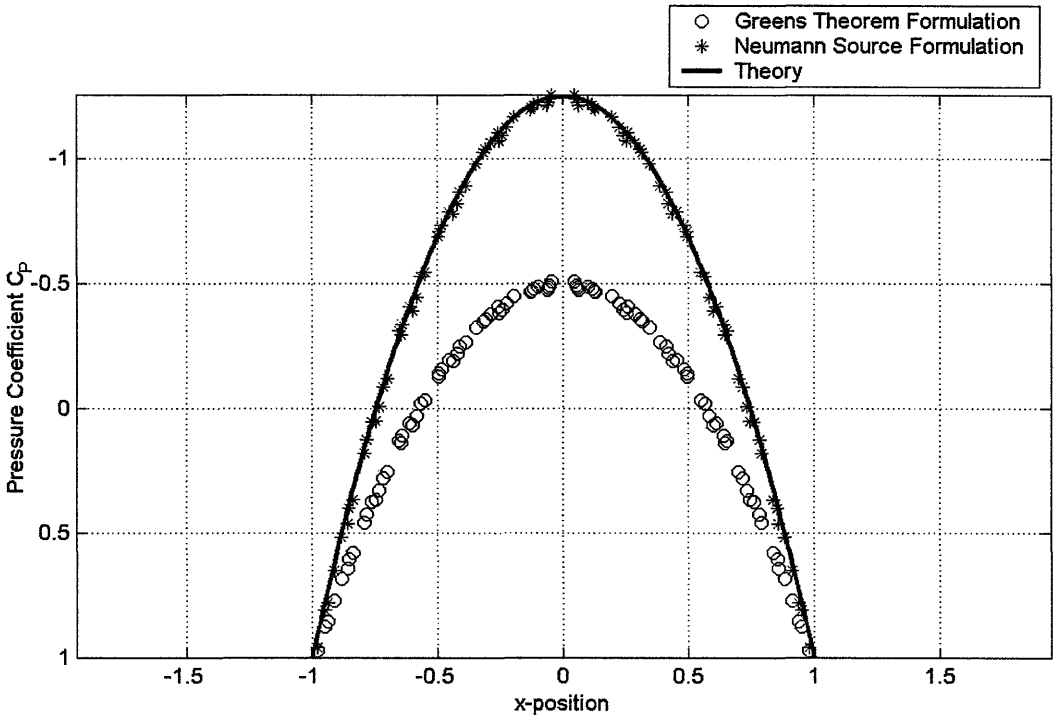

Figure 3-1: A comparison of the pressure around a sphere, computed using a source Neumann velocity formulation and a Green's theorem formulation. The velocity was computed using a forward evaluation of the boundary intergral equations. The result deomstrates the diminished accuracy of the Green's theorem approach.

3.1.2 Orders of Approximation

These approximations are made as follows:

1. **Surface Discretization**: The surface discretization is performed using a watertight surface triangulation. The majority of the results presented in this thesis were performed with a flat panel discretization of the surface, although, initial work presented in this chapter demonstrates several advantages of using curved element discretizations.

2. **Solution Discretization**: The solution discretization is performed using piecewise linear basis functions with solution continuity enforced. These C^0 continuous ele-

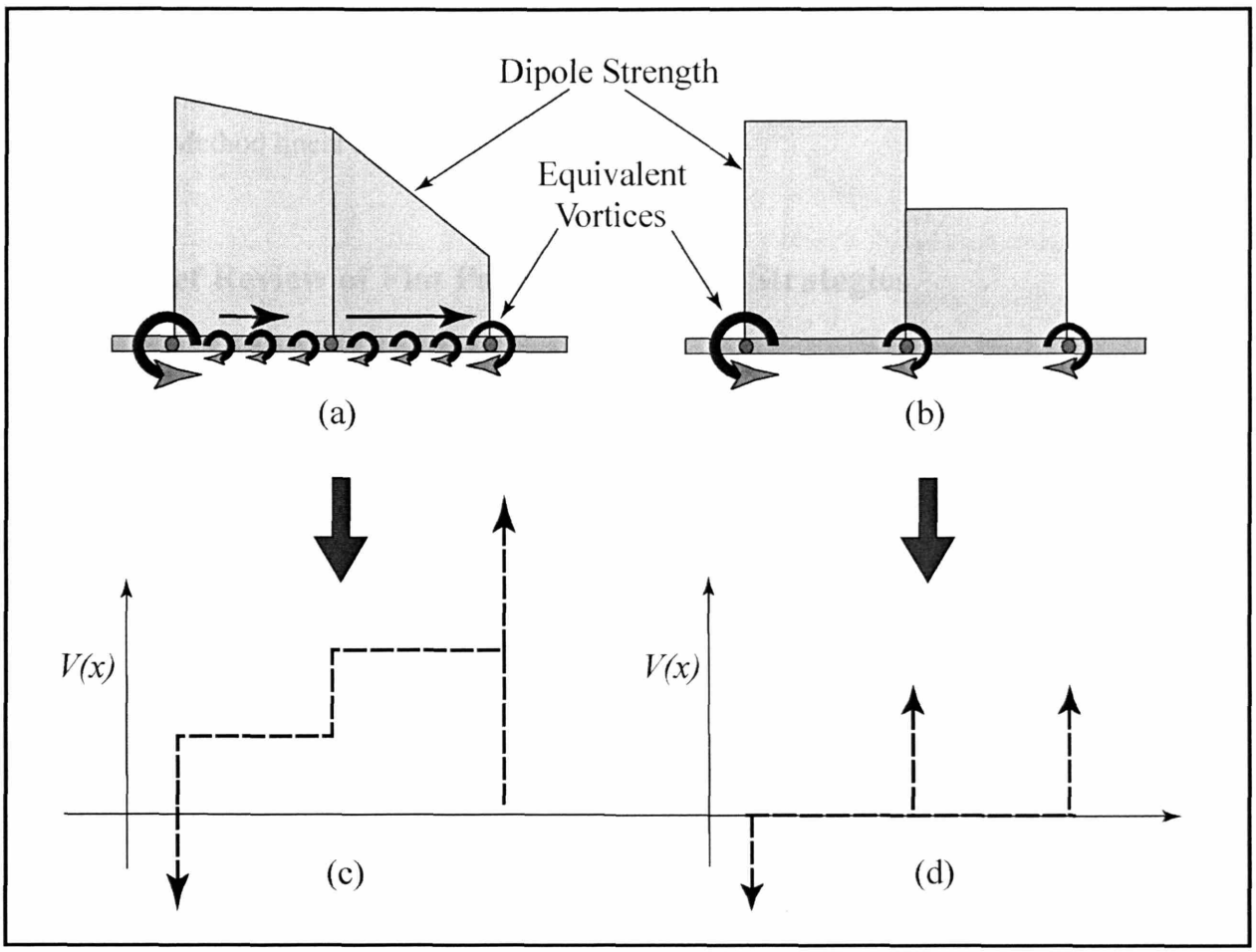

Figure 3-2: An illustration of the inconsistency of using constant doublet representations when modeling the tangential velocity close to a body when a forward evaluation of the BIE is used. (a) shows the linear dipole and the equivalent constant vorticity distribution on a surface, (b) shows the same for a constant dipole and the equivalent point vortices, (c) shows the tangential velocity computed a small ϵ above the surface for the linear dipole distribution, while (d) shows the tangential velocity due to the constant distribution of doublets. Notice, in (d) the tangential velocity at the wall of the body is zero at all locations except for locations where there is a discontinuous jump in doublet strength. There the velocity is infinite. As the evaluation point tends away from the surface, the velocity in (d) will approach the velocity in (c), however, on average this occurs after several panel lengths away from the surface. The difficulty with computing the tangential velocity arises due to the poor approximation of tangential velocity self term for constant dipole panels. As such, linear or higher order dipole distributions are recommended

ments are similar in nature to those used in the finite element community [126]. In addition quadratic basis function approaches are presented in this chapter.

By discretising the surface geometry into a set of flat panels with associated compact support basis functions, the Boundary Integral Equations presented in Chapter 2 form a Boundary Element Method linear system of equations.

3.1.3 Brief Review of Flat Panel Integration Strategies

In their paper on panel methods, Hess and Smith [13] proposed several analytical formulas for computing panel integrals for sources and doublets. Later, Newman [112] proposed a more general framework for the computation of analytical formulas over flat panel polygons. The framework proposed by Newman included a proposed recursive algorithm for the integration of higher order polynomials over flat polygons. The recursive formulas are presented in more detail by Wang [111]. Although Hess, Smith [13], Newman [112], and others have proposed formulas for the analytical integration, numerical approaches do exist. Based on adaptive quadrature schemes, these methods are typically more expensive for computing the self term integrals. Some examples of these approaches for both flat and curved panels can be found in [128, 129, 130, 131, 132, 133].

3.2 Integration Approaches for Quadratic Basis Functions on Quadratic Curved Panels

The geometry is described using parametrized triangular quadratic patches [126]:

$$X(\xi,\eta) = a_x\xi^2 + b_x\eta^2 + c_x\xi\eta + d_x\xi + e_x\eta + f_x \tag{3.5}$$

$$Y(\xi,\eta) = a_y\xi^2 + b_y\eta^2 + c_y\xi\eta + d_y\xi + e_y\eta + f_y \tag{3.6}$$

$$Z(\xi,\eta) = a_z\xi^2 + b_z\eta^2 + c_z\xi\eta + d_z\xi + e_z\eta + f_z \tag{3.7}$$

The coefficients a_i through f_i are determined from the nodes defining the curved panel patch. The representation of the parametrization is shown in figure 3-3. Parametric quadratic basis functions are used such that the patch geometry definition is consistent with the basis

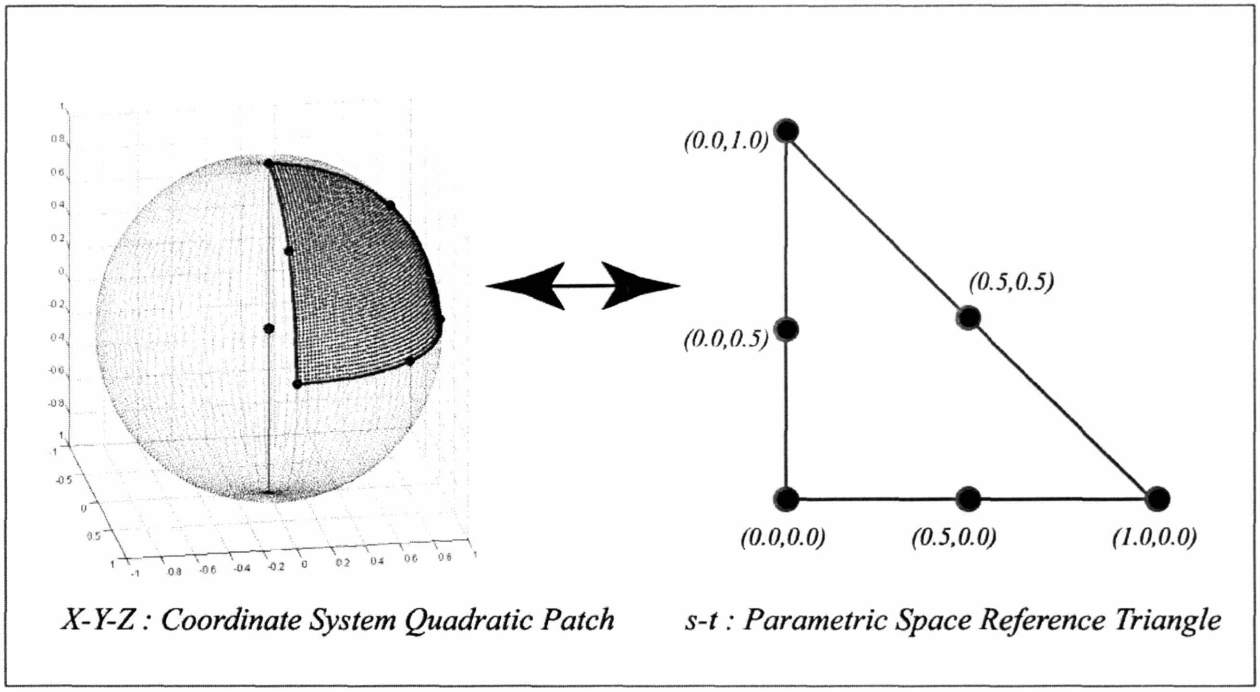

Figure 3-3: The relationship between the quadratically curved panel and the flat parametric triangle. The curved panel in this example is a $\frac{1}{8}$ segment of a sphere.

function definition [126]. These basis functions for a given panel are presented pictorially in figure 3-4.

3.3 Panel Integration Approaches for Non-Self Term Integrals

High order methods currently consider adaptive quadrature schemes[115], expansions[119] and semi-analytical approaches [111, 121] for the evaluation of curved panel integrals. Nearby non-self term panel integrals can easily be computed using the method developed by Wang et al.[111]. The far field interactions can be computed using a quadrature approximation. Although the Wang et al. method is used for nearby panels, it should be noted that the methods presented in this chapter for the self term integrals can be extended to compute the non-self term integrals; however, they are typically less efficient than the Wang et al. approach. The Wang et al. method does not work well for the self term evaluation in this quadratic panel method due to:

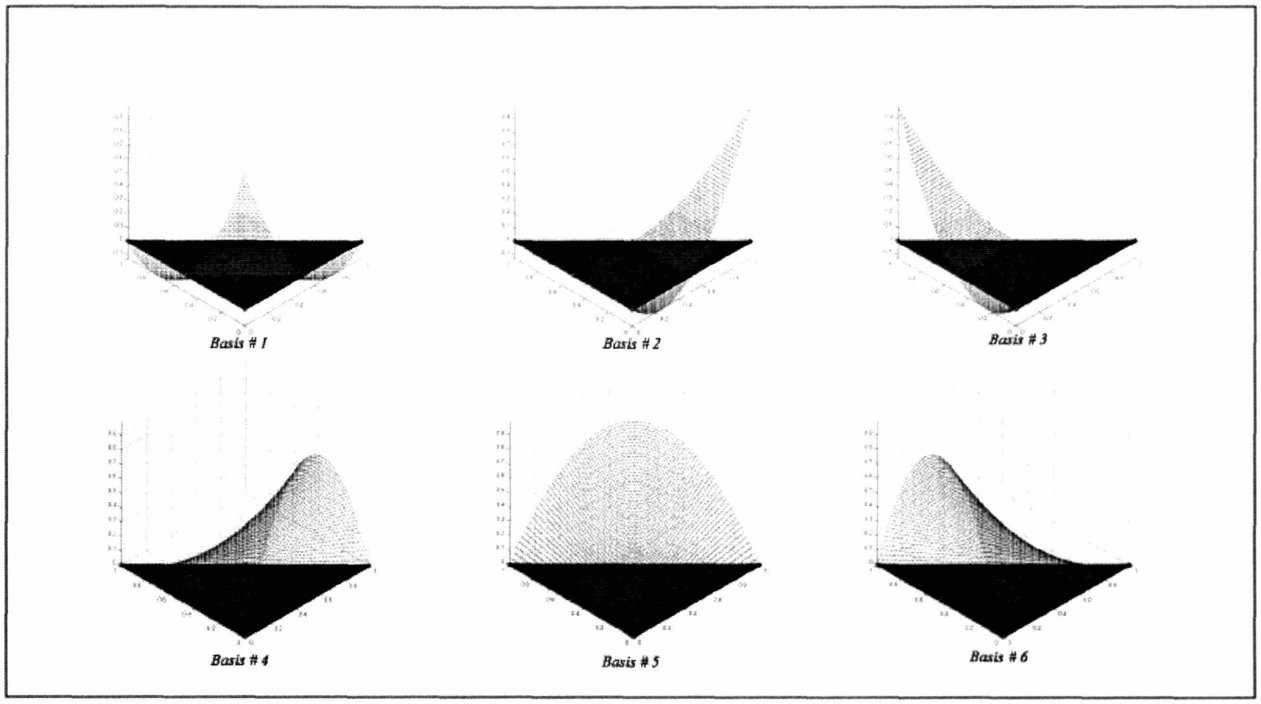

Figure 3-4: The 6-quadratic basis functions on the reference triangle.

1. The inability to form a ratio between the double layer kernel for a flat panel and the double layer kernel for a curved panel. This is shown below in the equivalent flat panel representation of the curved panel integral:

$$\Phi(x) = \int_{S_f} \mu(x') \frac{\partial}{\partial n} \left(\frac{1}{\|x - x'_f\|} \right) \left(\frac{\frac{\partial}{\partial n} \left(\frac{1}{\|x - x'_f\|} \right)}{\frac{\partial}{\partial n} \left(\frac{1}{\|x - x'_c\|} \right)} |J| \right) dS'_f, \tag{3.8}$$

   but:

$$K_{\frac{\partial}{\partial n}\left(\frac{1}{r}\right)} = \frac{\frac{\partial}{\partial n} \left(\frac{1}{\|x - x'_f\|} \right)}{\frac{\partial}{\partial n} \left(\frac{1}{\|x - x'_c\|} \right)} \tag{3.9}$$

   Is undefined at $x = x'$ and zero elsewhere. Hence, it is not possible to fit a polynomial accurately through this representation.

2. The difficulties associated with smoothly mapping non-constant radii of curvature to a flat, straight edged reference triangle. It is challenging to determine a mapping in which the self term curved-to-flat panel transformation is easily fitted with a polynomial in these cases. Although the Wang et al. method can be applied, unless more

complicated mapping approaches are considered, the accuracy of the approach will typically be diminished.

3.4 Panel Integration: The Self Term Integrals

Methods for quadratic basis function single and double layer self term integration have been developed for quadratically curved panels. These methods can easily be extended to higher orders.

3.4.1 Single Layer Integrals: The Self Term Integral

Although the self term integration for the single layer which is used is similar to the Wang et al. approach and those traditionally used[115], the differences introduced in this computation, albeit small, are important to improve the accuracy of the quadratically curved panel integrals.

Background Theory

The single layer potential self term integration is performed numerically after appropriately transforming the curved panel into a flat panel (with curved edges). Following the transformation, the panel integral is evaluated using quadrature in cylindrical coordinates. The transformation to cylindrical coordinates to desingularize the integrand was presented by Hess and Smith[122] in their analytical computation approaches for flat panel integrals, and the ideas have been further used in numerical implementations for higher order[115]. The background theory of the method used in this approach is described below:

1. Consider the integral governing the self term single layer on a curved panel:

$$\Psi(x) = \int_{S_c} \sigma(\xi'_c, \eta'_c) \frac{1}{\|x - x'_c\|} dS'_c, \tag{3.10}$$

where $\sigma(\xi', \eta')$ is the basis function representation of the single layer strength on the panel.

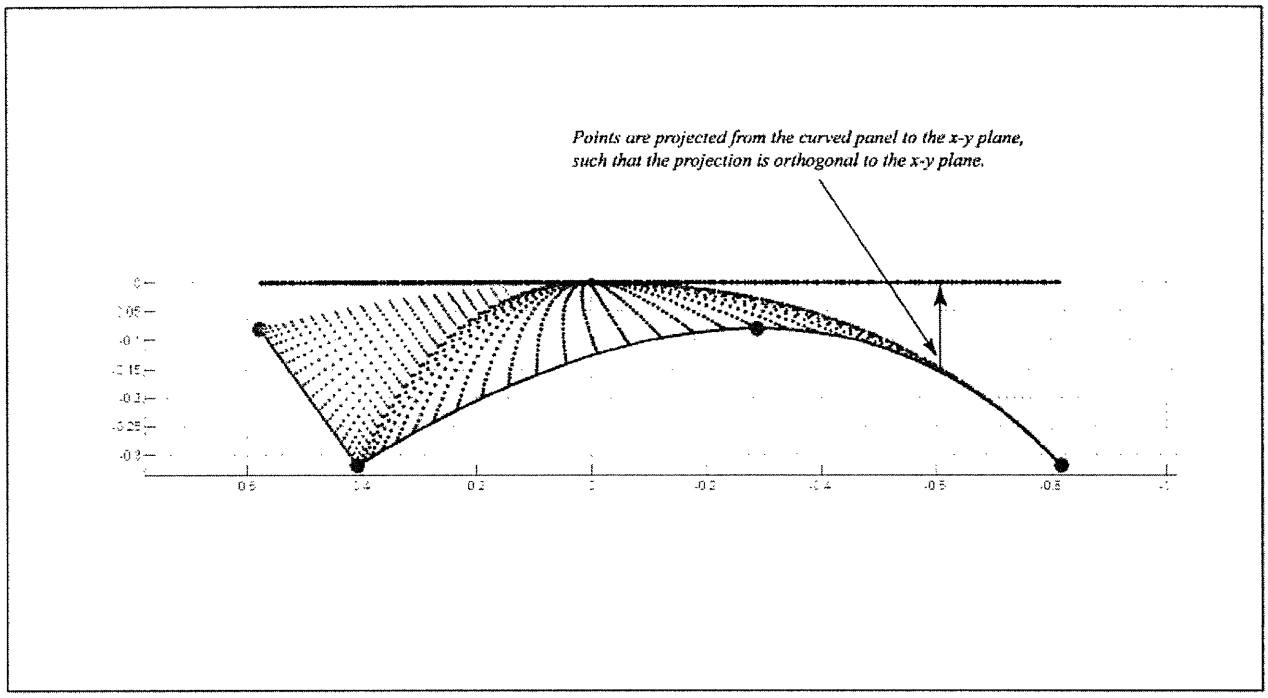

Figure 3-5: The orthonormal projection shown for a large selection of points on the curved panel to the tangent plane. Notice that the curved panel is projected onto the tangent plane in a manner that is normal to the tangent plane.

2. Project the curved panel geometry using an orthonormal projection onto the tangent plane at the evaluation point as shown in figure 3-5. As a result the integral over the flat tangent plane is:

$$\Psi(x) = \int_{S_f} \sigma(\xi_c', \eta_c') \frac{1}{\|x - x_c'\|} |J| dS_f', \tag{3.11}$$

where $|J|$ is the determinant of the Jacobian due to the orthonormal mapping. The value of $|J|$ evaluated across the flat panel will be smooth assuming large distortions are not encountered in the mapping.

3. As in the Wang et al. method [111], multiply and divide the integrand by $\frac{1}{\|x-x_f'\|}$:

$$\Psi(x) = \int_{S_f} \sigma(\xi_c', \eta_c') \frac{1}{\|x - x_f'\|} \left(\frac{\|x - x_f'\|}{\|x - x_c'\|} |J| \right) dS_f'. \tag{3.12}$$

4. Combine the basis representation polynomial ($\sigma(\xi_c', \eta_c')$) with the polynomial repre-

sentation of the mapping, into a single polynomial representation $Q(r'_f, \theta'_f)$, and the integral becomes:

$$\Psi(x) = \int_{S_f} Q(r'_f, \theta'_f) \frac{1}{\|x - x'_f\|} dS'_f \tag{3.13}$$

5. Equation 3.13 is then re-written in cylindrical coordinates as:

$$\Psi(x) = \int_{\theta=0}^{\theta=2\pi} \int_{r=0}^{r=R(\theta)} Q(r'_f, \theta'_f) \frac{1}{\|r'_f\|} \|r'_f\| d\theta' dr' \tag{3.14}$$

6. Which, when simplified becomes:

$$\Psi(x) = \int_{\theta=0}^{\theta=2\pi} \int_{r=0}^{r=R(\theta)} Q(r'_f, \theta'_f) d\theta' dr' \tag{3.15}$$

7. The resulting integral is simple to evaluate by first analytically integrating the polynomial $Q(r'_f, \theta'_f)$ in r, and then using one dimensional quadrature, for the remaining θ-integral. In cases where curved panels are significantly distorted or stretched, care should be taken as the polynomial fit will likely require significantly higher order polynomial representations for an accurate solution than when the panels are regularly shaped.

Implementation Approach

In order to implement the above approach, the following steps are used:

1. Transform the curved panel such that the tangent plane at the evaluation point lies in the $x_T - y_T$ plane, and the panel normal at the evaluation point is in the $+z_T$ direction, as shown in figure 3-6.

2. Determine a series of points on the curved panel which will be used to fit polynomial approximations to distribution on the panel. One can use any appropriate set of quadrature points; however, the polynomial fit will occur in $R - \Theta$ coordinates, and as such, an appropriate quadrature scheme might be similar to that used over 4-sided regions(with the sides of the rectangle being the R and Θ limits). In order to achieve a more accurate approximation to the integral, subdivision of the original panel into

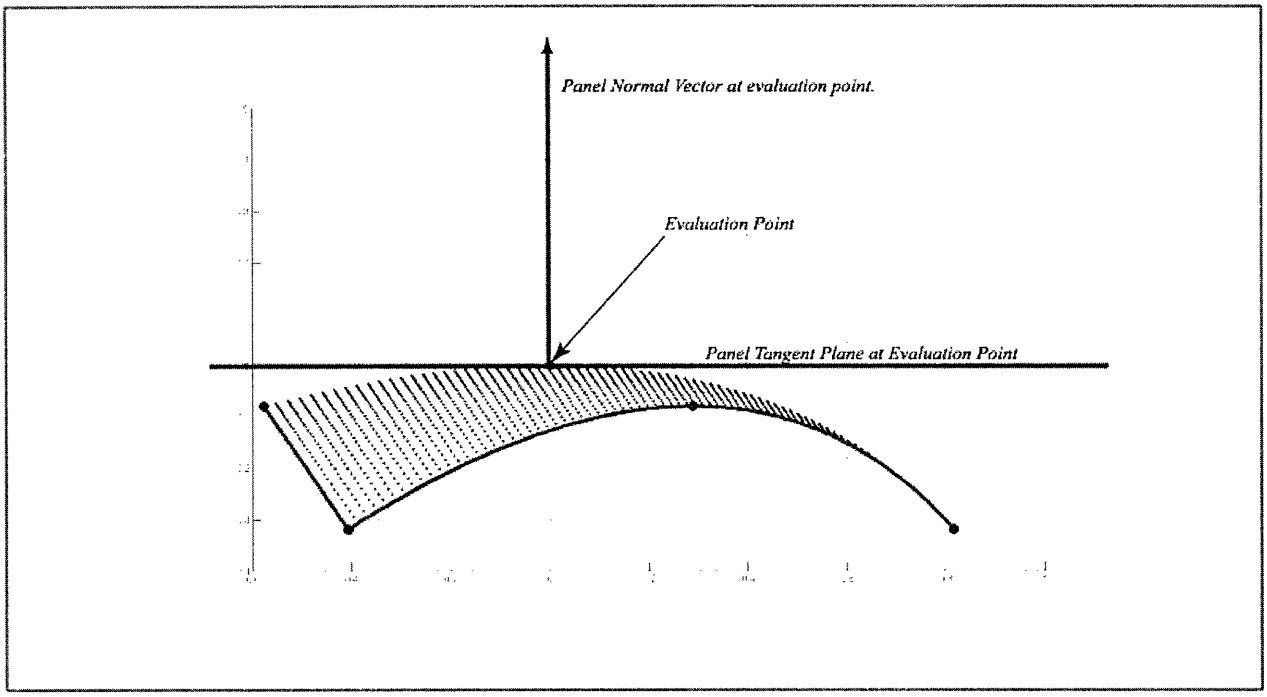

Figure 3-6: The panel after it has been appropriately transformed such that the tangent plane at the evaluation point is the $x_T - y_T$ plane, and the panel normal at the evaluation point is in the $+z_T$ direction.

three panels should be performed, where the subdivision occurs by connecting lines between the vertices and the evaluation point. Figure 3-7 demonstrates the points which will be used for the polynomial fit, as well as the division of the panel into three subpanels.

3. Orthogonally project the polynomial fit points onto the $x_T - y_T$ plane. One can also project the edges of the panel onto the $x_T - y_T$ plane. The projection of the curved panel edges and polynomial fit points onto the $x_T - y_T$ plane forms a flat reference panel for the integration. This projection is demonstrated in figure 3-8 and figure 3-5.

4. Compute the integrand, $Q(r'_f, \theta'_f)$ at the polynomial fit points, which is product of the following values:

   (a) The determinant of the Jacobian of the mapping between the curved panel and the orthonormal projection of the panel onto the $x_T - y_T$ plane. The expression

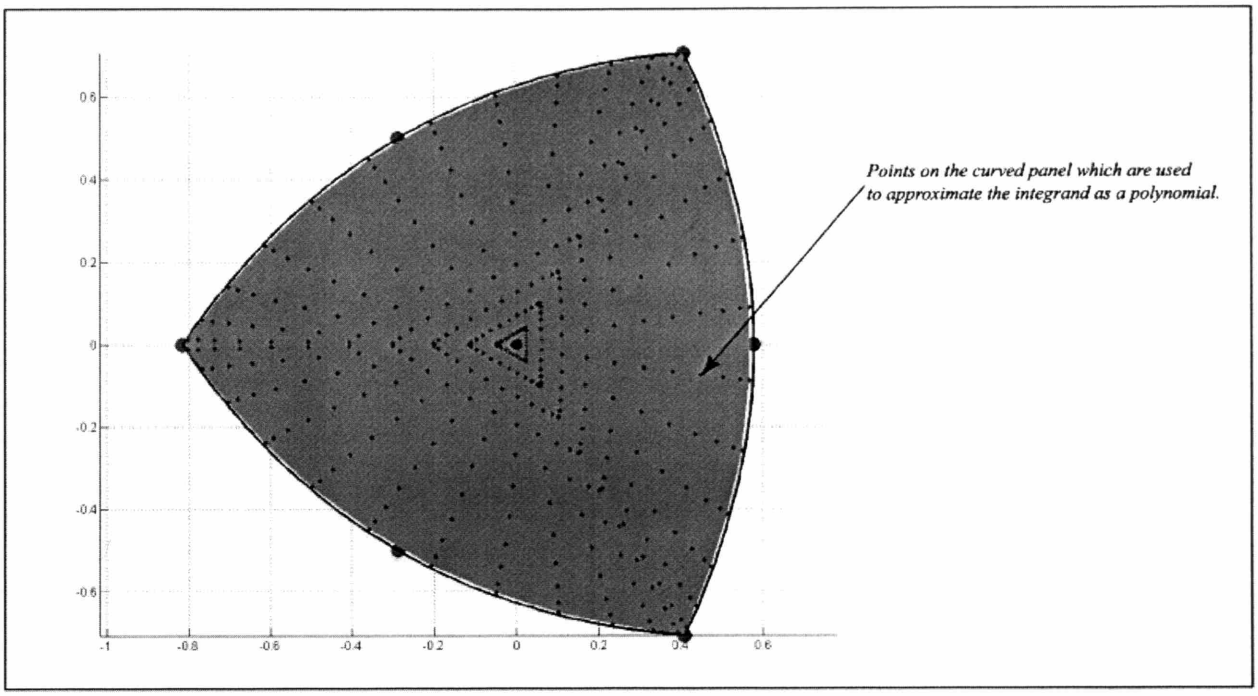

Figure 3-7: The points which are used to compute the polynomial approximation of the smooth integrand. Notice the polynomial fitting points are arranged in a manner that resembles a quadrature scheme for a degenerate quadrilateral. This apparent degeneracy will disappear once $R - \Theta$ coordinates are used. In addition, one should note the division of the panel into three subpanels. The layout of quadrature points and division of the panel is performed on the $\xi - \eta$ parametric triangle.

of the determinant can be found analytically for quadratic panels.

(b) The ratio between the kernel evaluated on the flat panel to the evaluation point and the kernel evaluated on the curved panel to the evaluation point.

(c) The Basis function value, $\sigma(r'_f, \theta'_f)$.

5. Compute a polynomial approximation to represent the integrand in the $R - \Theta$ coordinate system. This polynomial approximation is computed by a simple linear system solve (The right hand side vector contains the known values of the function, the system matrix is a Vandermonde matrix where the entries are evaluated at the polynomial fit points (in $R - \Theta$ coordinates), while the vector of unknowns contains the unknown polynomial coefficients).

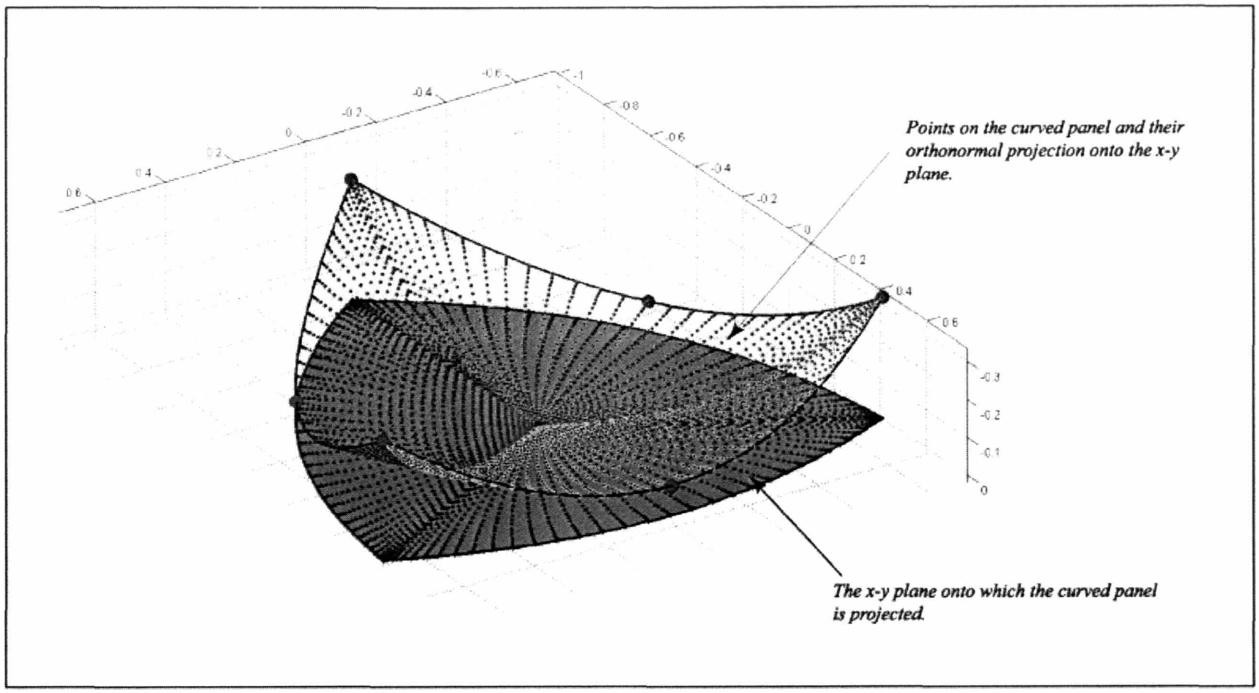

Figure 3-8: The orthonormal projection shown for a large selection of points on the curved panel. Note that the panel edges will not be straight lines in the general case. This is the fundamental difference between the Wang et al. method and the current method for computing the self term integration of the single layer.

6. Integrate the resulting polynomial in R analytically. The integrand of:

$$\Psi(x) = \int_{\Theta=0}^{\Theta=2\pi} \int_{r=0}^{r=R(\theta)} Q(r'_f, \theta'_f) dr d\theta' \tag{3.16}$$

is a polynomial representation in $R-\Theta$. As such, the integral is simply an appropriate coefficient multiplication and exponent augmentation. The integral becomes:

$$\Psi(x) = \int_{\Theta=0}^{\Theta=2\pi} U(R'_f(\theta'_f), \theta'_f) d\theta', \tag{3.17}$$

where $U(R'_f(\theta'_f), \theta'_f)$ is the polynomial resulting from integration. $R'_f(\theta)$ is the distance from the evaluation point to the flat panel edge for a given angle θ. This integral is merely an integration of $U(R'_f(\theta), \theta'_f)$ in θ around the edges of the panel.

7. Determine a quadratic parametric relation for the edges of the curved panel (a one-dimensional quadratic parametrization of the projected edge), such that in the param-

eter t the θ-integral becomes:

$$\Psi(x) = \int_{\Theta=0}^{\Theta=2\pi} U(R'_f(\theta), \theta'_f) d\theta' = \int_{t=0}^{t=1} U(R'_f(\theta'_f(t)), \theta'_f(t)) |J_{\theta \to t}| dt. \quad (3.18)$$

Since the above integral is computed numerically using quadrature, place quadrature points on the panel edges. These quadrature points are placed by mapping the Gauss quadrature points from the parametric representation to the curved edges.

8. Integrate the line integral numerically using the panel edge based quadrature routine.

The scheme presented for the single layer self term can be applied to arbitrary curved panels with high order basis functions. In addition, the method does not have the same limitations as the Wang et al. method due to the lack of restrictions on the reference panel edge shape. In the current method, the reference flat panel edges can be straight or curved lines. The curved panel self term single layer integration using the above process is simple from both an application and conceptual point of view.

3.4.2 Double Layer Integrals: The Self Term Integral

As with the single layer integration, the double layer self term integration approach we present is a conceptually simple numerical integration. Similar to the single layer, the approach we present for the double layer is not restricted simply to self term panels.

Background Theory

The double layer self term integral is performed through the implementation of some fundamental ideas presented in Kellogg [114] and later exploited in Newman [112]. The double layer expression is considered from a slightly different perspective as shown below:

$$\Phi(x) = \int_S \mu(x') \frac{\partial}{\partial n} \frac{1}{\|x - x'\|} dS', \quad (3.19)$$

where $\mu(x')$ is the basis function representation. If we re-write the expression as:

$$\Phi(x) = \int_S \mu(x')\hat{n} \cdot \left[\nabla\left(\frac{1}{\|x - x'\|}\right)\right] dS', \tag{3.20}$$

the expression in the square brackets can be regarded as the velocity at the panel surface integration point x' due to a point charge at x. Furthermore, if we assume that for now $\mu(x')$ is a unit constant distribution over the panel:

$$\Phi(x) = \int_S \hat{n} \cdot \left(\nabla\left(\frac{1}{\|x - x'\|}\right)\right) dS', \tag{3.21}$$

which is exactly the flux through the panel S' due to a point charge at x.

Since the point charge at x emits a divergence free velocity in a radial manner, we can equivalently say that the flux due to the point source which passes through the panel, is identical to the flux which passes through any radial projection of the panel (where the radial projection is centered at the point source which is also the evaluation point). If the panel is radially projected onto a unit sphere centered at the evaluation point, the integration is equivalent to determining the flux through a portion of a sphere defined by the radial projection of the panel. This is shown in figure 3-9.

The integral for the flux through the spherical patch formed by the radial projection of the panel (where the radial projection is centered at the evaluation point which lies at the origin) is expressed as:

$$\Phi(x) = \int_S \hat{n} \cdot \left(\nabla\left(\frac{1}{r}\right)\right) dS' = \int_S 1 \, dS' \tag{3.22}$$

Which is identically the area of the sphere onto which the projection of the panel acts. In order to compute higher order distributions a similar radial projection can be used. In the higher order approach, the basis function is considered as a weighting function on the flux through the panel due to the source point charge. In other words, both the panel and the basis function are projected onto the unit sphere in a radial projection. This is shown by considering equation 3.20.

The interpretation of the dipole integral here is a flux through the panel surface S, due

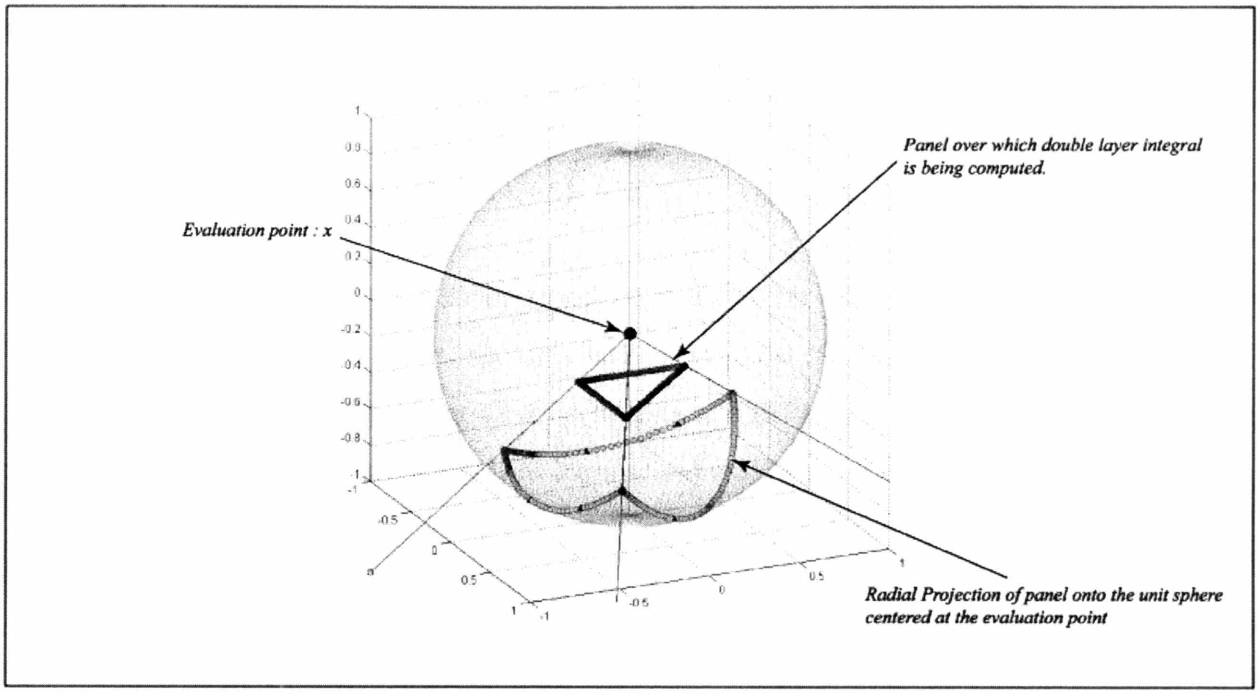

Figure 3-9: The radial projection of a flat panel onto the unit sphere centered at the evaluation point, x.

a point charge located at x, weighted with the basis function value $\mu(x')$ at the point x' at which the flux is being evaluated. Again, since the flux due to the source point charge is divergence free, this weighed flux for each point x' on the panel can be projected onto the unit sphere in a similar radial projection as before. The resulting integral becomes:

$$\Phi(x) = \int_S \mu(\theta, \phi)\hat{n} \cdot \left(\nabla\left(\frac{1}{r}\right)\right) dS' = \int_S \mu(\theta, \phi) dS' \tag{3.23}$$

Which is merely a calculation of the basis function weighted area of the radially projected panel onto the unit sphere.

A Note on the Self Term Double Layer Potential Integral

When the self term of the double layer potential integral over a surface is considered, care must be taken. Consider the double layer integral:

$$\Phi(x) = \int_S \mu(x') \frac{\partial}{\partial n} \frac{1}{\|x - x'\|} dS', \tag{3.24}$$

At $x = x'$, the integral is undefined. As such the point is excluded from the domain and the Cauchy Principle Value is evaluated, such that:

$$\Phi(x) = \pm 2\pi\mu(x) + \oint_S \mu(x') \frac{\partial}{\partial n} \frac{1}{\|x - x'\|} dS', \tag{3.25}$$

where the $\pm 2\pi\mu(x)$ term is the Cauchy Principle Value of the integral, the sign of which depends on the direction in which one approaches the panel (from above or below).The remaining integral is evaluated over all $x' \neq x$ points on the panel. In the section which follows, the evaluation of the integral is of interest and will be described.

Implementation Approach

The implementation of the integration of the double layer over curved panels is presented for quadratic basis functions; however, it should be noted that arbitrary order basis functions can be used. Furthermore, it should be noted that the constant basis computation is much less computationally complex than the higher order computations, since it amounts to computing the area of the sphere between the equator and the projection of the panel. This is a direct result of the fact that there is no varying basis distribution on the panel.

The following steps are performed to compute the double layer integral.

1. Transform the curved panel such that the tangent plane at the evaluation point lies in the $x_T - y_T$ plane, and the panel normal at the evaluation point is in the $+z_T$ direction, as shown in figure 3-6. Furthermore, translate the transformed panel such that the evaluation point lies at $(x_e, y_e, z_e) = (0, 0, 0)$.

2. Split the curved triangle into 6-sub triangles. These sub triangles are formed by:

   (a) Dividing the panel along lines joining the evaluation point and the vertices.

   (b) Dividing the panel along the lines joining the evaluation point and the nearest point on each of the panel edges (in the current implementation this is measured on the reference parameter based triangle).

3. Determine quadrature points on each of the six sub triangles. In addition to the points themselves, determine the basis function value at each of the points. These

quadrature points are determined based on quadrature rules applied to the $\xi - \eta$ parameter triangles and then mapped to the surface of the curved panel. As in the single layer self term computation, these points are used for the determination of a polynomial approximation, hence any appropriate distribution of points will be adequate. Again, we choose to use the quadrature rule for four-sided domains. Figure 3-10 demonstrates the splitting of the curved triangle and the placement of quadrature points.

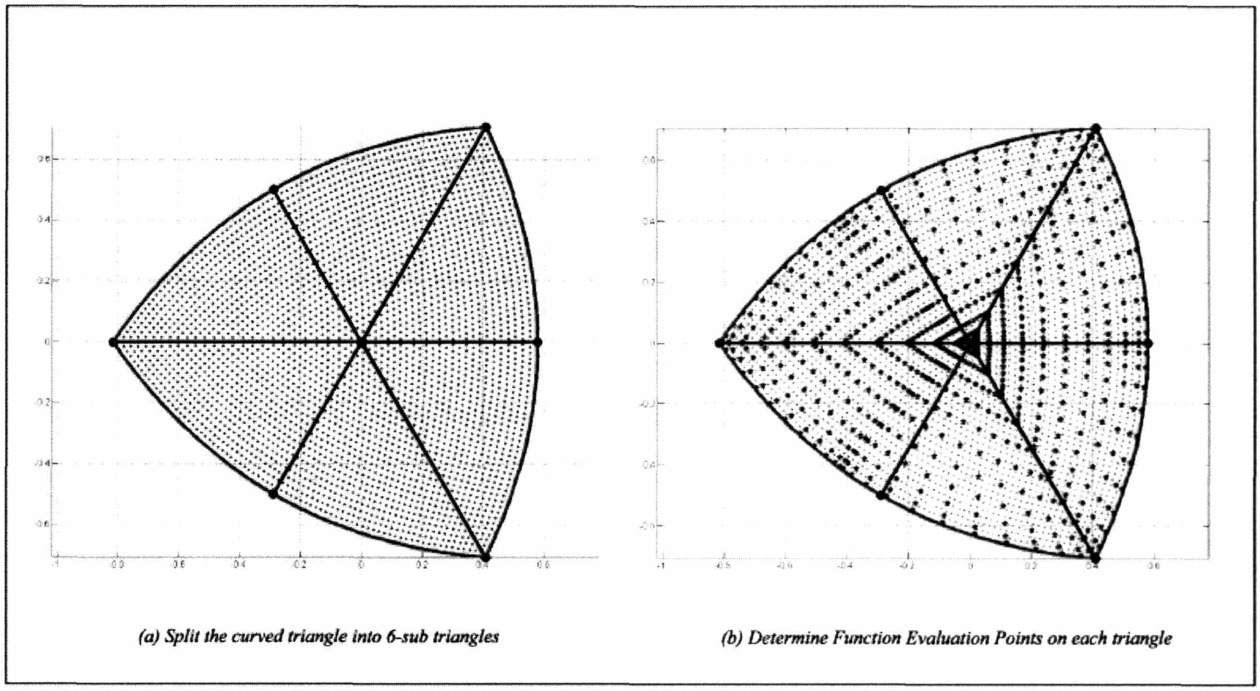

(a) Split the curved triangle into 6-sub triangles

(b) Determine Function Evaluation Points on each triangle

Figure 3-10: The 6-subtriangles illustrated on the curved panel. The illustration on the right shows the points which will be used in the polynomial approximation of the integrand after it is projected to the unit sphere.

4. Radially project the points on the panel onto the unit sphere. The points can be projected onto the unit sphere by:

$$P_S(x, y, z) = \frac{P(x, y, z)}{\|P(x, y, z)\|} \tag{3.26}$$

Note, since the integral in question excludes the point $x = x'$, the projection of the portion of the panel directly encircling the origin (which is the evaluation point), will lie on the equator of the sphere.

By radially projecting the panel onto a unit sphere centered at the evaluation point, the integral can be represented as:

$$\Phi(x) = \oint_S \mu(x') \frac{\partial}{\partial n} \frac{1}{\|x - x'\|} dS' \rightarrow \int_{\Theta=0}^{\Theta=2\pi} \int_{\Phi=0}^{\Phi=\phi(\Theta)} \mu(\phi, \theta) \frac{\partial}{\partial n} \left(\frac{1}{r}\right) r^2 \sin(\phi) d\phi d\theta \tag{3.27}$$

Which, when we consider the unit sphere ($r = 1$), becomes:

$$\Phi(x) = \int_{\theta=0}^{\theta=2\pi} \int_{\phi=\frac{\pi}{2}}^{\phi=\phi(\theta)} \mu(\phi, \theta) \sin(\phi) d\phi d\theta \tag{3.28}$$

If, the $\sin(\phi)$ term in the integrand is combined with the basis representation to give $P(\phi, \theta)$, the resulting integral expression is:

$$\Phi(x) = \int_{\Theta=0}^{\Theta=2\pi} \int_{\Phi=\frac{\pi}{2}}^{\Phi=\phi(\Theta)} P(\phi, \theta) d\phi d\theta \tag{3.29}$$

5. Determine the $\Phi - \Theta$ coordinates of each of the points.

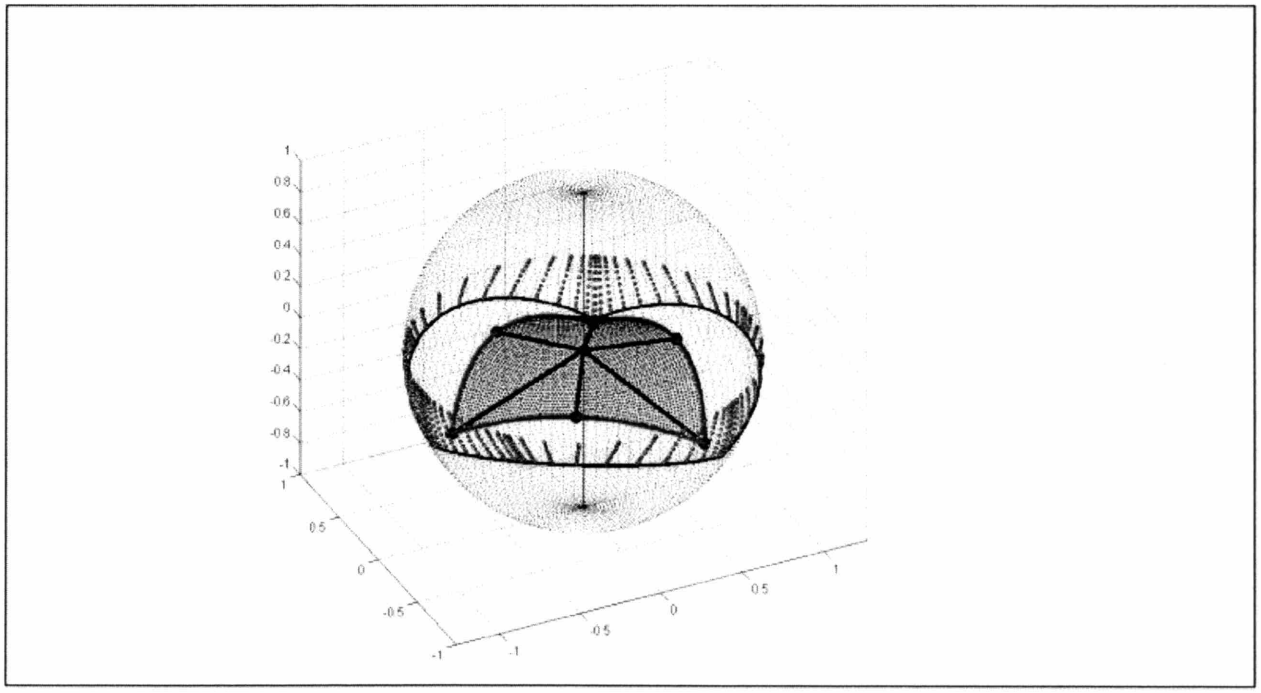

Figure 3-11: The radial projection of the points on the panel and the edges onto a unit sphere centered at the evaluation point.

6. Sort the projected points such that they lie within the Θ angles of the original curved panel subdivision.

7. For each of the 6 sub-triangles determine the polynomial approximation, $P(\phi, \theta)$, which best represents the basis function value as it is radially projected from the panel points to the points on the sphere.

8. Integrate the inner integral of the polynomial, $P(\phi, \theta)$, analytically in Φ:

$$\Phi(x) = \int_{\Theta=0}^{\Theta=2\pi} \int_{\Phi=\frac{\pi}{2}}^{\Phi=\phi(\Theta)} P(\phi, \theta) d\phi d\theta \rightarrow \Phi(x) = \int_{\Theta=0}^{\Theta=2\pi} Q(\phi(\Theta), \theta) d\theta \quad (3.30)$$

9. Integrate the remaining line integral using quadrature. The edge of the panel over which the line integral is being performed must be expressed as a quadratic line based on a parameter t. The integral to be computed then becomes:

$$\Phi(x) = \int_{t=0}^{t=1} Q(\phi(\Theta(t)), \theta(t)) |J|_{\theta \rightarrow t} dt, \quad (3.31)$$

which is easily computed using moderate orders of Gaussian quadrature in one dimension.

10. Since we are concerned only with evaluating the Cauchy Principle Value integral in this computation, in order to get the full influence of the self term, we add to this result the appropriate $\pm 2\pi\mu$ Cauchy Principle Value (CPV).

3.4.3 Potential Flow Around the Unit Sphere

In order to demonstrate the quadratic panel method arising from application of the integration techniques described, a series of solutions for the flow around increasingly refined unit spheres is presented. The potential flow around the unit sphere has an analytical solution for the perturbation potential which is given by[113]:

$$\phi = U_\infty \cos\theta \left(\frac{R^3}{2r^2} \right). \quad (3.32)$$

The simulations considered were run at $U_\infty = 1$, over unit radius ($R = 1$) spheres. The panel method approximations which are considered in the convergence comparison are:

1. Constant collocation on planar panels
2. Linear basis Galerkin on planar panels
3. Quadratic basis Galerkin on planar panels
4. Quadratic basis Galerkin on quadratic curved patches

The results of the quadratic curved panels are visibly superior to the constant collocation as presented in figure 3-12. The convergence of each of the methods to the analytical solution

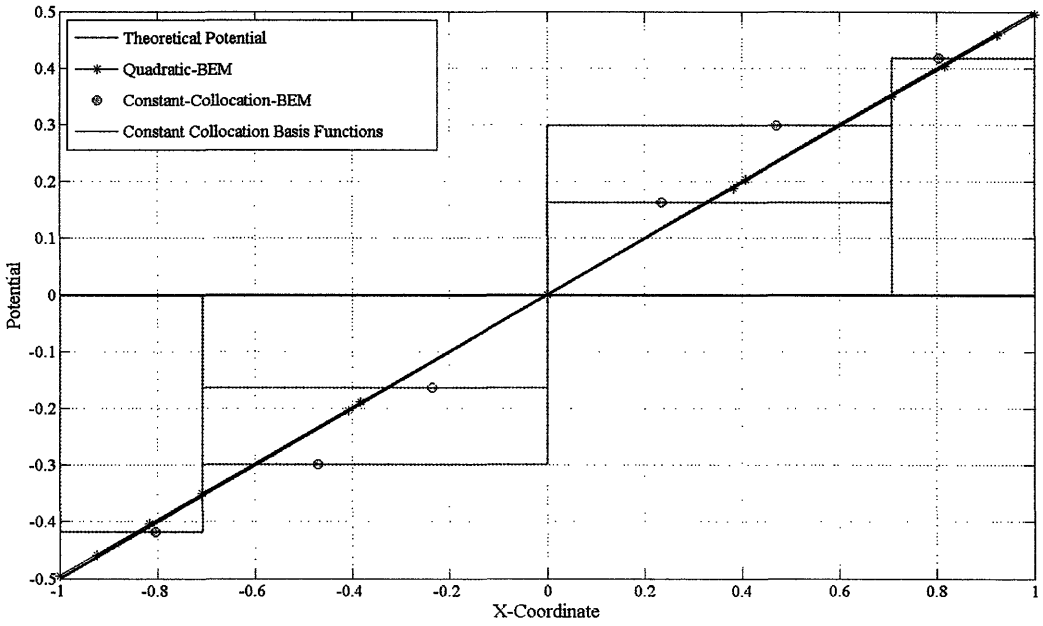

Figure 3-12: An illustration of the solution ϕ computed on a 32-panel sphere comparing constant basis function representations with quadratic basis functions on quadratic patches. The theoretical result is also plotted and coincides with the result from the high order panel method. For clarity in the depiction of the constant basis function results, both the potential value at the centroid and the basis function itself are represented on the plot. This further demonstrates that the constant basis approximation will have poor error convergence.

is demonstrated in figure 3-13. The error was computed for each panel and integrated using high order quadrature schemes. From figure 3-13, it can be seen that the highest

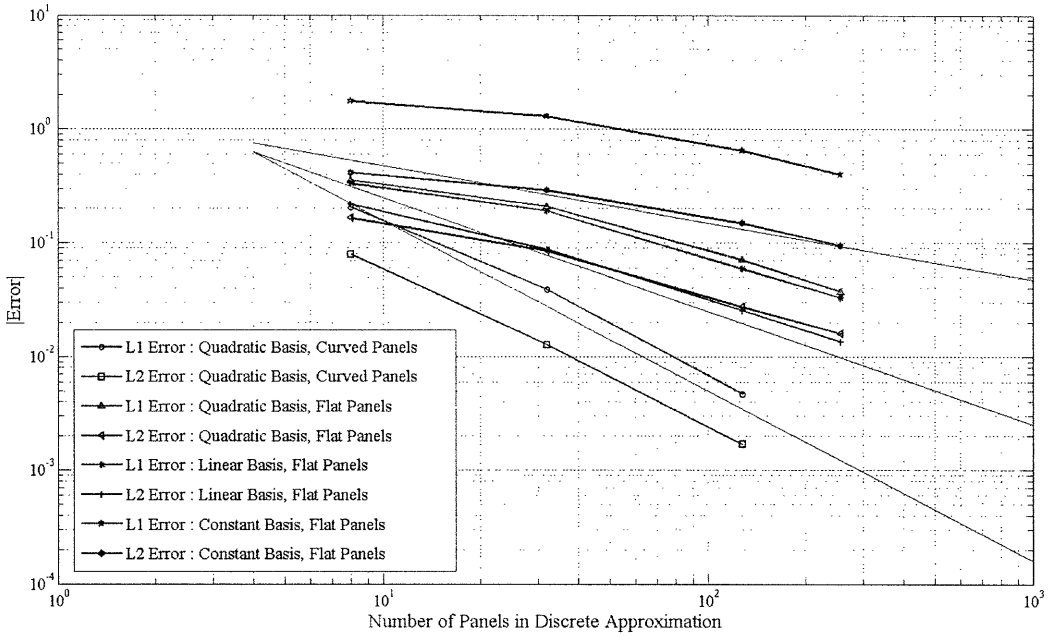

Figure 3-13: The error convergence of the potential for constant basis representation on flat panels, linear basis representation on flat panels, and quadratic representation on curved panels. The plots show L1 and L2 error integrated over the sphere using the underlying basis representation for the integration. Notice that the constant basis functions on flat panels converge at a rate of $O(N^{-\frac{1}{2}})$, the linear basis on flat panels at $O(N^{-1})$, the quadratic basis on flat panels at $O(N^{-1})$, and the quadratic basis on quadratic patches at $O(N^{-\frac{3}{2}})$.

convergence rate for flat panel discretizations is limited by the geometry convergence. This is realized when comparing the quadratic, linear and constant basis solutions when flat panel discretizations are used. The flat panel discretization surface area converges at a rate inversely proportional to the number of panels ($O(N^{-1}) = O(h^2)$), hence becomes the limiting convergence rate for the case. It is interesting to note that the results for the linear basis function representation are the most accurate of the set of computations done on flat panels. Although this may appear strange, it is consistent with the approximations being made. Quadratic basis functions will provide a more accurate solution to the discrete geometry (which is based on a flat panel representation), which in the case of a sphere or curved surface, is typically a worse approximation than the linear basis on flat panels.

The convergence results for the curved panel high order basis functions demonstrate that increased convergence rates can only be achieved if approximation order increases are

realized in both basis function approximation and surface discretization. If we consider the panel methods described, it would take a discretization on the order of $10^5 - 10^6$ constant basis flat panels to achieve the error levels displayed by a 128 curved panel high order method. Similarly, it would take on the order of 10^4 panels to reach that level of accuracy using linear basis functions on flat panels. From these results it can be seen that low panel counts using accurate geometry representations and high order basis functions can often lead to accuracy levels hard to achieve with flat panel lower order approaches.

3.5 Conclusion

The work presented in this chapter highlights the methods involved in computing panel integrals for the high order BEM representation and proposes approaches for integrating the self term integrals. It was found that the high order method, when compared on a number of panels basis was always significantly more accurate than the low order approaches.

Chapter 4

Wake Details

The explicit modeling of wake shear layers in panel methods often presents challenges. More specifically, the following challenges exist:

1. *Ensuring the wake position is representative of a physically realistic vorticity distribution*: The wake should evolve with the local freestream velocity, otherwise it is a force producing surface. Many panel methods require user specified wakes[106, 116], while several others [35, 107] incorporate wake roll-up and wake evolution routines. The wake roll-up routines often suffer from limitations associated with the use of panels to discretize the wake potential jump or vorticity.

2. *Satisfying a potential jump along the downstream portion of the body*: The wake represents a potential jump in the domain. This potential jump must also be present at the body-wake intersection. Since the potential jump in a domain discontinuity, meshing challenges will typically exist at wake-body intersections.

3. *Using appropriate models to deal with wake intersections and downstream lifting surfaces*: During unsteady motions, wakes may readily intersect with downstream surfaces. When a doublet wake intersects with a downstream surface, the solution of the potential flow will lose physical meaning. Although wake-body intersections are non-physical, they can often occur due to the nature of the discrete representation.

In this chapter, several techniques for more advanced and automatic wake modeling and evolution are presented.

4.1 Body Piercing Wakes

In traditional panel method approaches, the wing trailing potential jump is represented using a dipole sheet extending behind the wings and conforming to the downstream portions of any bodies, as demonstrated in figure 4-1. The dipole wake sheets induce a potential

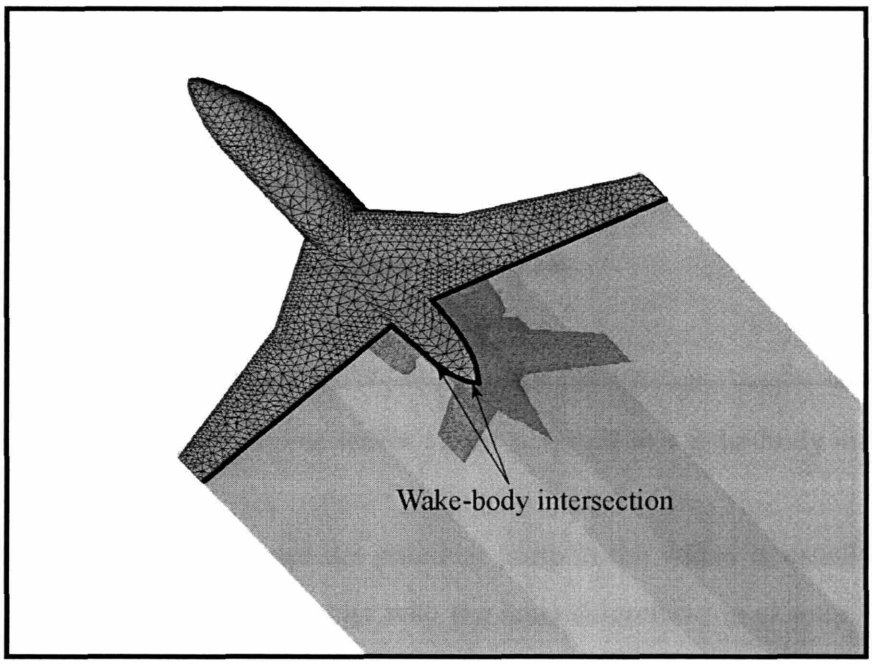

Figure 4-1: A pictorial representation of the Green's Theorem formulation of the Boundary Integral Equation.

jump in the domain across the thin trailing wake. For potential based solutions, such as the source-doublet formulation, wake-body intersections must be carefully treated to preserve and accurately model the potential jump. In order to do this, the wake sheet must be abutted to the body and form an impermeable intersection (The wake should align exactly with the fuselage). The result is a large potential jump along the wake-body intersection. This is illustrated in figure 4-2. When the velocity is computed, the effect of the potential jump along the side of the body cancels with the effect of the potential jump due to the wake. As such, the velocity at all points on the body is smooth. When determining the velocity near the wake-body intersection, a limiting process must be used such that the velocity evaluation point never coincides with the triple point intersection of the wake and fuselage.

Significant constraints on wake-body meshing are imposed through the use of dipole

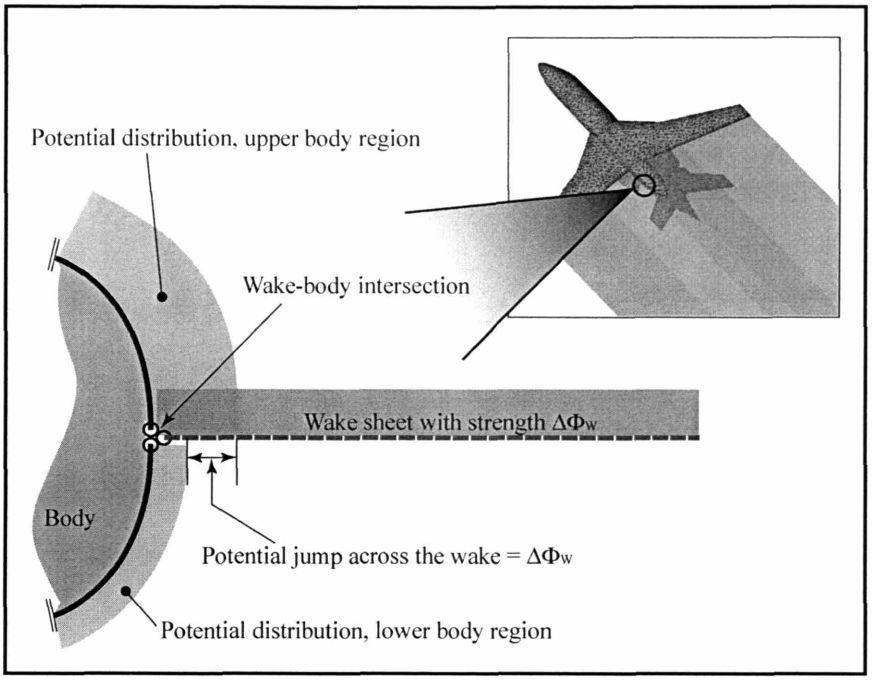

Figure 4-2: The effect of dipole wakes on the potential at a wake-body interface.

potential jump sheet wakes. Since the potential jump in the wakes is usually large, one must ensure that the dipole wakes align with the body discretization exactly. If the wake does not align with the body discretization, the edge of the wake sheet next to the body will act as a strong vortex. In turn, this will cause erroneous values of the potential along the body. For the wake piercing formulation presented in this thesis, the wakes are treated as equivalent vorticity distributions which produce a velocity influence. By examining the traditional dipole wake sheet implementation as analogous vorticity influences, one finds that there are three strong line vortices at all wake-body intersections (see figure 4-3). This set of strong vortices is not physical, rather it is a mathematical consequence of preserving the wake potential jump right up to the fuselage. The combined-body and wake line vortices are of equal magnitude, in the same positions, but of opposite signs, thus, in the velocity evaluation, they completely cancel each other (to preserve the physical reality of minimal vorticity at the wake-body intersection). The net velocity at wake-body intersections is therefore smooth.

The concept of the body piercing vortex wakes is a natural extension of using an equivalent vorticity wake to produce a velocity influence on the body, rather than a potential

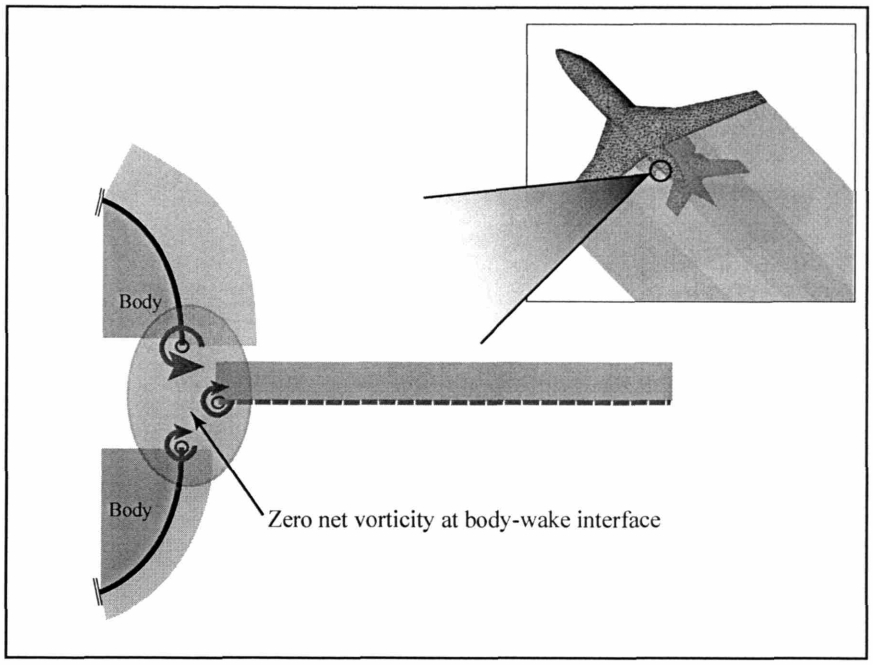

Figure 4-3: Representing the potential wake as vortices.

jump. Additionally, consider that the wake is merely a means by which the body bound vorticity (or equivalent circulation) is shed into the domain. The body bound vorticity can be mathematically represented in many diverse ways in a potential flow. As such, it is convenient to extend the vortex wakes into the body and represent the circulation of the body and wing using an embedded or body piercing vorticity distribution. By enforcing the influence of this body piercing wake as a velocity influence on the wing-body system, the potential jump in the solution for the body surface potential is not explicitly modeled, rather it is implicitly modeled via the velocity influence vorticity body piercing wakes. By accounting for all contributions to the total or overall potential, the potential jump at the wake-body intersection is re-introduced via the potential influence of the vorticity wake (which is equivalent to a dipole sheet). This body piercing wake formulation is illustrated in figure 4-4. Although the body piercing wake seems highly un-natural, the portion of the wake inside of the body is merely a means of representing the body bound vorticity. The body bound vorticity is required to produce the circulation around the lifting surface.

The body piercing wake formulation is implemented as follows:

1. Setup a solution to the wing-body component of the potential flow solution using any

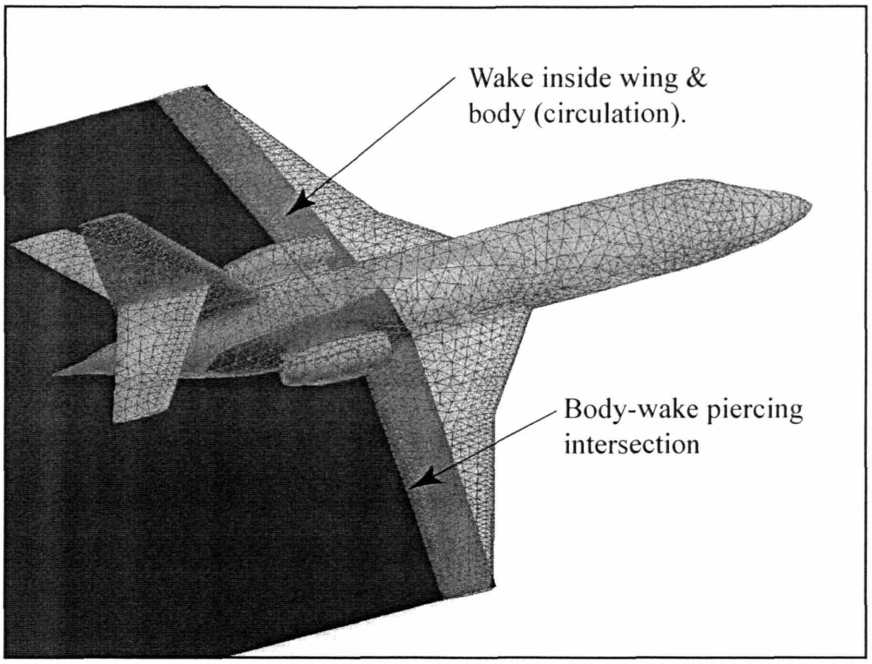

Figure 4-4: A demonstration of the body piercing wakes.

potential flow formulation.

2. Prescribe a wake which pierces the body. The wake should have a gradual variation of doublet strength from a value of zero at internal wake boundary points to the value prescribed by the Kutta condition at points where the wake pierces the boundary from interior to the exterior. For wings this piercing wake must intersect the wing at the trailing edge at which a Kutta condition will be applied.

3. Express the wake influence in terms of a contribution to the velocity boundary condition. Solve the system of equations, ensuring that the boundary conditions and trailing edge Kutta condition are satisfied. Be careful to recognize that the quantity being solved for has a different representation than it would if one were to consider a traditional panel method formulation (ie. if one is solving for the doublet strength, realize that the doublet strength no longer represents the perturbation potential, rather it represents the perturbation potential minus the wake potential!).

4. If the potential is desired, compute the potential influence due to the freestream, wakes and body and add them together.

Although, it is believed that the body piercing wake formulation is novel for three dimensional potential flow applications, initial proposals for body piercing wake concepts can be seen in some of the two dimensional panel method investigations by Hess, Pierce and Smith [13]. In two dimensions a single vortex point inside 2-Dimensional airfoils (represented using Neumann source panels) is used to provide the circulation necessary for lift generation. The idea was not pursued for long, since Hess, Pierce and Smith soon found that the vorticity panel Neumann approach was more convenient for their applications.

A brief example of body piercing wakes is presented to illuminate the application.

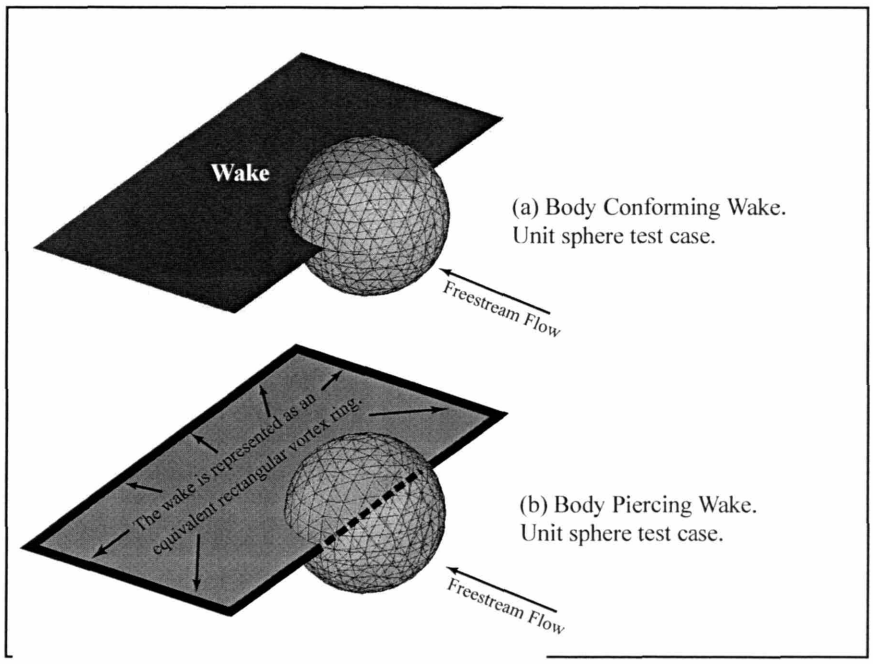

Figure 4-5: A schematic of the sphere example with (a) Body conforming wakes, and (b) body piercing wakes. The body conforming wake is represented using a potential jump inducing potential jump, while the body piercing wake is represented using an equivalent vortex ring (shown using thick lines).

A dipole sheet enclosing the trailing half hemisphere of a sphere: The example of a body piercing wake is the flow around a unit sphere centered at the origin. A trailing wake sheet of unit strength is prescribed. In the traditional formulation, the wake sheet is described using a dipole sheet of constant strength which conforms to the sphere as shown in figure 4-5a. In the body-piercing-wakes formulation, the wake is represented using a quadrilateral vortex ring which pierces into the sphere as shown in figure 4-5b. The

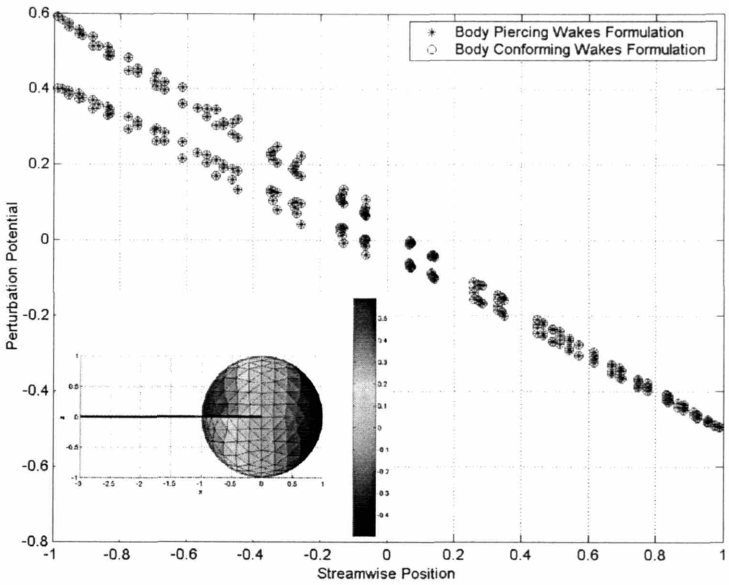

Figure 4-6: The total potential computed due to a body conforming wake, (o), and body piercing wake, (*).

resulting *total potential* for the two separate simulations is presented in figure 4-6. The total potential is the superposition of the body surface potential, and the potential due to the wake sheet.

4.1.1 Comments on Body-Piercing Wakes

For unsteady panel methods, a simple, and general approach to handle the wakes is a necessity. The body piercing wakes presented in this chapter have the potential to simplify panel methods greatly. Without the need for complicated wake-body intersection griding, it is possible to reduce user interaction times with panel methods by orders of magnitude. The body piercing wake concept can be applied to all non-membrane panel method formulations by appropriately incorporating the correct boundary conditions. Due to the conversion from a potential jump influence wake sheet to an equivalent velocity influcence, the discontinuities at wake-body intersections associated with the potential jump requirement are eliminated.

The body piercing wake formulation is effective for higher order distributions with

large panel counts. Although the method will work for low order, coarse discretizations, the effect of the internal wake will tend to reduce the accuracy of the solution (since the wake influence becomes a velocity boundary condition). The use of at least linear strength basis functions for the solution of body piercing wake problems is recommended.

4.2 The Vortex Particle Method

The vorticity in the wakes can be represented in a number of ways. In this thesis, a vortex particle method is investigated for the representation of the domain vorticity. Although a vortex particle method is chosen in this work, one could easily implement many other forms of vortex representation including sheet or filament vorticity.

The domain vorticity is represented using discrete vortex particles which capture the strength and magnitude of the vorticity. The overall domain vorticity is represented as the summation over all of the discrete vortex particles in the domain, which is written as[88]:

$$\vec{\omega}(\vec{R},t) = \sum_p \vec{\omega}_p(t) vol_p \delta(\vec{R} - \vec{R}_p(t)) = \sum_p \vec{\alpha_p}(t)\delta(\vec{R} - \vec{R}_p(t)),$$

where, $\vec{\omega}_p(t)vol_p$ is written as $\vec{\alpha}_p(t)$. Here, vol_p refers to the volume of the fluid domain which is represented by the vortex particle.

For a vortex particle representation of the vorticity, the discrete vector potential is:

$$\vec{\Psi}_p(\vec{R},t) = \frac{1}{4\pi}\sum_p \vec{\alpha}(\vec{R},t)\frac{1}{\|\vec{R} - \vec{R}_p(t)\|}.$$

The vorticity induced velocity is:

$$\nabla \times \vec{\Psi}_p(\vec{R},t) = \frac{1}{4\pi}\sum_p \nabla\frac{1}{\|\vec{R} - \vec{R}_p(t)\|} \times \vec{\alpha}(\vec{R},t). \tag{4.1}$$

Similarly, the gradient of the velocity term used for the vorticity stretching in the vorticity

evolution equation is:

$$\nabla\left(\nabla\times\vec{\Psi}(\vec{R})\right)=\frac{1}{4\pi}\sum_{p}\nabla\left(\nabla\frac{1}{\|\vec{R}-\vec{R}_{p}(t)\|}\times\vec{\alpha}(\vec{R},t)\right). \tag{4.2}$$

A Lagrangian reference frame is used for the evolution of the vorticity, such that the position $\vec{R}_p(t)$ of a discrete vortex particle at any given time is:

$$\frac{d}{dt}\vec{R}_{p}(t)=\vec{U}_{p}(\vec{R}(t),t). \tag{4.3}$$

The evolution of the vortex particle strength as it travels through the domain is:

$$\frac{D\vec{\alpha}_{p}(t)}{Dt}=\vec{\alpha}_{p}(t)\cdot\nabla\vec{U}_{p}(\vec{R}(t),t). \tag{4.4}$$

Each of the vortex particles, or vortons, has an associated core in order to mimic the physical vortex core as well as to reduce the numerical instability of the vortex interactions. A collection of vortex particle core expressions are presented in [88]. The evaluation of the vorticity induced vector potential can be represented as a matrix vector product:

$$[C]\,[\vec{\alpha}]=\vec{\Psi}_{p}$$

Here the vorticity is known and a single matrix vector product results in the vector potential. Additional information about vortex particle core functions and vortex methods in general can be found in [88].

Discrete Form of the Vorticity Evolution Equation

The evolution of vorticity is computed by discretizing the ODEs governing the vorticity evolution and computing the vortex particle position at time, $t+1$. A simple approach to this would be to use a forward Euler equation:

$$\vec{R}(t+1)=\vec{R}(t)+\vec{U}_{p}(\vec{R}(t),t)\Delta t \tag{4.5}$$

and then update the strength of the vortex as:

$$\vec{\alpha}_p(t+1) = \vec{\alpha}_p(t) + \vec{\alpha}_p(t) \cdot \nabla \vec{U}_p(\vec{R}(t), t)\Delta t. \tag{4.6}$$

4.3 Conclusions

In this chapter, methods for simplifying and automating wake modeling have been presented. The approaches presented in this chapter help minimize the user involvement in the solution of lifting body flows by:

1. Allowing CAD and CFD surface grids to be used for lifting body simulations. The development of body piercing wakes eliminates the task of prescribing wake-body intersections.

2. Using vortex particle methods to evolve the domain vorticity in time. The vortex particles are not constrained by connectivity requirements. This permits automatic, hands of wake evolution in complicated environments.

With the flexibility of vortex particle methods, coupled with the generality of body-piercing wakes, the lifting body problem is significantly simplified.

Chapter 5

Implementation Details

In this chapter the implementation details of the panel method formulations are described.

The boundary integral equation is discretized using a boundary element method [89, 127, 90], while the vortex volume integral equation is represented using a vortex particle method [59, 88, 57].

5.1 Boundary Element Method Implementation

The Galerkin Boundary Element Method is used to discretize the various potential flow formulations. Solution basis functions of linear order are considered for all examples shown. The Boundary integral equation is written in terms of a residual R:

$$(BIE - RHS) = R. \tag{5.1}$$

As an example, the Neumann-Source problem is written as:

$$\left[\sum_{j=1}^{N} \hat{n} \cdot \nabla \left(\frac{1}{4\pi} \int_{S_j} \sigma_j b_j \frac{1}{\|\vec{r} - \vec{r}'\|} dS'_j + \Phi_w \right) - \left(\hat{n} \cdot (\vec{V}_G + \vec{V}_{Gp} + \vec{\Omega} \times \vec{r}_{Gp} - \nabla \times \vec{\Psi}) \right) \right] = R_\sigma. \tag{5.2}$$

The weighted residual is minimized using a Galerkin formulation [127]. For each panel i on the discrete surface, a minimization of the residual is achieved by first multiplying by a

target basis function b_i and integrating the product over the panel:

$$\int b_i \left(BIE - RHS\right) dS_T = \int b_i R dS_T \tag{5.3}$$

for the example of the Neumann-Source formulation (for all target basis i):

$$\begin{aligned}\sum_j \int_{S_{T_i}} b_i \left[\hat{n} \cdot \nabla \left(\frac{1}{4\pi} \int_{S_j} \sigma_j b_j \frac{1}{\|\vec{r} - \vec{r}'\|} dS'_j + \Phi_w\right)\right] dS_{T_i} - \\ \int_{S_{T_i}} b_i \left[\left(\hat{n} \cdot (\vec{V}_G + \vec{V}_{Gp} + \vec{\Omega} \times \vec{r}_{Gp} - \nabla \times \vec{\Psi})\right)\right] dS_{T_i} \\ = \int_{S_{T_i}} b_i R_\sigma \, dS_{T_i}.\end{aligned} \tag{5.4}$$

In effect, this formulation minimizes the residual by ensuring it lies in a space orthogonal to the solution basis. In the panel method presented, the integration over the test basis functions is performed using numerical quadrature schemes[134, 135, 136]. In addition, the testing basis functions b_i are of identical form to those used for the solution representation b_j.

As a result of the discretization and formation of a residual minimization statement, the boundary integral equations become linear systems of equations which are readily solved using any number of techniques. Although the Galerkin formulation statement is robust, the computational effort is increased over the simpler collocation based approaches [127] due to the necessity of evaluating the integral over the target panel numerically. This outer integral evaluation results in an increase in complexity by a factor proportional to the number of quadrature points used in the integral evaluation.

5.2 Wake Implementation details

The vortex particle method wake representation was presented in chapter 4. Some additional details pertaining to the implementation of the wake model are presented in this section.

5.2.1 Kutta Condition Implementation

The addition of wakes involves adding new unknowns to the system. These unknowns can be determined by adding a Kutta condition to the linear system. The Kutta condition can be linear or non-linear. The linearized potential Kutta condition [123] is implemented by adding appropriate rows and columns to the the influence coefficients matrix. The nonlinear Kutta condition [137, 117, 142] is implemented using a fixed, approximate Jacobian in a damped Newton Method [139] solver. The use of Quasi-Newton methods such as the BFGS [140] algorithm will be investigated in future implementations. The advantage of a Quasi Newton method implementation is that an approximate Jacobian matrix is constructed with minimal time investment, thus reducing the cost involved in constructing the full Jacobian.

The linear system including a wake and Kutta condition can be written as:

$$\begin{bmatrix} [B2B] & [W2B] \\ [B2W] & [W2W] \end{bmatrix} \begin{Bmatrix} \{\hat{B}\} \\ \{\hat{W}\} \end{Bmatrix} = \begin{Bmatrix} \{B.C_{body}\} \\ \{T.E_{Kutta}\} \end{Bmatrix},$$

where, $B2B$ represents the body to body potential or velocity influence matrix, $W2B$ represents the wake to body potential or velocity influence, $B2W$ represents the body to wake influence at the Kutta condition forcing points, and $W2W$ represents the interaction between the wake and the Kutta condition points. For a simple linearized Source-Doublet formulation the linear system is:

$$\begin{bmatrix} [B2B_\mu] & [W2B_\mu] \\ [\Phi_U - \Phi_L] & [I] \end{bmatrix} \begin{Bmatrix} \{\hat{\mu}_{body}\} \\ \{\hat{\mu}_{wake}\} \end{Bmatrix} = \begin{Bmatrix} [B]\{\sigma_{body}\} \\ \{0\} \end{Bmatrix}.$$

This is a compact manner to write the linear system including the Kutta condition. For the non-linear Kutta condition, an iterative procedure is used to solve for the surface singularity strength:

1. For the current iteration wake strength, $\left\{\hat{W}_n\right\}$, solve the following intermediate linear system for the body singularity strength $\left\{\hat{B}_n\right\}$:

$$[B2B]\left\{\hat{B}_n\right\} + [W2B]\left\{\hat{W}_n\right\} = \{B.C_{body}\}. \tag{5.5}$$

Since, $\left\{\hat{W}_n\right\}$ is prescribed for the current step, the linear system to be solved is:

$$[B2B]\left\{\hat{B}_n\right\} = \{B.C_{body}\} - [W2B]\left\{\hat{W}_n\right\}. \tag{5.6}$$

2. Determine how well the Kutta condition is satisfied using the current wake strength, but the updated body surface singularity distribution:

$$[B2W]\left\{\hat{B}_n\right\} + [W2W]\left\{\hat{W}_n\right\} - \{T.E_{Kutta}\} = \{R\}. \tag{5.7}$$

3. If the residual R from equation 5.7 is less than some given tolerance, stop the iteration loop, else go to 4.

4. Update the wake strength based on the Kutta condition, and the current solution. For the non-linear pressure Kutta condition, this amounts to computing the change in potential based on the current trailing edge pressure jump:

$$\left[\frac{\partial(P_u - P_l)_i}{\hat{W}_j}\right]\left\{\Delta\hat{W}_n\right\} = \{\Delta(P_u - P_l)_n\}. \tag{5.8}$$

Solving this linear system, the resulting wake strength $\hat{W}$ is:

$$\hat{W}_{n+1} = \hat{W}_n + \Delta\hat{W}_n \tag{5.9}$$

5. Go to step 1. Repeat until converged.

The above weak iteration can be used for both linear and non-linear equations. For linear equations, the iteration will take a single step to converge, however, for non-linear Kutta conditions the approach may take several steps to converge, depending on how well the Jacobian matrix in equation 5.8 is represented.

5.2.2 Doublet Sheet, Vortex Sheet and Vortex Particle Wakes

Consider a discrete dipole sheet representing a wing trailing wake. The discrete doublet wake can be equivalently represented using equivalent vortex sheets and vortex rings. For piecewise continuous doublet representations, the equivalent vortex ring surrounding the doublet panels is nullified by the neighboring panels. As such, the use of higher order, piecewise continuous doublet wake panels is preferred. In order to convert the dipole panels to equivalent vortex particles the following steps are taken (see figure 5-1):

1. Determine the equivalent vortex representation for each dipole sheet to be converted to vortex particles. The equivalent vortex sheet is computed by examining the tangential derivative of the potential distribution.

2. Determine the number of vortex particles to be emitted from each panel.

3. Divide the panel into equal area segments and generate a vortex particle at the centroid of each of the segments.

   (a) The particle strengths are computed by multiplying the area represented by the panel segment by the strength of the vortex panel.

   (b) The vortex particle radius is determined using the maximum radius of the panel segment and adjust it by a user specified factor.

5.2.3 The Farfield Approximation Model

Two levels of farfield approximation exist:

1. *Fixed in space particles*: When vortex particles travel sufficiently far away from the bodies in the domain their exact position becomes less important. As such, once the vortex particles have reached a sufficient distance from the body, they can be frozen in space. This effectively reduces the inter-particle computations since no induced velocities are required for the farfield-fixed-in-space vortex particles. The vortex particles which are fixed in space do however continue to move with the freestream velocity relative to the body in question.

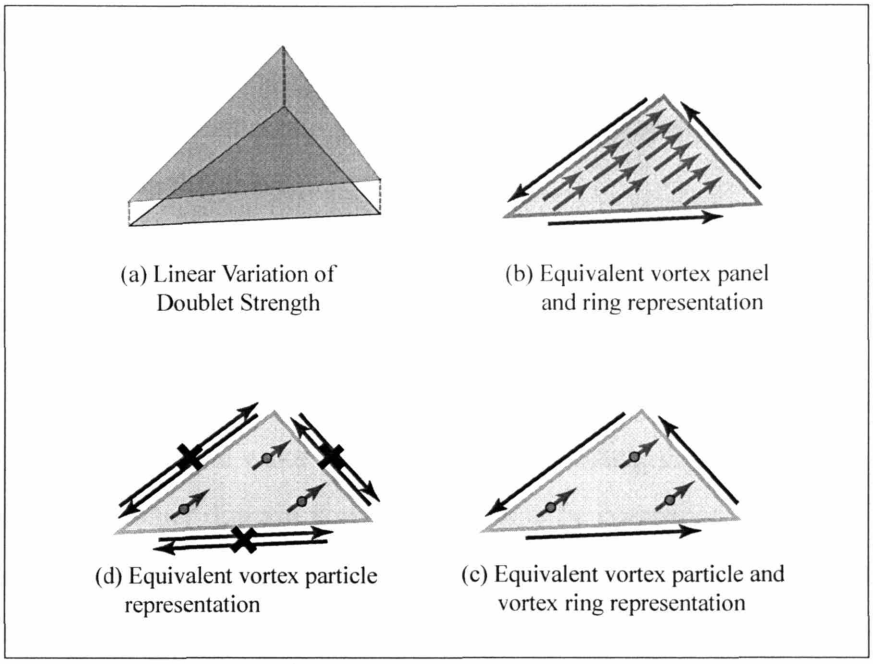

Figure 5-1: A schematic illustrating the conversion of dipole sheet panels to vortex particles. In (a) the linear variation dipole distribution is shown for a particular wake panel. In (b) and equivalent vortex representation is illustrated. Notice, there are strong vortices around the circumference of the panel, and there is a constant strength vorticity distribution on the panel. In (c) the constant strength vorticity distribution on the panel is converted into a series of vortons or vortex particles. Finally, in (d) the cancellation of the circumferential panel vortices with the circumferential vortices of neighboring panels is illustrated. This cancellation occurs due to the piecewise continuous linear basis representation of the doublet strength. If the representation were not continuous, the circumferential vortices would not cancel with their local neighbors.

2. *Multipole Expansion Lumping* Once particles reach extreme distances from the body, their influence can be treated as a lump sum influence. The vortex particles are lumped into multipole expansions and each multipole expansion is treated as a simple multipole particle. These multipole representations have no inter-particle influence in the farfield; however, they do have influence on the near field vortices and the body. Since these multipole representations have no inter-particle influence, they simply convect with the freestream flow. This farfield simplification is made in order to reduce the number of particles in the domain in order to maintain a fast simulation.

The farfield models are used to reduce computational complexity.

5.3 Putting it all together

The following section describes the solution approach implemented in the panel method framework presented in this thesis.

5.3.1 Summary of Solution Steps

In order to simulate a body shedding wakes, it is necessary to compute velocities and use those velocities to advect the wake. In addition to convecting the wake, the velocities due to the wake and any other domain vorticity must also be computed as an influence on the body boundary condition. In the current implementation this is accomplished by using a time stepping procedure. The following general steps occur during each time step in the solution process regardless of the potential flow formulation being used:

Step 1) If the simulation is a morphing body simulation, load the current geometry definition. Solve the potential flow boundary integral equation, to determine the unknown singularity strengths on the surface of the body. Also determine the unknown potential jump in the new wake region for the current timestep. Any of the potential flow formulations from chapter 2 can be used for determining the potential flow solution. The velocity boundary condition should be computed based on the current body translational and rotational velocities, as well as any morphing of the body surface. The current domain vorticity influence, $\vec{U}_{\Psi}$, is also included in the boundary conditions. Included in this flow solution is the determination of the potential jump across unknown buffer wake, which enforces the potential Kutta condition.

Step 2) Determine the strength of the vorticity that needs to be released into to domain. This new vorticity is the converted vorticity from the previous timestep known buffer wake layer.

Step 3) Determine the velocity and gradient of the velocity influence from the body onto the vortex particles in the wake using the boundary integral equations. This involves eval-

uating the gradient of the potential flow integral equation at each of the vortex particle positions. This is a single matrix vector product.

Step 4) Determine the velocity and gradient of the velocity influence of each of the wake particles on each of the other wake particles using the integral equation for the vorticity-velocity relationship. This is a matrix vector product.

Step 4 a) If necessary, compute the pressures and forces acting on the body, prior to updating the position and strength of the wake. This is an application of the unsteady Bernoulli equation, to determine the pressure from the velocity.

Step 5) For each vortex particle in the wake, update the particle position and vortex particle strength using the Lagrangian vortex evolution equations. If the vortex particles are in the farfield region, simply advect the particles with the local freestream velocity relative to the body. For the nearfield particles, this step involves determining the new position and strength by solving the ODEs governing the evolution of the vorticity.

Step 6) Compute the wake to body influence based on the new wake voterx particle positions and strengths. This is done by evaluating the matrix vector product represented by the Poisson equation governing the vorticity-velocity relationship.

Step 7) Start over at (1) unless the iteration stopping condition has been reached.

5.4 Acceleration Algorithms

Two matrix vector product(MVP) acceleration techniques are implemented for the solution of the potential flow. The precorrected-FFT [84] is used for accelerating the GMRES [100] iterative potential flow solution, while the Fast Multipole Tree approach is used for evaluating the vorticity stretching and velocity influences. Following the introduction of the acceleration methods a brief discussion of the use of the methods is presented. Although

the acceleration methods are briefly outlined in the following two sections, more detailed information can be found in the original literature [110, 109, 70, 86].

5.4.1 precorrected-FFT

The precorrected-FFT method used is based on the original p-FFT algorithm [84]. Through a collaborative effort, a generic version of the pFFT algorithm was implemented[47]. In the pFFT algorithm, the matrix vector product:

$$[A]\vec{\sigma} = \vec{\phi} \tag{5.10}$$

is accelerated using the following steps:

1. **Projection**: Through a polynomial interpolation procedure the charge distribution σ is projected onto a 3-Dimensional Fast Fourier Transform Grid. In order to make the process generic, the projection operator takes the moments and centers of discrete charge representation and projects those moments onto the FFT grid. By taking moments and centers, the use of arbitrary charge sources is possible. The process is summarized as:

   $$[P]\vec{\sigma} = \vec{\sigma_g} \tag{5.11}$$

   where, P is the projection matrix and σ_g is the FFT grid equivalent charge. The projection operator is setup once per given geometry per FFT grid.

2. FFT, **Convolution,** FFT^{-1}: An FFT is performed on the equivalent grid source charges. Also, an FFT is performed on the kernel evaluated on the grid. The FFT is performed using the FFTw code[48]. Once in Fourier space, a multiplication of the transformed charge and transformed kernel is performed (the original physical space operation was a convolution). Finally, an inverse FFT is applied to the result of the multiplication to give the grid potentials, ϕ_g.

   $$[H]\vec{\sigma_g} = \vec{\phi_g} \tag{5.12}$$

3. **Interpolation**: The grid charges are interpolated back onto the evaluation points through a polynomial interpolation. The interpolation is achieved using the same operator as in the projection with different moments and centers possible (if the testing basis functions are different or the inner/outer operators are different). The interpolation matrix is determined by taking the transpose of the result (in reality a transpose multiply operation is performed to reduce the number of memory accesses):

$$[I]\vec{\phi_g} = \vec{\phi} \tag{5.13}$$

4. **Precorrection**: Finally, the approximation of the nearfield interactions are subtracted and replaced by directly computed interactions (using an appropriate integration scheme).

$$\left([D] - [\tilde{I}][\tilde{H}][\tilde{P}]\right)\sigma = PC \tag{5.14}$$

The end result is a matrix vector product which is represented as:

$$[I][H][P] + \left([D] - [\tilde{I}][\tilde{H}][\tilde{P}]\right)\sigma = \phi \tag{5.15}$$

The matrices $[I]$,$[P]$ and $[D]$ as well as the Kernel transform a need only be computed once per given fixed geometry. The matrix vector product is rapidly computed during the iterative solution process by multiplying the stored matrices. The generic framework which was developed enabled the separation of the operators.

5.4.2 Fast Multipole Tree Method

The fast multipole tree method [110, 70] is implemented for accelerating the evaluation of the vorticity stretching and velocity influences. The method uses a multipole expansions but does not go into the complexity of using local expansions [46]. The following steps highlight the FMT algorithm which is implemented:

1. **Octree Domain Decomposition**: The following steps are used to setup the octree and multipole representation:

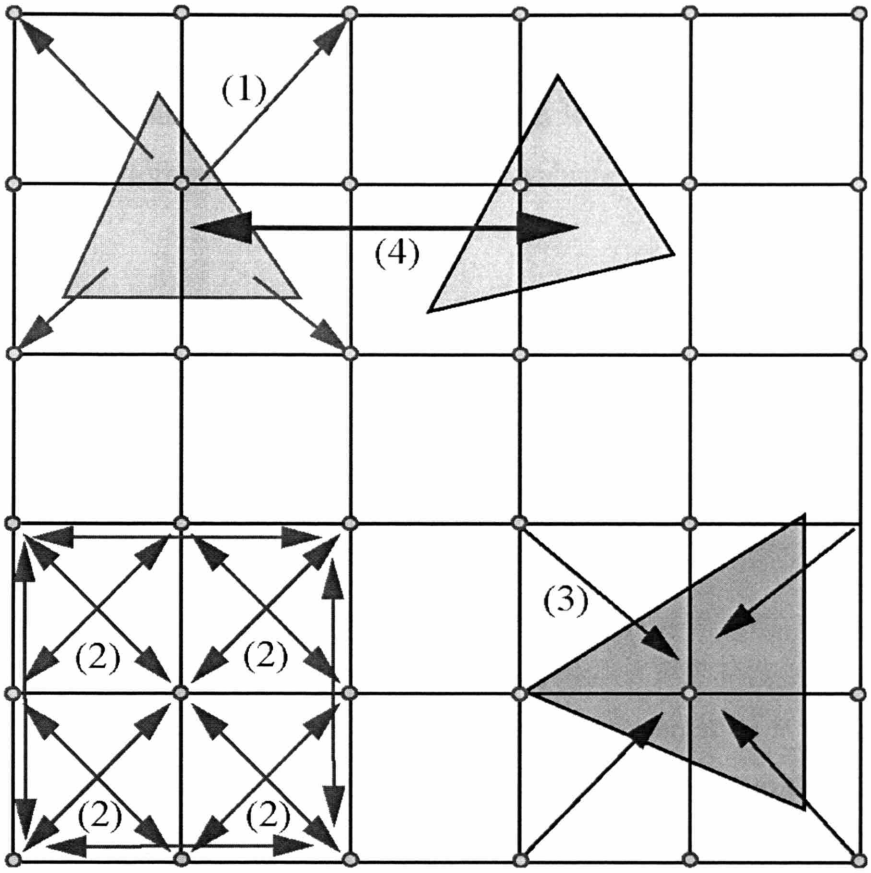

Figure 5-2: The pFFT algorithm presented graphically. First a uniform 3D-FFT grid is generated. The domain charges are projected onto the grid. Following that the convolution is performed in Fourier space to yield the grid potential. Following that the grid potentials are interpolated back to the evaluation points, and lastly the nearby interactions computed directly and subtracted from the grid based computation.

(a) Create a root cell enclosing the entire geometry under consideration

(b) Get $NumElements$, the number of elements in the *current cell*

(c) If $NumElements > MaxNumElements$ *then* split *current cell* into 8-children cells and cycle over each of the 8-children cells by going to step b.

(d) If $NumElements < MaxNumElements$ *then* construct leaf cell multipole representation by clustering elements in current cell into a multipole moment expansion at the centroid of the *current cell*. Go to b. and continue decomposition with the next cell in the list.

(e) Translate and add the *current cell* multipole expansion to the parent cell multipole expansion. The parent cell is the one level higher cell to which the current

child cell is associated.

2. **Potential Evaluation**: The potential evaluation is the second step in the multipole process. The following steps are taken to evaluate the potential at a point $\vec{R} = (x, y, z)$:

   (a) Start at the root cell level:

   (b) Evaluate the distance, R_{pr} between the cell centroid and the evaluation point. Compare this with the cell sidelength S. Compare the separation to sidelength ratio with a user specified minimum:

$$K = R_{pr}/S \tag{5.16}$$

   (c) If $K < K_{user}$: The current cell multipole representation is too close to the evaluation point. If the current cell is not a leaf cell, go to the children cells of the current cell, cycling through each starting at step (b). Nested loops can continue multiple levels until each interaction is accounted for. If the current cell is a leaf cell, directly evaluate the interactions between the elements in the current cell and the evaluation point.

   (d) If $K > K_{user}$: Compute the potential due to the current cell to the evaluation point:

      i. If the current cell is a leaf cell, the potential is computed by cycling through the elements in the cell.

      ii. If the current cell is not a leaf cell, compute the potential at the evaluation point using the multipole expansion expressions in the cell.

In the current implementation of the Fast Multipole Tree approach, a heirarchical distance specification is used. One specifies a center of the domain and one can specify multipole tree evaluation properties in different zones of the domain defined using increasingly larger spherical zones. For example, near the body, one might wish to ensure that the majority of interactions are directly computed, while far from the body, the more frequent use of

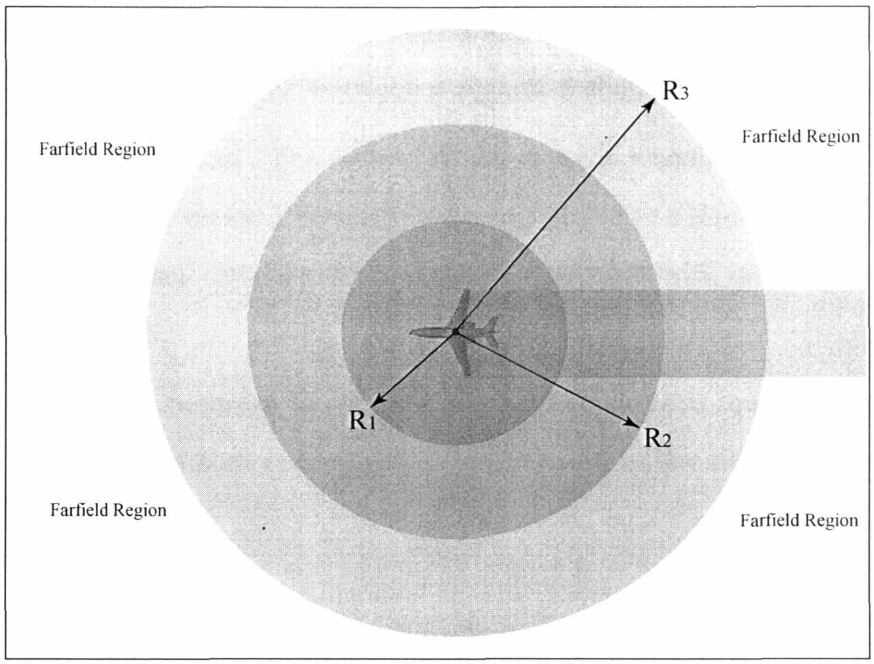

Figure 5-3: The domain is divided into several concentric spherical domains. In each domain, the minimum separation distance between evaluation point and cell center can be specified. This allows for high resolution of the interactions in certain regions of the domain, while other regions can have a more approximate, more rapidly computed interaction.

multipole expansions can be considered. This is shown in figure 5-3 The various controls on the Fast Multipole Tree acceleration in the current code are as follows:

1. **Octree Decomposition Setup Controls**

   (a) Buffer for the bounding box. The bounding box can be enlarged by a small amount to encompass additional space if necessary.

   (b) Multipole Order. Second order is maximum expansion order.

   (c) Maximum number of elements per octree cell. The number of elements per cell enables the octree decomposition. It has been found through trial and error that 10-20 elements are the best compromise between accuracy and computation time.

2. **Evaluation Controls**

   (a) Minimum cell separation for farfield multipole approximation. This is based on the ratio of cell-sidelength to the distance between the cell-centroid and

element-centroid. Typically, separation distances of 2.5 cell sidelengths are a good compromise between accuracy and evaluation time.

(b) The farfield radius. The farfield radius dictates where the motion of particles is based only on the freestream velocity relative to a fixed in space body. The magnitude and direction of the vorticity associated with each of the particles is not adjusted.

(c) Nearfield Subdomian Radii. The nearfield subdomain radii are used to determine the minimum cell separation value based on the distance away from the body.

5.4.3 A Brief Discussion of the Acceleration Routines

The pFFT and FMT approaches have different strengths for the problem under consideration. For this reason, both of the approaches are used for their appropriate application. The pFFT is used for computing the matrix vector product inside of the GMRES iterative solution method, while the FMT is used to compute the matrix vector products for one off computations (such as the velocity and stretching computations). This is discussed briefly here.

1. The pFFT is used for the solution routines, since, once the matrices are set up for a given geometry the matrix vector product is extremely efficient. Since the Fast Multipole Tree method which is implemented only considers an upwards sweep of the Octree structure (no local expansions), the matrix vector product is less efficient.

2. The pFFT is not used for the wake interactions, since the wake may extend a long way behind the body. In order to accurately approximate the wake, a large equi-spaced grid must be used. The FMT is more appropriate due to the hierarchical nature of the octree grid. This permits rapid evaluation of the influence.

3. The pFFT is not used for the wake particle to particle interactions due to the expense of precorrection. The precorrection cost becomes significant component of the setup time when the direct computations are simple point to point interactions.

4. The FMT is used for computing the majority of the velocity influences, since the pFFT would typically require a larger direct interaction stencil and/or a larger projection and interpolation stencil and order. This increases the direct and precorrection components of the matrix vector product setup significantly. Since the FMT can be tuned, it is ideal for computing the velocity and stretching influences.

5.5 Implementation Details of the BIE Formulations

In this section a brief discussion of the three boundary integral equation formulations which were presented in Chapter 2 are discussed. The application of these formulations for solving the body surface singularity distributions is examined more closely in the following chapter; however, for completeness they are presented here.

1. **Source-Doublet Formulation with Potential Doublet Buffer Wakes:** The source-doublet formulation used for solving the potential flow involves the use of sources and doublets on the surface of the body, with a dipole buffer wake sheet used for satisfying the linear Kutta condition. The no flux boundary condition is satisfied through the use of the source distribution. In addition to the body motion and morphing velocities, the vortex particle wake velocity is also used as a boundary condition on the potential solution. The time stepping procedure is similar to that presented earlier.

2. **Doublet Lattice Neumann Formulation with Velocity Inducing Doublet Buffer Wakes:** The doublet lattice formulation is similar to a traditional doublet lattice solver except for the linear order doublet strengths and the use of vortex particles in the wake rather than a traditional wake sheet. The Kutta condition is the simple linearized no trailing edge vorticity Kutta condition.

3. **Source Neumann Formulation with Body Piercing Doublet Wakes:** The implementation of the source Neumann formulation with body piercing wakes is presented in a little greater detail that the previous two formulations. The surface singularity in

this formulation is a source distribution of piecewise linear strength. The source distribution is treated as a velocity influence. The wakes are represented using doublet sheets which pierce the body at the trailing edge. For a single, simple wing, Figure 5-4 illustrates the piercing doublet wake. The doublet wake sheet is treated as a velocity influence. The combined velocity influence must satisfy the surface boundary condition (which is used to determine the source strengths) and the Kutta condition (which is used to determine the doublet strengths). The non-linear Pressure Kutta condition described earlier is implemented.

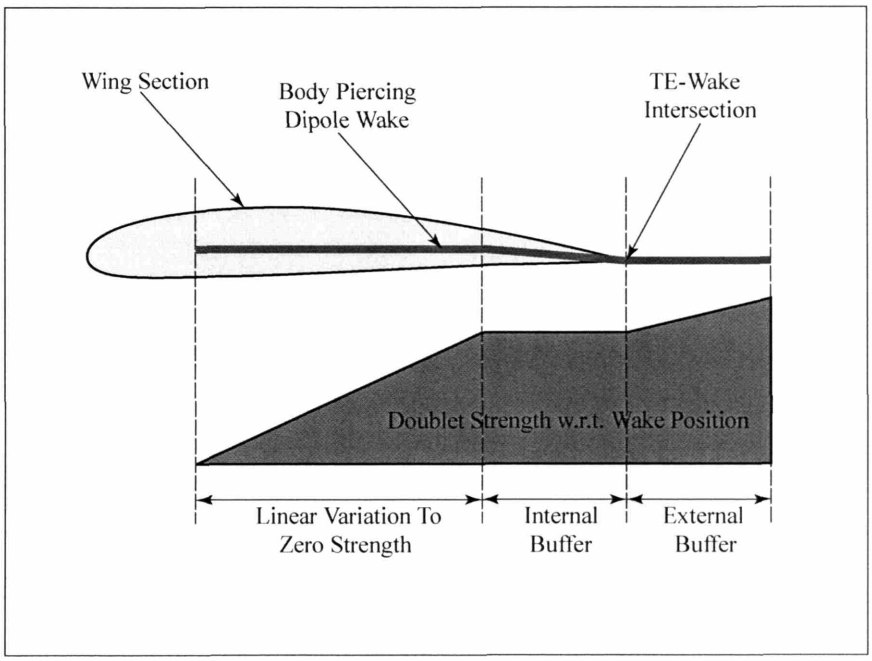

Figure 5-4: A schematic illustrating the body piercing wakes demonstrates the linear variation of the internal to the body wakes. For effective computations, it has been found that a linear distribution of doublet strength inside of the body results in sufficiently smooth source distributions on the surface of the body. For efficiency the source-Neumann formulation is the approach considered in this work (note: the body piercing wake concept can also be used for source-doublet type approaches).

5.6 Conclusions

The various implementation details for the potential flow solution framework have been presented in this chapter. In the chapter which follows simulation results and examples are

presented for the various potential flow formulations investigated.

Chapter 6

Simulations and Results

This chapter demonstrates the solution of a selection of relevant sample potential flows using the formulations presented in this thesis.

6.1 Validation Computational Experiments

6.1.1 NACA-0012 Non-Lifting Wing

A rectangular wing with a symmetric NACA 0012 airfoil at zero degrees angle of incidence is examined in this section. The discretized wing comprises 4096 triangular panels and 2145 vertices. The wing is a lattice of ordered right angle triangles (32 panel widths in the spanwise direction by 64 panel widths in the chordwise direction) with leading edge refinement. Although an analytical solution is not known, the NACA 0012 airfoil is a common test case and as such, the comparison to computational data from the 2-D panel method XFOIL [38] is made. The surface pressure distribution for the source-Neumann formulation and the Source-Doublet Potential formulation is illustrated in figure 6-1. Since the flow is at a zero incidence angle, the wake sheet strength is identically zero.

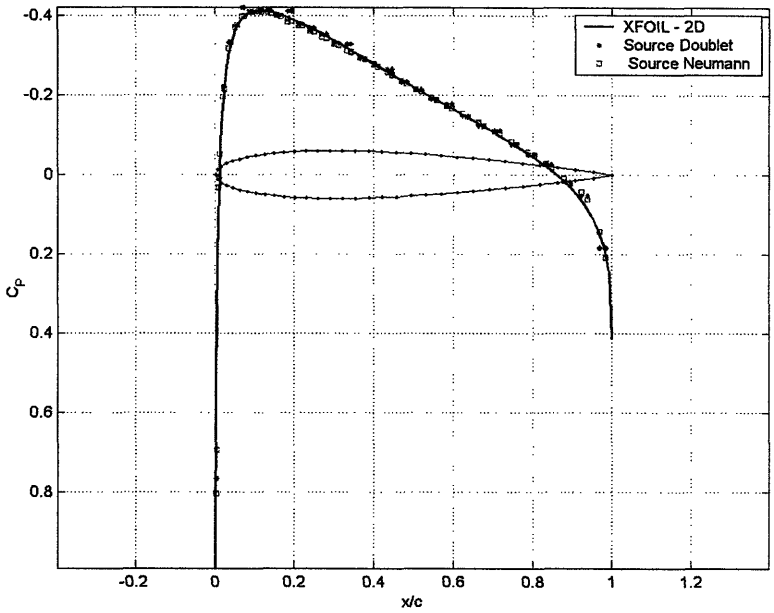

Figure 6-1: The results are illustrated for both the Neumann-Source approach and the Source-Doublet approach. Comparison is made to the 2-D results from the panel method code XFOIL [38] and show a good match.

6.2 Steady NACA 0012 Lifting Wing Simulations

In order to determine the steady state solution to a given lifting problem, there are two options. First, the solution of a potential flow problem with a very long trailing wake. This solution is determined in one step and does not require iteration in time. The second approach is more costly yet more accurate. It involves solving for the steady state conditions by iterating some startup flow up to steady state. The second option, though more costly is chosen for this example. The lifting body wing centerline pressure distribution is presented in figures 6-2 and 6-3. Figure 6-2 illustrates the pressure distribution around the midsection of a NACA 0012 with Aspect Ratio of 4. Since bodies of thickness are presented, only the source-doublet and source Neumann-formulations are considered. The results demonstrate good agreement with each other, as well as a good agreement with a reduced angle of attack 2-D simulation. In addition to the thick body simulation results, a plot of the wing centerline pressure difference due to a flat plate with an aspect ratio 4 wing is presented in 6-3. The result demonstrates the large leading edge contribution to the pressure due to the

strong leading edge vorticity in this case.

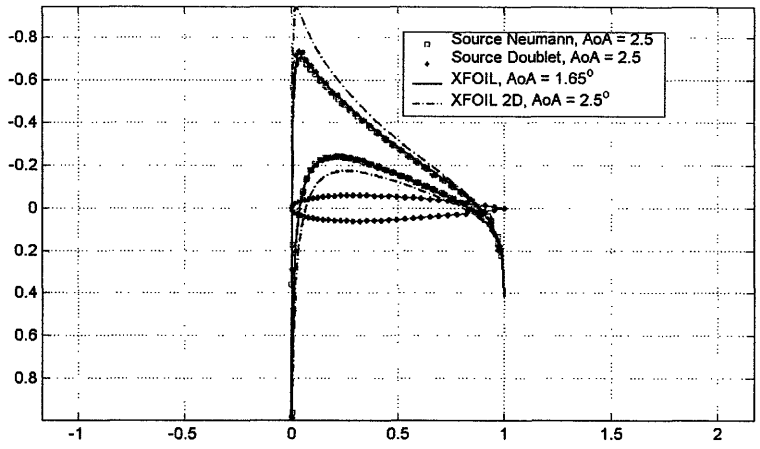

Figure 6-2: The pressure distribution around the midsection of an Aspect Ratio 12 finite wing with NACA 0012 profile at a zero angle of attack

6.3 Unsteady Computations

In this section results for wings under unsteady motions are examined.

6.3.1 Unsteady Startup Flow

The simulation of an unsteady startup flow is presented in this section. The wing in this example is subject to a unit step velocity increase, such that the acceleration of the wing at time $t = 0$ is an impulse function. As a result of the sudden start up, several interesting flow features can be seen. First, an infinite force will act on the body due to the sudden acceleration of the body (in the discrete simulations, this force is large, not infinite). A starting vortex is formed due to the satisfaction of the Kutta condition at the initial startup. As the distance between the starting vortex and wing increases, the effect of the downwash

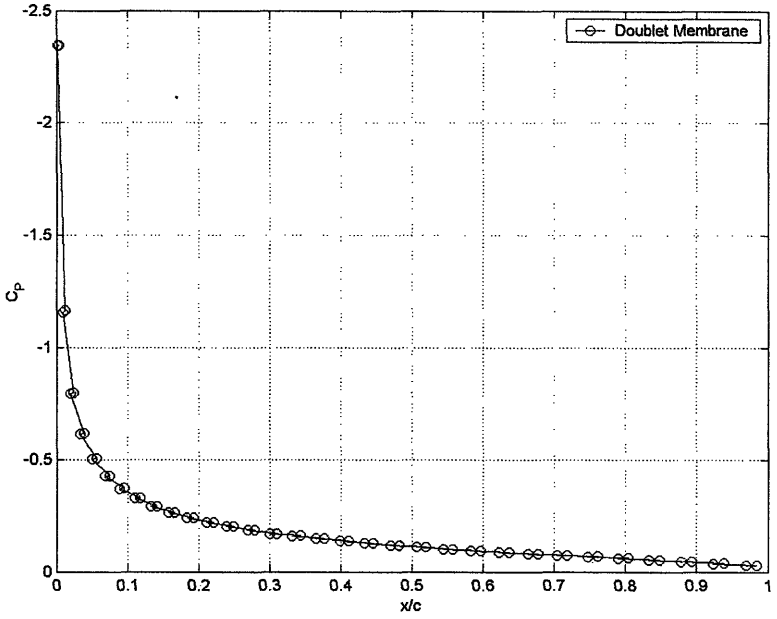

Figure 6-3: The pressure distribution at the midspan of a Aspect Ratio 12 membrane wing.

from the starting vortex is reduced. As a result the lift will gradually rise and after a long time, settle at a steady state value. Finally, since the wing is three-dimensional, one can readily see the wing tip vortices and the wing tip vortex roll-up. The startup flow was examined for three different aspect ratio wings (Aspect Ratio 4, Aspect Ratio 8, and Aspect Ratio 12), each with a NACA 0012 profile, except for the membrane which is an infinitely thin plate with no camber. The non-membrane wings are discretized using 4096 triangular panels and 2145 vertices, while the membrane wing is discretized using 2048 panels and 1089 vertices. In these simulations, there is significant wing leading edge refinement in order to accurately capture the large gradients of singularity strength at the leading edge.

Figure 6-4 shows the time evolution of the Z-component of the resultant force for the wing at an incidence angle of 2.5 degrees. The results are compared with data extracted from a vortex lattice startup flow computation presented in Katz and Plotkin [113]. Figure 6-5 shows the resulting vortex particle trail behind the wing. The unsteady startup flow demonstrates that the methods developed in the solution framework accurately model time dependent flows. The unsteady lift increase with time compares well with the results presented in [113]. The only noticeable difference between the results is the early transient

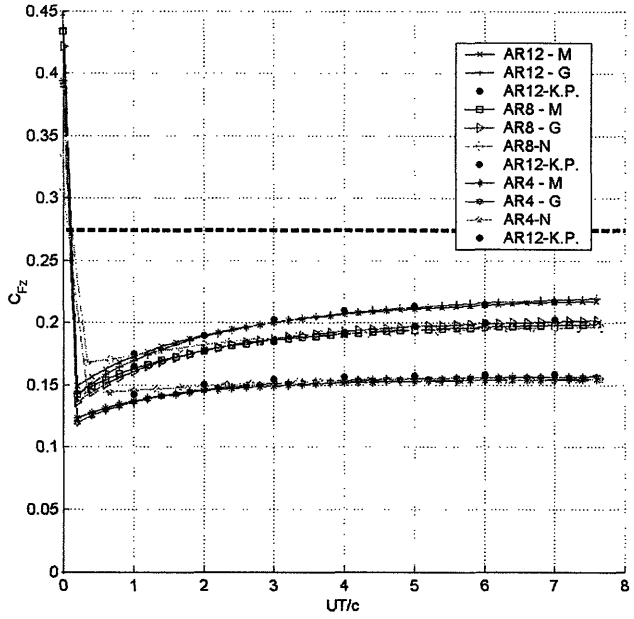

Figure 6-4: The figure illustrates the time development of the Z-Component coefficient after a sudden step function velocity change. The wing is instantaneously set to 2.5 degrees angle of attack at time t=0. The results are plotted for an aspect ratio of 4,8, and 12. In addition results are plotted for the membrane solution approach (M), the source doublet approach (G), and the Source-Neumann approach (N). The plot also illustrates the results presented in Katz and Plotkin [113].

time response of the Neumann-Body-Piercing Wake formulation result. These deviations between the Neumann Source formulation code and the other formulations are attributed to the satisfaction of a nonlinear pressure Kutta condition rather than a linear Kutta condition.

6.3.2 Unsteady Finite Aspect Ratio Heaving Wing

The unsteady heaving wing problem provides an opportunity to validate the unsteady time dependent flow solution capabilities of the panel methods examined. The heaving wing demonstrates the ability to compute unsteady flows in which wake-body interactions play an important role in the overall production of forces. The heaving wing simulations are compared to analytical expressions for an oscillating 2-Dimensional plate which are presented by Theodorsen [104] and Katz and Plotkin [113].

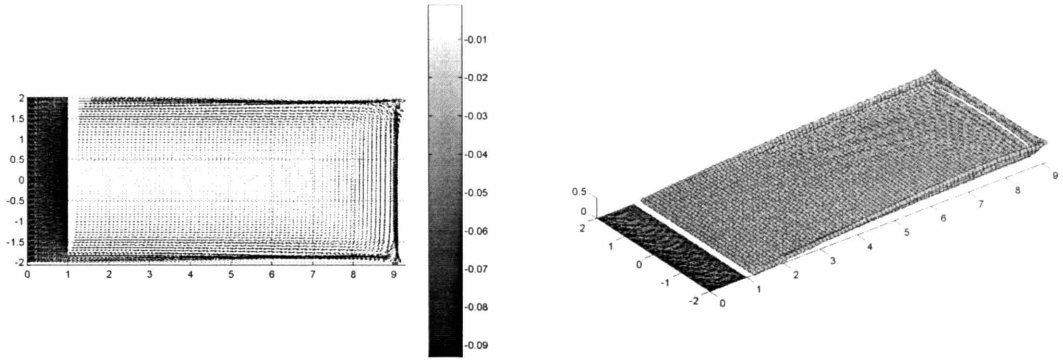

(a) The vortex particle representation of the vorticity behind an aspect ratio 8 wing after a sudden startup. The figure illustrates the vorticity distribution in the wake. As expected, there is a strong concentration of vorticity trailing the wingtips, which eventually forms two vortices. In addition, the figure clearly illustrates the startup vortex, as well as the gradual increase in vorticity due to the sudden startup of the wing.

(b) The vortex particles trailing an aspect ratio 8 wing after a sudden unit step velocity startup. The figure clearly demonstrates the startup vortex roll up as well as the commencement of the wing tip vortex roll up.

Figure 6-5: The startup flow around an aspect ratio 8 wing.

Theodorsen Theory For 2-Dimensional Flat Plate Heaving Motions [104]

In the Theodorsen theory, oscillations are assumed to have a small amplitude. The Z-Component of force produced during heaving oscillations of a 2-Dimensional flat plate is expressed as [104]:

$$F_Z = -\pi\rho c\left(UC(k)\frac{dh}{dt} + \frac{c}{4}\frac{d^2h}{dt^2}\right), \tag{6.1}$$

The first part of equation 6.1 represents the generation of traditional steady state lift multiplied by a lift reduction factor $C(k)$, while the second part of the equation represents the unsteady acceleration component of the lift. The lift reduction factor $C(k)$ can be written as a function of the reduced frequency k as[104]:

$$C(k) = F(k) + iG(k). \tag{6.2}$$

The expression for the real component, $F(k)$ is:

$$F(k) = \frac{J_1(k)(J_1(k) + Y_0(k)) + Y_1(k)(Y_1(k) - J_0(k))}{(J_1(k) + Y_0)^2 + (Y_1 - J_0(k))^2}, \tag{6.3}$$

while, the expression for $G(k)$ is:

$$G(k) = -\frac{Y_1(k)Y_0(k) + J_1(k)J_0(k)}{(J_1(k) + Y_0)^2 + (Y_1 - J_0(k))^2}. \tag{6.4}$$

A plot of the circulatory lift reduction factor and phase shift due to Theodorsen's lift deficiency factor is presented in figure 6-6. The reduced frequency k is defined as:

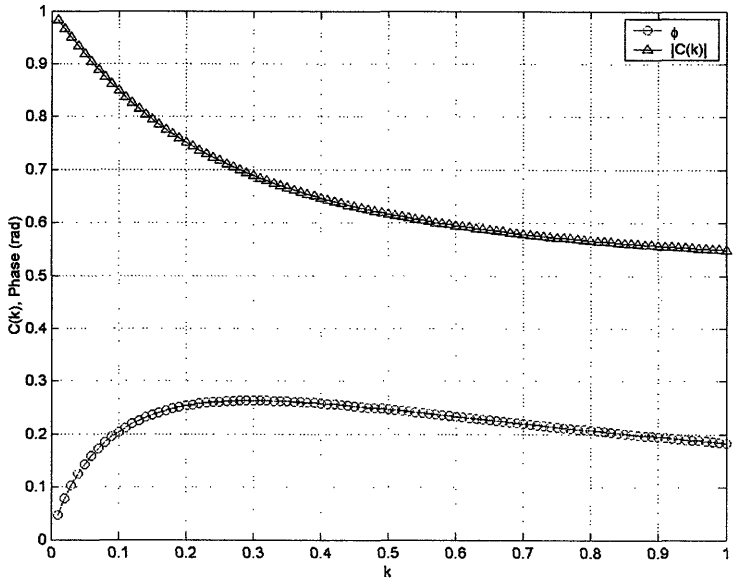

Figure 6-6: The Theodorsen lift deficiency function as a function of the reduced frequency. The function is presented in terms of the magnitude ($C(k)$) and the phase shift in $radians$.

$$k = \frac{\omega c}{2U}. \tag{6.5}$$

The Theodorsen lift deficiency factor $C(k)$ is a direct result of the downwash on the main wing produced by the unsteady wake development. The unsteady release of vorticity causes a reduction in the circulatory lift while also causing a lag in the development of the lift.

Katz-Plotkin Theory [113]

Katz-Plotkin derived the following similar expression; however, considered different assumptions [113]:

$$L = -\pi\rho c\left(U\frac{dh}{dt} + \frac{3c}{4}\frac{d^2h}{dt^2}\right). \tag{6.6}$$

To arrive at equation 6.6, Katz and Plotkin [113] neglected the effect of the wake downwash on the flat plate. Although this simplifies the derivation, this results in significant deviations from the Theodorsen [104] result and the computational results.

Simulations of Heaving Wings

Simulations are performed for several different frequencies. Each simulation has a heaving velocity defined by:

$$\frac{dh(t)}{dt} = -0.05sin(\omega t). \tag{6.7}$$

The computational results are presented and compared with the Theodorsen Theory [104] and the Katz and Plotkin theory [113] in figures 6-7 - 6-9. The results for the heave oscillations compare more favorably with the theory presented by Theodorsen [104] than Katz and Plotkin [113] as would be expected. This is due to the panel method accurately representing the unsteady vorticity in the wake. As the heave oscillations increase in frequency, the importance of more accurately capturing the wake downwash effect on the heaving wing is apparent.

The computational results demonstrate slight differences when compared to the theoretical predictions. There are several reasons for this:

1. The computational results consider a finite aspect ratio wing. As such, the computational results expectedly demonstrate a slightly lower Z-force prediction due to the 3-Dimensional nature of the flow. This effect is clearly captured in the lower frequency oscillations where tip vortices play a significant role in Z-force reduction.

2. The computational results consider several different Kutta conditions, whereas, the Theodorsen theory [104] considers a finite-trailing-edge-velocity Kutta condition. As such, the computational results would be expected to differ from the theoretical

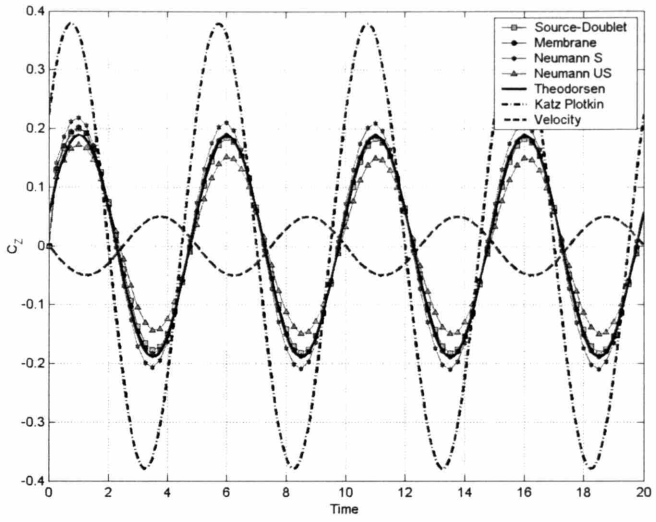

Figure 6-7: The plot illustrates the z-Component Coefficient of Force resulting from heaving oscillations at a reduced frequency of $\frac{\pi}{5}$. Notice, at this higher reduced frequency, the unsteady component of the Forces begins to have an effect on the overall forces. This can be seen from the phase shift which appears between the velocity and the resulting lift. Computational results are presented for the source-doublet, the doublet Neumann membrane lattice, the source-Neumann wake piercing formulation with body piercing wakes (for both a steady and unsteady pressure Kutta condition). Comparison is made to theories presented by Theodorsen [104] and Katz and Plotkin [113].

predictions, especially at higher frequencies. For example, in figure 6-7 results have been presented for steady and unsteady, linear and non-linear Kutta conditions. It can be seen that differences exist between the various simulations. The most notable differences occur when the Kutta condition considered differs from the one considered by Theodorsen.

The simulation results for the heave oscillations demonstrate the versatility and ease of use of the combined panel method-vortex particle method approach. In figures 6-10 vorticity wake structure plots are presented for both fast and slow heave oscillations. The plots illustrate both the vorticity structure as well as the vorticity evolution with time.

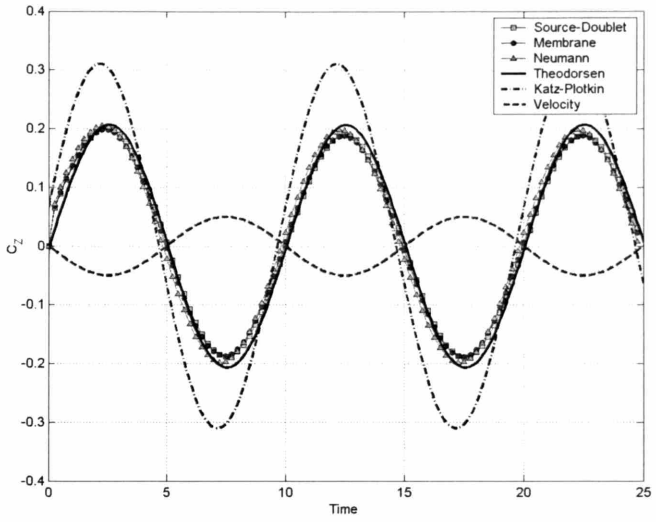

Figure 6-8: The plot illustrates the z-Component Coefficient of Force resulting from heaving oscillations at a reduced frequency of $\frac{\pi}{10}$. At this frequency, the Z-force is of opposite phase to the velocity as would be expected in lower frequency motions. Computational results are presented for the source-doublet, the doublet Neumann membrane lattice, the source-Neumann wake piercing formulation with body piercing wakes (for a steady pressure Kutta condition). Comparison is made to theories presented by Theodorsen [104] and Katz and Plotkin [113].

6.4 Wing-Body Simulation Example

In this section, a practical simulation of a wing-body configuration is demonstrated. The example demonstrates the ability to reduce the problem setup time through the use of the novel approaches presented in this thesis. The use of a body piercing wake allows the wing-body mesh to be imported from a standard mesh generation tool.

6.4.1 Rigid Body Piercing Wakes

The first example presented demonstrates the use of rigid body piercing wakes. The geometry under consideration is presented in figure 6-11. The wing trailing edge vertices are prescribed, and from that the rigid wake geometry is constructed. The wake is extended into the wings through the trailing edge, as well as through the fuselage. The results of the wing body rigid-body-piercing-wake-only simulations are presented in figure 6-12. The results presented in figure 6-12 demonstrate the body-piercing wake approach for a practical

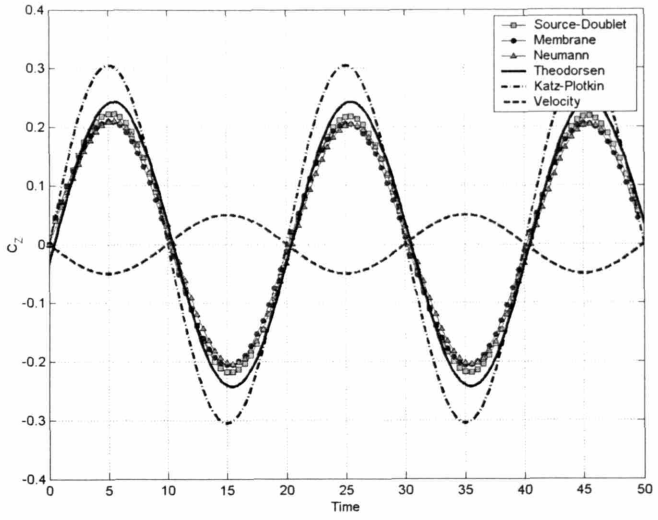

Figure 6-9: The plot illustrates the z-Component Coefficient of Force resulting from heaving oscillations at a reduced frequency of $\frac{\pi}{20}$. At this frequency, the Z-force is of opposite phase to the velocity as would be expected in lower frequency motions. Computational results are presented for the source-doublet, the doublet Neumann membrane lattice, the source-Neumann wake piercing formulation with body piercing wakes (for a steady pressure Kutta condition). Comparison is made to theories presented by Theodorsen [104] and Katz and Plotkin [113].

geometry.

6.4.2 Combined Body Piercing Wakes and Vortex Particles

A second example is considered in which both body-piercing wakes and vortex particles are used in the same simulation. The body piercing wakes are used to represent the vorticity at the trailing edge of the wing for the timestep under consideration. The wake is then converted to vortex particles in preparation for the next timestep. Results are presented in figure 6-13. The results demonstrate the pressure distributions as well as the vortex particle wake evolution. Tip vortices are seen forming downstream of the lifting surface. The effective lift of the wing-body configuration at 3 degrees angle of attack was $L_{eff} = 0.618$, while an aspect ratio 6 wing alone had an effective lift of $L_{eff} = 0.629$ and an aspect ratio 5.2 wing was found to have an effective lift of $L_{eff} = 0.516$. The lift coefficient for the wing-body was determined to be $C_L = 0.168$, while for an aspect ratio 6 wing

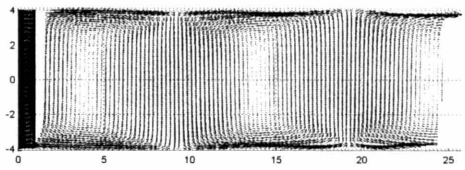

(a) An illustration of the vortex particle structure behind a slowly heaving wing. The appearance of distinct vortex rings is clear. These rings are a direct result of the heaving motion during which the Z-component of the forces oscillates between a positive and negative value.

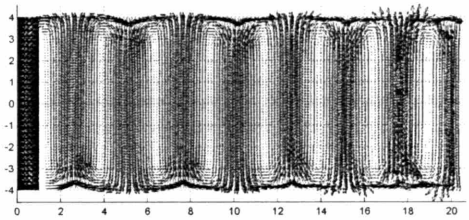

(b) The vortex particle structure behind a rapidly heaving AR8 wing. The figure illustrates the vortex particle structure behind a rapidly heaving wing. The appearance of distinct vortex rings is clear. These rings are a direct result of the heaving motion during which the Z-component of the forces oscillates between a positive and negative value.

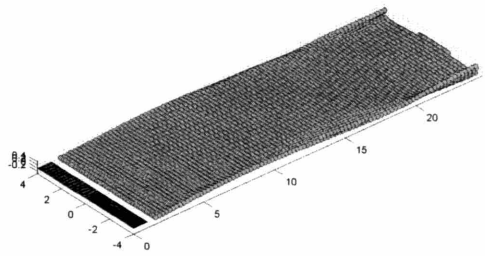

(c) An illustration of the vortex particles in the wake trailing a slowly heaving wing. The wake roll-up during the oscillation can be seen.

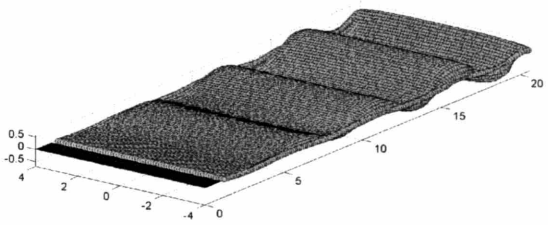

(d) An illustration of the vortex particles in the wake trailing a rapidly oscillating wing. The vortex wake self influence is seen to further deform the wake as the wake propagates downstream.

Figure 6-10: Plots of the vortex wake structures behind oscillating wings.

the lift coefficient was $C_L = 0.171$ and for an aspect ratio 5.2 wing $C_L = 0.162$. The results illustrate successful fuselage lift carryover is achieved with the body-piercing wake

(a) Side View.

(b) Front View.

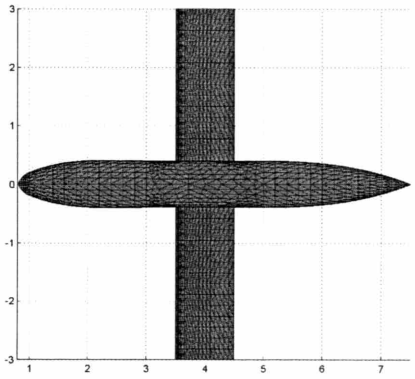

(c) Top View.

Figure 6-11: The geometry considered for the wing-body example.

formulation.

6.5 Example : Flapping Flight

In this section an example of the application of the panel method framework to a flapping flight application is presented.

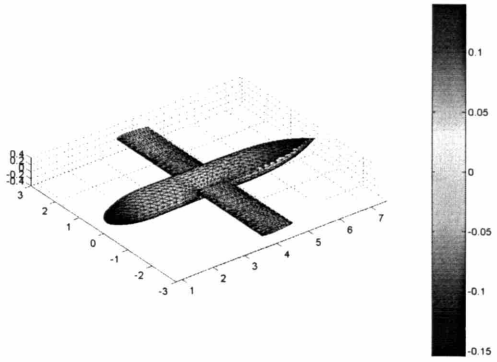

(a) Surface potential 3D view. Notice the body piercing wake approach captures the discontinuous potential along the fuselage when the overall potential ϕ is determined. Since the body piercing wakes are represented as a velocity influence the solution of the body surface potential ϕ_B is continuous. Note that the surface potential representation is based on the potential at the centroid of each of the panels, therefore, the wake potential jump does not appear along the wake shedding line.

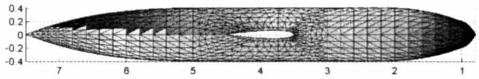

(b) Surface potential side view. Notice the body piercing wake approach captures the discontinuous potential along the fuselage when the overall potential ϕ is determined. Since the body piercing wakes are represented as a velocity influence the solution of the body surface potential ϕ_B is continuous. Note that the surface potential representation is based on the potential at the centroid of each of the panels, therefore, the wake potential jump does not appear along the wake shedding line.

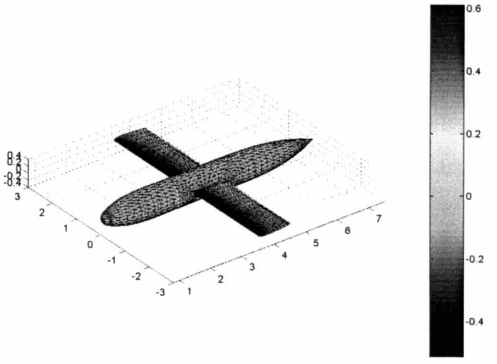

(c) Surface pressure plot. Notice here that the pressure is continuous.

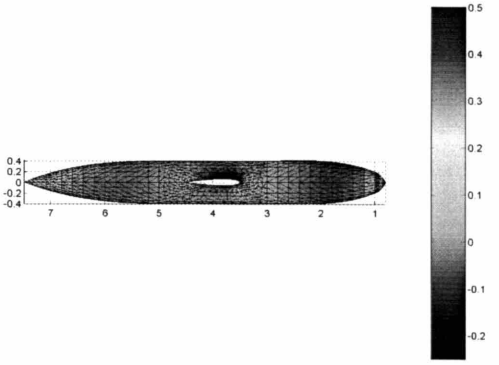

(d) Surface pressure plot. Notice here that the pressure is continuous.

Figure 6-12: Results for the surface potential and surface pressure considering a rigid body-piercing wake representation.

6.5.1 Flapping Wing Example

The method presented by Hall et al. [143] is used to determine the minimum power wake vorticity distribution for a particular flapping wing lifting line. In this case a simple hinged

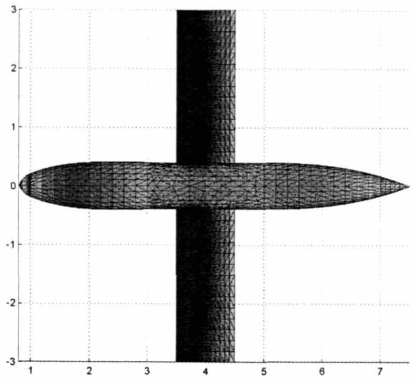

(a) The surface pressure distribution as viewed from above.

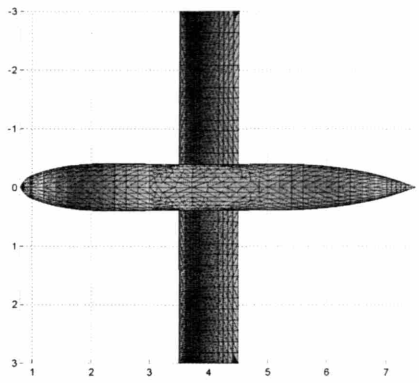

(b) The surface pressure distribution as viewed from below.

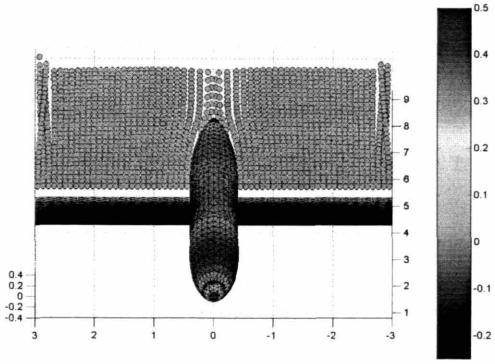

(c) Surface pressure plot including vortex particle wakes.

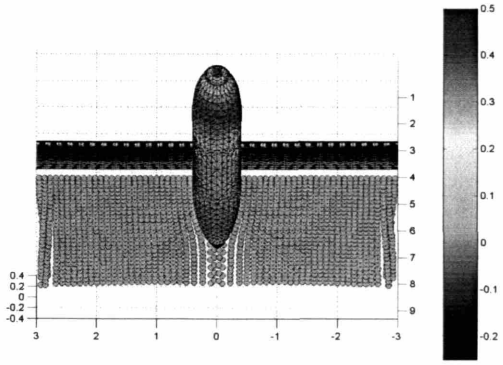

(d) Surface pressure plot including vortex particle wakes.

Figure 6-13: The geometry considered for the wing-body example.

flapping motion is considered. Considering the lifting line flapping motions, the wake imposed downwash and the resulting minimum power vorticity distribution, a thin membrane flapping wing geometry representation replicating the minimum power wake vorticity distribution is constructed as follows:

1. Construct a reference wing platform which flaps with the correct parameter dependence while shedding the least amount of vorticity possible into the domain. The wing can be designed to have a zero vorticity shedding throughout the wingbeat by instantaneous local modifications of section camber and angle of attack. In this ex-

periment, however, the wing is assumed to have a zero camber and the wing section is aligned with the flow at the leading edge. This assumption will produce a reference wing which has non-zero vorticity, especially in regions near the tip where incidence angles are important; however, as a first order approximation for demonstrating the translation process this is adequate.

2. Compute the downwash at lifting line positions along the wake considering only the vorticity downstream of the lifting line.

3. Compute the local section angle of attack for the entire wing beat at each spanwise section of the wing. This is computed considering the optimal vorticity distribution in the wake from the Hall *et. al.* simulations.

4. Adjust the reference wing platform for the local downwash effects due to the wake as well as the local sectional angle of attack. The resulting geometry will have significant twist as the wing span is traversed during the flapping motions.

5. Mesh the flapping wing as either a thick body representation (using an airfoil profile) or as a thin membrane. In this paper the thin membrane is considered due to the ease of meshing the geometry (especially near flapping joints).

The membrane doublet lattice code is used for these simulations due to the relative ease of meshing the morphing geometry with a thin surface approximation. The minimum power vorticity wake result from the Hall et al.[143] simulation approach is presented in figure 6-14(a). The panel method simulation results based on this result are presented in figures 6-14(b) - 6-14(d). Although the wake resulting from the panel method differs in fine details from the desired vorticity distribution, the result of the panel method simulation demonstrates a good overall agreement between the target vorticity wake structure and the resulting simulated vortex particle wake structure. In addition, the panel method simulation demonstrates the effects of wake roll-up during wingstroke segments where large vorticity release is expected (such as during the downstroke portion of the flapping cycle).

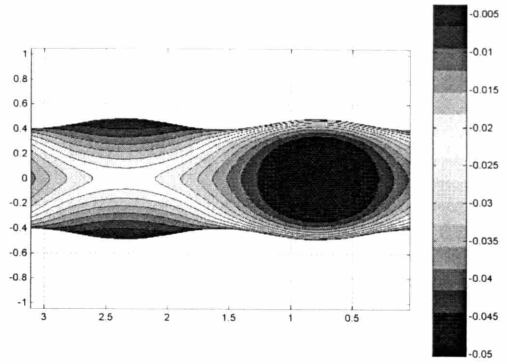

(a) The reference wake from the wake only minimum power vorticity solution. Flight path is from right to left.

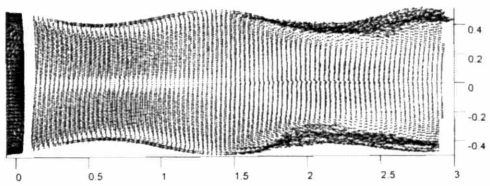

(b) A top view of the resulting FastAero simulation of a flapping geometry. Flight path is from right to left.

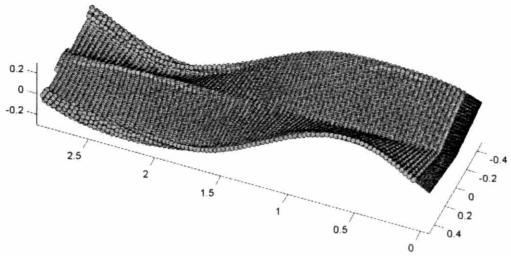

(c) An illustration of the vortex particle wake trailing a flapping wing, simulated using FastAero.

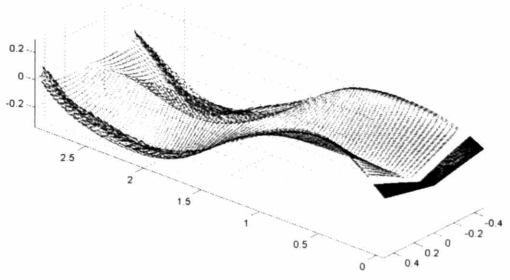

(d) An illustration of the vorticity in the wake trailing a flapping wing, simulated using FastAero.

Figure 6-14: A demonstration of the use of a wake only optimal vorticity distribution result to construct an efficient three-dimensional flapping wing geometry for simulation in an unsteady panel method solver.

6.6 Some Comments on Solution Time and Accuracy

The methods presented in this thesis have all been accelerated to scale nearly linearly with the number of discrete elements. Despite the acceleration of the methods, the computational burden can still be extensive. In this section the computational cost is discussed briefly. Although the current code is not completely optimized in terms of computational

structure and implementation, the discussion of the computational times will provide insight into the relative cost of each of the three panel method formulations.

6.6.1 Doublet Neumann Formulation

The doublet Neumann formulation is consistently the fastest approach for simulating unsteady lifting surface flows. This is due to the following reasons:

1. The number of surface elements needed for a particular simulation is typically one half of that needed for a similar thick body lifting surface simulation.

2. The problem involves the setup of a single linear system matrix. This results in a single accelerated system being setup per geometry.

3. The Aerodynamic Influence Coefficient Matrix is typically very well conditioned due to the strong diagonal dominance of the matrix.

4. The implementation of a linear Kutta condition means that the solution for any given timestep is known after a single solve. This does not involve additional solves to refine iterations.

5. The forces, moments and surface pressures can all be computed based on the doublet strength solution and surface gradients of the doublet strength. As a result, no forward evaluation of the integral equations are necessary.

As a result, the Doublet-Neumann method yields rapid solution times. For example, the unsteady rigid wing simulations in this chapter were all simulated in less than one hour on a 3.2 ghz Intel Pentium, 2GB RAM memory personal workstation.

6.6.2 Source Doublet Formulation

The source-doublet formulation is the next fastest approach for simulating the unsteady potential flow. The advantages of this approach are similar to the membrane doublet Neumann code with a few differences:

1. The rigid body problem involves a single setup of two linear system matrices. This results in a set of accelerated systems being setup per geometry.

2. The implementation of a linear Kutta condition means that the solution for any given timestep is known after a single solve.

3. The forces, moments and surface pressures can all be computed based on the doublet strength solution and surface gradients of the doublet strength. As a result, no forward evaluation of the integral equations are necessary.

The source-doublet formulation performs solutions in a comparable time as the Membrane Doublet Neumann code, however, is slower due to the comparably reduced conditioning of the linear system matrix and the increased complexity of thicker bodies. The thick wing, unsteady simulations were computed in under an hour.

6.6.3 The Body Piercing wake Formulation

The body piercing wake formulation is by far the most costly of the implementations. This is due to several reasons, but most notably:

1. The body piercing wake formulation involves and iterative pressure Kutta condition. Although a time savings is realized in using an approximate Jacobian, there is still significant computational cost in solving the linear system multiple times to determine the wake strength and surface singularity distribution.

2. The post-processing of the solution involves the setup and evaluation of an integral equation for both the body induced velocity and the body induced potential. In a future version of the method these matrices should be setup on a one-off basis for rigid body simulations. The setup and forward evaluation of the integral equation for post-processing purposes imposes a significant time penalty on the method.

Although the source-Neumann-body-piercing-wakes formulation presents increased solution times, it should be noted that the reduction of the solution setup time and grid generation complexity should easily offset the cost of the solution. In addition, when compared

on an even level with the other methods (rigid body simulations implementing non-linear iterative pressure Kutta conditions) the source-Neumann approach will not be significantly unfavorable.

6.6.4 Rigid Vs. morphing Bodies

The computational framework has the capacity to simulate both rigid bodies as well as morphing geometry bodies. The two options prove to have significantly different solution times. For the rigid body, the body system matrices for the are setup once. At each iteration the solution involves solving for the particular boundary conditions on the given geometry. In the case of the morphing geometry problem, the solution is performed on a different geometry at each step. In the current implementation this means that the system matrix setup time for each timestep takes a significant portion of that particular step's time. As a result, morphing body geometries are typically significantly more costly that their rigid body counterparts. As a result, future work will involve reducing the linear system setup time in the pFFT algorithm through thorough optimization of the computational routines.

6.6.5 Comments on the use of Galerkin linear basis approaches

In each of the formulations implemented in this thesis, a Galerkin, linear basis approach was considered. The additional computational complexity due to the high order galerkin method compared with a lower order constant collocation approaches is seen more predominantly at the linear system setup stages of the computation where an approximately six-fold increase in computational time is seen. This is due to the following two reasons:

1. The linear basis function panel integration costs are approximately two times more expensive than the constant basis counterpart.

2. The Galerkin testing involves a quadrature integration which at minimum comprises the panel integration at 3 positions on the target panel. When compared with the single evaluation point in a constant collocation approach, the Galerkin method is at least three times more expensive.

Although the linear Galerkin approaches are more time consuming than constant collocation, the benefits of increased convergence and more refined solution representation outweigh the disadvantages.

6.7 Conclusions

in this chapter several example simulations highlighting the panel method formulations implemented have been shown. The methods are all in good agreement with available theoretical, computational and analytical results.

Chapter 7

Conclusions

This thesis presents a panel method which addresses the drawbacks with current panel method implementations.

7.1 Contributions

Several contributions have been made in this thesis.

7.1.1 The general panel method framework

The panel method which has been developed in this thesis represents a synthesis of both new and existing ideas, which when combined form a powerful tool for the rapid, hands off analysis of steady and unsteady lifting body and wing-body flows. The tool is a contribution in that it combines the most effective strategies currently available with contributions to the field made in this thesis to provide an advanced potential flow analysis environment . The tool which has been developed provides a framework in which potential flow simulations can be easily performed requiring:

- Minimal user setup time due to automatic wake generation strategies.
- Minimal user expertise in wake modeling due to the use of automatic vortex particle wake generation schemes.
- Minimal solution turnaround times due to the implementation of fast acceleration

approaches.

- Minimal user interference due to the hands off automatic wake strategies.

The approach relies on advanced acceleration algorithms (pFFT [109] and FMT [110]) to facilitate the rapid solution of a combined panel method-vortex-particle approach [63, 62].

7.1.2 Body Piercing Wake Formulation

The thesis presents a potential flow formulation which considers body piercing wakes to handle the difficulties associated with wing-body geometries in both traditional panel method approaches as well as combined panel method and vortex particle method approaches. The introduction of body piercing wakes permits wing-body simulations which have not been possible in previous panel method-vortex particle approaches [62].

7.1.3 Higher Order Integration Approaches

This thesis presents the development of a conceptually simple, yet accurate, quadratic basis function, quadratic geometry self term panel integration approach for the double layer integration. In addition, a desingularized projection based numerical integration approach for the single layer self term has been implemented to form a quadratic basis, quadratic geometry dense system BEM solver.

7.2 Future Work

Although the panel method presented in this thesis represents a complete framework, there are several directions of future work which will be considered:

1. The continued development of the panel method to include:

   (a) Viscous diffusion in the vortex particle wake. The addition of viscous diffusion models will provide accurate vorticity wake models for flows which will be considered (such as lower Reynold's number natural flapping flight applications).

(b) Boundary layer corrections through the use of integral boundary layer methods.

(c) More panel integration schemes and orders into the panel method framework. For example, implementing the curved panel, high order integration approaches into the accelerated potential flow framework.

(d) Several wake models of differing complexity. Due to the generality of the Helmholtz decomposition of the velocity field, many diverse wake models can be considered. In certain situations, a filament or sheet based wake model might be more appropriate than the vortex particle approach. As such, incorporating those models into the general accelerated framework will prove useful.

2. The use of the panel method to analyze complex unsteady potential flow problems particularly suited to hands-off, automatic wake handling, for example:

(a) Rotor aerodynamics: Due to the non-diffusive nature of the Lagrangian vortex particle dynamics, accurate models of rotor aerodynamics are possible.

(b) Natural flapping propulsion and flight aerodynamics: Due to both the rapid solution of unsteady flow problems as well as the automatic hands-off simulation capabilities the method presented in this thesis represents an attractive approach for natural flapping propulsion and flight analysis.

(c) Induced drag reduction in formation flight: Due to the automatic wake generation and advection, analyzing formation flight drag reduction is simplified when compared to previous approaches.

Bibliography

[1] Noh, W.F. *A time-dependent two-space dimensional coupled Euler-Lagrangian code*, Meth. in Comp. Physics, Vol. 3, 95(1):115-138, 1992.

[2] Franck, R.M., Lazarus, R.B., *Mixed Eulerian-Lagrangian method.* Meth. in Comp. Physics, Vol. 3, 47-67, 1964.

[3] Belytschko, T., Kennedy, J.M., Schoeberle, D.F., *Quasi-Eulerian finite element formulation for fluid-structure interaction* . Proceedings of Joint ASME/CSME Presseure Vessels and Piping Conference. ASME: paper 78-PVP-60, 1978.

[4] Hamamoto, M., Ohta, Y., Hara, K, Hisada, T., *Free-flight analysis of flapping flight during turning by fluid structure interaction finite element analysis based on arbitrary lagrange-eulerian method*, Intl. Conf. on robotics and Automation, IEEE, 2004.

[5] Peskin, C.S.,*Flow Patterns Around Heart Valves: A Digital Computer Method for Solving the Equations of Motion*, PhD. Thesis. Physiol., Albert Einstein Coll. Med., Univ. Microfilms, 378:72-30, 1972.

[6] Peskin, C.S., *The immersed boundary method*, Acta Numerica, 2002:479-517, Cambridge University Press, 2002.

[7] Mittal, R., Iaccarino, G., *Immersed boundary methods*, Annu. Rev. of Fluid Mech., 37:239-61, 2005.

[8] G.K.Batchelor, *An Introduction to Fluid Dynamics*, Cambridge University Press, Cambridge, 2000.

[9] Anderson, J.D. *Fundamentals of Aerodynamics*, 3rd. Edition, McGraw-Hill Science/Engineering/Math, 2001.

[10] Hess, J.L., *Panel methods in computational fluid dynamics*, Annu. Rev. of Fluid Mech., 22:255-74, 1990.

[11] Hess, J.L. *Higher-order numerical solution of the integral equation for the two dimensional Neumann problem.* Comput. Methods Appl. Mesh. Eng., 2:1-15, 1973.

[12] Hess, J.L. *The problem of three-dimensional lifting flow and its solution by means of surface singularity distribution.* Comput. Methods Appl. Mech. Eng. 4:283-319, 1974.

[13] Hess, J.L., Smith, A.M.O., *Calculation of nonlifting potential flow about arbitrary three-dimensional bodies.* J. Ship Res., 8:22-44, 1964.

[14] Ahmadi, A., Widnall, S.E., *Unsteady lifting line theory as a signular perturbation problem*, J. Fluid Mech., 153:59-81, 1985.

[15] Cenko, A., *PAN AIR applictions to complex configurations*, J. of Aircraft, 0021-8669, vol 20, no. 10, 887-892, 1983.

[16] Park, M.A., Green, L.L., Montgomery, R.C., Raney, D.L., *Determination of stability and control derivatives using computational fluid dynamics and automatic differentiation*, AIAA-99-3136, 1999.

[17] Nathman, J. *Improvement of a panel method by including panel warp*, AIAA-2004-721, 42nd Aerospace Sciences Meeting and Exhibit, Reno, Nevada, 2004.

[18] Tinoco, E.N., Ball, D.N., Rice, F.A., *PANAIR analysis of a transport high-lift configuration*, J. Aircr., 24:181-86, 1987.

[19] T. R. Quackenbush, D. A. Washspress, A.H.Boschitsch, *Rotor Aerodynamic Loads Computation Using a Constant Vorticity Contour Free Wake Model*, Juornal of Aircraft, vol.32 no.5, pp 911-920, 1995.

[20] Keuthe, A.M., amd Chow, C.-Y.,*Foundations of Aerodynamics: Bases of Aerodynamic Design,* 4th ed., John Wiley and Sons, New York, 1986.

[21] Katz, J., Plotkin, A., *Low-speed aerodynamics: from wing theory to panel methods*, McGraw-Hill, New York, 1991.

[22] Rosen, B.S., Laiosa, J.P., Davis, W.H., Stavetski, D., *Splash Free-Surface Flow Code Methodology for Hydrodynamic Design and Analysis of IACC Yachts*, 11 Chesapeake Sailing Yacht Symposium, Annapolis, 1993.

[23] Sclavounos, P.D., *Ship flow simulation in calm water and waves*, SWAN 1 Version 3.1, User Manual, Boston Marine Consulting Inc., 1999.

[24] Lamb, H, *Hydrodynamics.*, London, Cambridge University Press, 6th ed., 1932.

[25] Kellogg, O.D., *Foundations of Potential Theory*, Dover Publications, 1954.

[26] Brazier, J.G., and Smith, A.M.O., *Development of Nose and Tail Shapes in Incompressible, Irrotational Flow*, Douglas Aircraft Co., Long Beach, CA, Rept. E.S. 0875, June 1947.

[27] Eppler, R., *Airfoil Design and Data*, Springer Verlag, Berlin, 1990.

[28] Selig, M.S., Maughmer, M.D., *A multi-point inverse airfoil design method based on conformal mapping*, AIAA-1991-69, 29th Aerospace Sciences Meeting and Exhibit, 1991.

[29] Smith, A.M.O., Pierce, J., *Exact solution of the Neumann problem. Calculation of plane and axially symmetric flows about or within arbitrary boundaries*, Proc. U.S. Natl. Congr. Appl. Mech., 3rd, Providence, R.I., pp.807-15, 1958.

[30] Carmichael, R.L. and Woodward, F.A, *An integrated approach to the analysis and design of wings and wing-body combinations in supersonic flow*n NASA TN D-3685, 1966.

[31] Morino, L., Luo, C.C., *Subsonic potential aerodynamics for complex configurations. A general theory*. AIAA J., 12:191-97.

[32] Johnson, F.T., *A general panel method for the analysis and design of arbitrary configurations in incompressible flows.* NASA CR-3079, 1980.

[33] Oskam, B. *Transonic panel method for the full potential equation applied to multipcomponent airfoils.* AIAA J. 23:1327-34, 1985.

[34] Coopersmith, R.M., Youngren, H.H., Bouchard, E.E., *Quadrilateral Element Panel Method (QUADPAN)*, Theoretical Report (V. 3.0), Lockheed-California, LR, 1983.

[35] Maskew, B.,*USAERO, A Timestepping Analysis Method for the Flow About Multiple Bodies in General Motions, User Manual*, Technical Report, Analytical Methods, Inc., Redmond, WA, 1990.

[36] High order panel emthod paper

[37] Fornasier, L., *HISS-A high order subsonic/supersonic singularity method for calculating linearized potential flow*, 17th AIAA Fluid dynamics, plasma dynamics and lasers conference, 1984.

[38] Drela, M., *XFOIL: An Analysis and Design System for Low Reynolds Number Airfoils*, Conference on Low Reynolds Number Aerodynamics, University of Notre Dame, June 1989.

[39] Liebeck, R.H., *Subsonic Airfoil Design*, In, Applied Computational aerodynamics, Vol 125 Progress in Astronautics and Aeronautics, AIAA, pp, 133-165, 1990.

[40] Mughal, B., Drela, M., *A calculation method for the three-dimensional boundary layer equations in integral form*, AIAA Paper 93-0786, Reno, NV, 1993.

[41] Nishida, B., and Drela, M., *Fully Simultaneous Coupling for three dimensional viscous/inviscid flows*, AIAA-95-1806-CP, AIAA 13th Applied Aerodynamics Conference, June, 1995.

[42] Bulirsch, R., Stoer, J., *The congugate-gradient method of Hestenes and Stiefel*,Section 8,7 in *Introduction to Numerical Analysis.*, New York, Springer Verlag, 1991.

[43] Freund, R., Nachtigal, N. *QMR: A quasi-minimal residual method for non-hermitian linear systems*, Numer. Math., 60:315-339, 1991.

[44] Nabors, K, White, J.K., *FastCap: A Multipole Accelerated 3-D Extraction Program*, IEEE Trans. On Comp. Aided Design, Vol. 10, No. 11, 1991.

[45] Aluru, N.R., Nadkarni, V., White, J.K., *A parallel precorrected-FFT based capacitance extraction program for signal integrity analysis*, Proceedings of the 33rd Design Automation Conference, Las Vegas, Jun, 1996.

[46] Board, J.A., Hakura, Z.S., Elliot, W.S., Gray, D.C., Blanke, W.J., Leathrum, J.F.,Jr.*Scalable implementations of multipole-accelerated algorithms for molecular dynamics*, Technical Report 94-002, Duke University, 1994.

[47] Willis, D.J., Lee, J., Coehlo, C.P.Bardhan, J, Hu, X., Ried, H., White, J.K., *pFFT2+: A Generic precorrected-FFT algorithm in C++: Users Manual*, Work in progress.

[48] Frigo, M., Johnson, S.,*FFTW Users Manual, Version 3.0.1*, Massachusetts Institute Of Technology, 2003.

[49] Vassberg, J, C. *A fast surface-panel method capable of solving million-element problems*, 35th AIAA Aerospace Sciences Meeting and Exhibit,AIAA-97-0168, 1997.

[50] Cooley, J.W., Tukey, O.W. *An algorithm for the machine calculation of complex fourier series.*, Math. Comput., 19:297-301, 1965.

[51] Jameson, A. *Aerodynamics design via control theory*, J. Sci. Comp. 3:233-60, 1988.

[52] Jameson, A. *Solution of the Euler Equations by a Multigrid Method*, Appplied math. and Computation, Vol. 13, pp.327-356, 1983.

[53] L. Rosenhead, *The formation of vorticies from a surface of discontinuity*, Proc. Roy. Soc. London Ser. A 134, 170-192, 1931.

[54] Cottet, G-H, Koumoutsakos, P.D.,*Vortex Methods:Theory and Applications*, Cambridge University Press, London, 2000.

[55] A. J. Chorin, *Vortex models and boundary layer instability*, SIAM J. Sci. Stat. Comput. 1:1-21, 1980.

[56] Cottet, G-H, Koumoutsakos, P., Ould-Salihi, M.L.,*Vortex methods with spatially varying cores*, J. Comput. Phys. 162 164-185, 2000.

[57] J. T. Beale, A. Majda, *Vortex methods I: convergence in three dimensions*, Math. Comput. 29 (159) 1-27, 1982.

[58] A. Leonard, *Vortex methods for flow simulation*, J. Comput. Phys. 37, 289-335, 1980.

[59] Leonard, A. *Computing three-dimensional incompressible flows with vortex elements*. Ann. Rev. Fluid Mech. 17:523-559, 1985.

[60] O. M. Knio, A. F. Ghoniem, *The three-dimensional structure of periodic vorticity layers under non-symmetric conditions*, J. Fluid Mech. 243, 353-392, 1992.

[61] Spalart, P.R., *Two recent extensions of thevortex particle method*, presented at the 22nd Aerospace Sciences Meeting and Exhibit, AIAA Paper 1984-343, Reno, January 1984.

[62] Voutsinas S.G., Belessis M.A., and Rados K.G., *Investigation of the yawed operation of wind turbines by means of a vortex particle method.* AGARD-CP-552 FDP Symposium on Aerodynamics and Aeroacoustics of Rotorcraft, Berlin, Germany, Paper 11, 1995.

[63] Rehbach, C., *Calcul numerique d'ecoulement tridimensionels instationaires avec nappes tourillonnaires*, La Recherche Aerospatiale, pp.289-298, 1977.

[64] Huberson, S. *Calcule d'ecoulements tridimensionnels instationnaires incomprressibles par une methode particulaire*. Journal de Mecaniques Theorique et Appliquee, 3(1): 805-819, 1984.

[65] Eldredge, J. D., *Efficient tools for the simulation of flapping wing flows,* presented at 43rd AIAA Aerospace Sciences Meeting, AIAA Paper 2005-0085, Reno, January 2005.

[66] Y.M. Marzouk, A.F. Ghoniem, *Mechanism of streamwise vorticity formation in a transverse jet*, 40th Aerospace Sciences Meeting and Exhibit, AIAA-2002-1063, January 2002.

[67] A. Gharakhani, A. F. Ghoniem, *Three-dimensional vortex simulation of time dependent incompressible internal viscous flows*, J. Comput. Phys. 134:75-95, 1997.

[68] Anderson, C., *A method of local corrections for computing the velocity field due to a distribution of vortex blobs.* J. Comput. Phys., vol 62, 111-123, 1986.

[69] Ploumhans, P., Winckelmans, G.S., *Vortex methods for high-resolution simulations of viscous flow past bluff bodies of general geometry.* J Comput Phys, 165:354-406, 2000.

[70] Appel, A.A., *An efficient program for many body simulations'*, SIAM Journal of scientific and statistical computing, vol. 16, n. 1, pp85-103, 1985.

[71] Maskew, B., *Prediction of subsonic aerodynamic characteristics: a case for low-order panel methods.*, J. Aircr., 19:157-63, 1982.

[72] Kerwin, J.E., Kinnas, S.A., Lee, J-T, Shih, W-Z,*A Surface Panel MEthod for the Hydrodynamic Analysis of Ducted Propellers*, SNAME Transactions, Vol. 95, 93-122, 1987.

[73] Kinnas, S.A., Hsin, C.Y., *Boundary Element Method for the Analysis of the Unsteady Flow Around Extreme Propeller Geometries*, AIAA Journal, Vol. 30, No. 3, 688-696, 1992.

[74] Liu, P, Bose, N., Colbourne, B., *A Broyden Numerical Kutta Condition for an Unsteady Panel Method*,

[75] Anderson, D.A., Tennehill, J.C., Pletcher, R.H.,*Computational Fluid Mechanics and Heat Transfer*, Taylor and Francis, 1997.

[76] D.J.Willis, J.Peraire, and J.K.White *To be presented*, 44th AIAA Aerospace Sciences Meeting and Exhibit, AIAA 2006-1253, 2006.

[77] Arfken, G. "Helmholtz's Theorem." Sec1.15 in *Mathematical Methods for Physicists, 3rd ed.* Orlando, FL: Academic Press, pp. 78-84, 1985.

[78] A. M. O. Smith, *The Panel Method: Its Original Development*, In, Applied Computational aerodynamics, Vol 125 Progress in Astronautics and Aeronautics, AIAA, pp, 3-20, 1990.

[79] D. L. Ashby, M. R. Dudley, and S. K. Iguchi, *Development and Validation of an Advanced Low Order Panel Method*, NASA TM 101024, Oct 1988.

[80] B. Maskew,*PROGRAM VSAERO: A Computer Program for Calculating the Non-Linear Aerodynamic Characteristics of Arbitrary Configurations"*, NASA CR-166476, Nov 1982.

[81] B. Rosen, J. P. Laiosa, *SPLASH Nonlinear and Unsteady Free-Surface Analysis Code for Grand Prix Yacht Design*, 13th Chesapeake Sailing Yacht Symposium, Annapolis, Jan 1997.

[82] P.Koumoutsakos, *Multiscale Flow Simulations Using Particles*, Annu. Rev. Fluid Mech., 37:457-487, 2005.

[83] WAMIT 6.2. *WAMIT User Manual, Version 6.2, 6.2PC and 6.1S, 6.1S-PC*, Dept. Of Ocean Engineering, M.I.T.

[84] J. R. Philips and J. K. White, *A Precorrected-FFT Method for Electrostatic Analysis of Complicated 3-D Structures*, IEEE Transactions On Computer-Aided Design of Integrated Circuits and Systems, IEEE, Vol. 16, 1997.

[85] L. Greengard and V. Rohklin, *A Fast Algorithm for Particle Simulations*, J. Comp. Phys., 73:pp325-384, 1987.

[86] J. Barnes and P. Hut, *A Hierarchical O(N log N) Force Caluclation Algorithm*, Nature 324, pp 446-449, 1986.

[87] L. Morino,*Steady, Oscillatory and Unsteady Subsonic and Supersonic Aerodynamics - Production Version (SOUSSA)* NASA CR-157130, 1980.

[88] G. S. Winckelmansand A. Leonard, *Contributions to Vortex Particle Methods for the Computation of Three-Dimensional Incompressible Unsteady Flows*, J. Comp. Phys, 109, pp 247-273, 1993.

[89] Brebbia, C., *Boundary Element Methods in Engineering: Proceedings*, Springer, New York, 1982.

[90] Chen, G., Zhou, J. *Boundary Element Methods*, 1st Ed., Academic Press, 1992.

[91] A. M. O. Smith and J. .L Hess, *Calculation of potential flow about arbitrary bodies.*, Progress in Aeronautic Sciences, 8, 1960.

[92] R.Kress, *Linear Integral Equations.* Springer-Verlag, New York, 1989.

[93] K.E.Atkinson, and W.Han *Theoretical Numerical Analysis: A Functional Analysis Framework*, Springer-Verlag, 2001.

[94] Willis, D.J. *A pFFT accelerated, High Order Panel Method* , Masters Thesis, MIT, 2003.

[95] Jackson, J.D., *Classical Electrodynamics, Third Edition*, John Wiley and Sons Inc., New York, 1998.

[96] Kythe, P.K. *An introduction to boundary element methods.*, CRC Press, Boca Raton, 1995.

[97] E.Hairer , C.Lubich, G.Wanner, *Geometric Numerical Integration*, Springer Series in Computational Mathematics, Springer, 2004.

[98] D.J.Willis, J. Peraire, J.K.White, *Body Piercing Wakes For Automatic Wake Generation in the Potential Panel Method*, Work in Progress.

[99] J. N. Newman, *Distribution of Sources and Normal Dipoles Over a Quadrilateral Panel*, J. Eng. Math., 20, 1985.

[100] Y. Saad and M. Schultz, *GMRES: A generalized Minimal Residual Algorithm for Solving Non-Symmetrixc Linear Systems*, SIAM, J. Sci. Stat. Comp., Vol 7, 1986.

[101] Z. Zhu, B. Song and J. K. White, *Algorithms in FastIMP: A Fast Wideband Impedance Extraction Program for Complicated 3D Geometries*, Proceedings of IEEE/ACM Design Automation Conference, Anaheim, California, June 2-6, 2003.

[102] R.W.Hockney, J.W.Eastwood, *Computer Simulation Using Particles*, Taylor and Francis Inc., Bristol, 1988.

[103] J. Katz, A. Plotkin, *Low-Speed Aerodynamics*,Second Edition, Cambridge Aerospace Series, Cambridge, 2001.

[104] T. Theodorsen, *General Theory of Aerodynamic Instability and the Mechanism of Flutter*,NACA Report 496, 1935.

[105] J.Peraire, J.Piero, L.Formaggia, K.Morgan, and O.C.Zienkiewicz, *Finite Element Euler Computations in Three Dimensions*, Int. J. Num. Meth. in Engn. 26, 2135-2159, 1988.

[106] D. L. Ashby, M. R. Dudley, and S. K. Iguchi, *Development and Validation of an Advanced Low Order Panel Method*, NASA TM 101024, Oct 1988.

[107] B. Maskew,*PROGRAM VSAERO: A Computer Program for Calculating the Non-Linear Aerodynamic Characteristics of Arbitrary Configurations"*, NASA CR-166476, Nov 1982.

[108] D.J. Willis, J. Peraire, J.K. White, *A Combined pFFT-Multipole Tree Code, Unsteady Panel Method with Vortex Particle Wakes*, 43rd AIAA Aerospace sciences Meeting and Exhibit, AIAA-2005-0854, 10-13 January 2005.

[109] J. R. Philips and J. K. White, *A Precorrected-FFT Method for Electrostatic Analysis of Complicated 3-D Structures*, IEEE Transactions On Computer-Aided Design of Integrated Circuits and Systems, IEEE, Vol. 16, 1997.

[110] L. Greengard and V. Rohklin, *A Fast Algorithm for Particle Simulations*, J. Comp. Phys., 73:pp325-384, 1987.

[111] X. Wang, J.N.Newman, and J.K.White, *Robust Algorithms for Boundary Element Integrals on Curved Surfaces* , International Conference on Modeling and Simulation of Micro systems, 2000.

[112] J. N. Newman, *Distribution of Sources and Normal Dipoles Over a Quadrilateral Panel*, J. Eng. Math., 20, 1985.

[113] J. Katz, A. Plotkin, *Low-Speed Aerodynamics, 2nd Edition*, Cambridge university Press, New York, 2001.

[114] O.D.Kellogg *Foundations of Potential Theory*,J. Springer, New York, 1929.

[115] C.Y. Hsin, J.E.Kerwin, and J.N.Newman, *A high order panel method based on B-Splines*. Proceedings of Sixth International Conference on Numerical Ship Hydrodynamics, eds. V.C. Patel and F. Stern, National Academy Press: Washington, pp133-151, 1993.

[116] A.E. Magnus, and M.A.Epton, *PAN AIR- A Computer Program for predicting Subsonic or Supersonic Linear Potential Flows about Arbitrary Configurations Using a High Order Panel Method*, Volume 1, Theory Document (Version 1.0), NASA CR-3251, 1980.

[117] C.S. Lee and J.E. Kerwin, *A B-Spline Higher-Order Panel Method Applied to Two Dimensional Lifting Problems*, Journal Of Ship Research, Volume 47, Number 4, pp 290-298, 2003.

[118] P. Ramachandran, S.C. Rajan, M. Ramakrishna, *A Fast Multipole Method for Higher Order Vortex Panels in Two Dimensions*, SIAM Journal on Scientific Computing, Vol 26, Issue 5, pp. 1620-1642, 2005.

[119] H. Maniar, *A B-Spline Based Higher Order Method in 3D*, Presented at the 10th Workshop on Water Waves and Floating Bodies, Oxford, England, 1995.

[120] H. Maniar, *A Three Dimensional High Order Panel Method Based on B-splines*, PhD. Thesis, Massachusetts Institute Of Technology, 1995.

[121] F.E. Ehlers, F.T.Johnson, and P.E. Rubbert, *A Higher Order Panel Method for Linearized Supersonic Flow.* AIAA 76-381, July 1976.

[122] J. Hess, and A.M.O Smith, *Calculation of Non-lifting potential flow about arbitrary three dimensional bodies*, J. Ship Research, 8, pp 22-44, 1994.

[123] U. Lemma, V.Marchese,and L. Morino, *High-order BEM for potential transonic flows*, Computational Mechanics, Springer Verlag, Vol. 21, No. 3, pp. 243-252, 1998.

[124] J.H.M. Frijns, *Improving the Accuracy of the Boundary Element Method by the use of Second-Order Interpolation Functions.*, IEEE Transactions on Biomedical Engineering, Vol. 47, No. 10, October 2000.

[125] A. Buchau, W. Rieger, and W.M.Rucker *BEM Computations Using the Fast Multipole Method in Combination with Higher Order Elements and the Galerkin Method.*, IEEE Transactions on Magnetics, Vol. 37 No. 5, September 2001.

[126] K.J.Bathe *Finite Element Procedures*, Prentice Hall, 1995.

[127] K.E.Atkinson, and W.Han *Theoretical Numerical Analysis: A Functional Analysis Framework*, Springer-Verlag, 2001.

[128] R. Klees, *Numerical calculation of weakly singular surface integrals*, Journal of Geodesy, Vol 70, pp 781-797, 1996.

[129] J.-L. Guermond, *Numerical Quadratures for layer potentials over curved domains in* R^3, SIAM Jounral of Numercial Analysis, Vol. 29, No. 5, pp. 1347-1369, 1992.

[130] K. Hayami, C.A.Brebbia *Quadrature Method for Singular and Nearly Singular Integrals in 3-D Boundary Element Method*, Boundary Element X, vol. 1, Mathematical and Computational Aspects. 1987.

[131] Graglia, R.D. *On the Numerical Integration of the Linear Shape Functions Times the 3-D Green's Function or its Gradient on a Plane Triangle*, IEEE Transactions on Antennas and Propagation, Vol. 41, No. 10, pp 1448-1456, 1993.

[132] L. Rossi, P.J.Cullen. *On the fully numerical evaluation of the linear-shape function times the 3D Green's Function on a Plane Tirangle*, IEEE Transactions on microwave theory and techniques, vol. 47, No. 4, pp. 398 - 403, 1999.

[133] P. Kim, and U.J.Choi, *Two Trigonometric Quadrature Formulae for evaluating hypersingular integrals*, International Journal For Numerical Methods in Engineering, Vol. 56, pp 469-486, 2003.

[134] Cools, R., *An encyclopedia of cubature formulas*, Journal of Complexity, Vol 19(3), pages 445-453, 2003.

[135] Cools, R. *Monomial cubature rulse since "Stroud": a compilation – part 2.* J. Comput. Appl. Math, 112(1-2): 21–27, 1999.

[136] Cools, R. and Rabinowitz *Monomial cubature rules since "Stroud": a compilation*, J. Comput. Appl. Math, 48: 309-326, 1993.

[137] Kinnas, S.A., and Hsin, C.Y., *Boundary element method for the analysis of the unsteady flow around extreme propeller geometries*, AIAA Journal, Vol. 30, No. 3, pp.688-696, 1992.

[138] Kerwin, J.E., Kinnas, S.A., Lee, J-T and Shi, W-Z., *A surface panel method for the hydrodynamic analysis of ducted propellers*, SNAME Transactions, Vol. 95, pp. 93-122, 1987.

[139] Press, W.H., Teukolsky, S.A., Vetterling, W.T., Flannery, B.P., *Numerical Recipes in C: The Art of Scientific Computing, 2nd Edition*, Cambridge University Press, New York, 1992.

[140] Broyden, C.G., *Quasi-Newton Methods and Their Applications to Function Minimization*, Mathematics of Computation, Vol. 21, No. 99, pp. 368-381, 1967.

[141] Fletcher, R., *Practical Methods of Optimization (2nd Ed.)*, John wiley, Chichester, 1987.

[142] Liu, P., Bose, N., and Colbourne, B.,*A Broyden numerical Kutta condition for an unsteady panel method* Internaional Shipbuidling Progress, vol. 49, no. December, pp. 263-274, 2002.

[143] Hall, K. C., Pigott, S.A., and Hall, S.R., *Power Requirements for Large-Amplitude Flapping Flight*, Journal of Aircraft, Vol. 35, No. 3, pp.352-361, 1998.